

On the stiffness of linear roller bearings

David Onno Wijnberg

On the stiffness of linear roller bearings

by

David Onno Wijnberg

to obtain the degree of Master of Science
at the Delft University of Technology,
to be defended publicly on Friday 27 August, 2021 at 13:30.

Thesis committee: Dr. ir. R.A.J. van Ostayen, TU Delft, supervisor
Dr. ir. R. Eling, supervisor
Prof. Dr.-Ing. H. Vallery
Dr. G.J. Verbiest

This thesis is confidential and cannot be made public until August 27, 2023.

An electronic version of this thesis is available at <http://repository.tudelft.nl/>.

Contents

1	Introduction	1
1.1	Bearings	2
1.1.1	Bearing principles	2
1.1.2	Types of rolling bearings	3
1.2	The relevance of bearing stiffness quantification	4
1.2.1	The definition of stiffness	4
1.2.2	The role of stiffness in mechatronic system performance	4
1.2.3	Stiffness in relation to static system performance	5
1.2.4	Stiffness in relation to dynamic system performance	5
1.3	Research goal	6
1.4	Structure of this Thesis	6
2	Literature	7
2.1	A brief history of rolling element bearings	8
2.2	Individual roller-rail contact models	8
2.2.1	Analytic models	9
2.2.2	Numerical models	10
2.2.3	Experimental work	11
2.3	Surface roughness	12
2.4	Lubrication	13
2.5	Standards for linear motion rolling bearing	14
2.6	Preload	15
2.7	Stiffness descriptions of bearing assemblies	15
2.7.1	Rotation rolling bearings	15
2.7.2	Linear motion rolling bearings	16
2.7.3	Experimental stiffness validation methods	16
2.8	Status quo and identification of open challenges	18
3	Theoretical description of roller-rail contact stiffness	19
3.1	Description of the roller-rail system	20
3.2	Modelling steps	21
3.3	2D analytical model	22
3.4	2D finite element model	30
3.4.1	Contact pressure and internal stress	30
3.4.2	Compression of the roller	31
3.4.3	Compression of the rail	31
3.4.4	Synopsis of the 2D model	32
3.5	3D finite element model	33
3.5.1	Contact pressure and internal stress	33
3.5.2	3D compared to 2D	35
3.5.3	Compression of the roller	35
3.5.4	Compression of the rail	36
3.5.5	Synopsis of the 3D model	37
3.6	Compression of a full 3D rail geometry	37
3.7	Synopsis	40

4	Stiffness of a normally loaded roller between two flat rails	41
4.1	Test setup	42
4.1.1	Considerations on a contact stiffness measurement setup	42
4.1.2	Description of the setup	43
4.1.3	Numeric multi body dynamics analysis of the setup	44
4.1.4	Test procedure	44
4.1.5	Test equipment	45
4.2	Test results and discussion	45
4.2.1	Precision of the setup	45
4.2.2	Accuracy of the setup	46
4.2.3	Product variations of rollers	46
4.2.4	Influence of lubrication	47
4.2.5	Variation of contact length	48
4.2.6	Variation of roller diameter	48
4.2.7	Variation of the number of rollers	49
4.2.8	Influence of roller material	50
4.2.9	Influence of the rail surface finish	51
4.3	Relating the experimental data to theory	53
4.4	Synopsis	55
5	Stiffness of a roller between two rails at 45°	57
5.1	Description of the roller-rail system at 45°	59
5.1.1	LEGO demonstration	60
5.2	Test setup	61
5.2.1	Description of the setup	61
5.2.2	Multi body dynamics analysis of the setup	62
5.2.3	Test procedure	62
5.2.4	Test equipment	62
5.3	Test results and discussion	63
5.3.1	Precision of the setup	63
5.3.2	Product variations of rollers	64
5.3.3	Influence of roller orientation	64
5.3.4	Variation of contact length	65
5.3.5	Variation of roller diameter	65
5.3.6	Influence of lubrication	67
5.3.7	Variation of the number of rollers	67
5.3.8	Influence of roller material	68
5.3.9	Tangential stiffness	69
5.4	Relating the experimental data to theory	70
5.4.1	Quantifying the tangential stiffness	70
5.4.2	Individual stiffness components compared to 45° measurements	71
5.4.3	Modelling a roller at 45°	72
5.5	Synopsis	73
6	Stiffness of a linear crossed roller bearing	75
6.1	Description of the crossed roller slide	76
6.2	Test setup	77
6.2.1	Description of the setup	78
6.2.2	Test procedure	78
6.2.3	Test equipment	78
6.3	Model	79
6.3.1	Numeric multi body dynamics model	79
6.3.2	Parametric multi body dynamics model	80

6.4	Test results and discussion	83
6.4.1	RT-3150, stiffness in z-direction	83
6.4.2	RT-3150, stiffness in other directions	84
6.4.3	RT-15100, stiffness in z-direction	85
6.4.4	RT-3150, rollers in tension	85
6.5	Synopsis	86
7	Conclusions and recommendations	87
7.1	Conclusions	87
7.2	Recommendations	89
A	Specification of rolling elements	91
B	Setup components	93
C	Multi body dynamics analysis of the normal test setup	95
D	Uncertainty and error analysis of the normal test setup	99
E	Results with capacitive sensor for normal test setup	103
F	Post hoc analysis on normal measurements	105
F.1	Univariate Analysis of covariance	105
F.1.1	Statistical assumptions	105
F.1.2	Results	106
F.2	Descriptives table for all normal measurements	108
G	Test setup for measuring individual stiffness components	109
G.1	Results	111
G.1.1	Influence of roller orientation	111
G.1.2	Variation of the number of rails	111
H	Post hoc analysis on 45° measurements	113
H.1	Univariate Analysis of covariance	113
H.2	Descriptives table for all 45° measurements	114
I	Test setup for measuring crossed roller slides	115
I.1	Parameters	115
I.2	Drawings	116
J	Multi body dynamics analysis of test setup for measuring crossed roller slides	117
K	Post hoc analysis on crossed roller guide measurements	119
K.1	Descriptives table of all measurements with the crossed roller guides	122
	Bibliography	123

1

Introduction

Linear crossed roller bearings play an essential role in the high tech industry, this kind of bearing is used for precision applications such as microscopes, optical systems and semiconductor production equipment. The performance of all these systems is related to the ability to produce and control a certain motion of a body. Bearings facilitate this motion, they are designed such that the resistance in the direction of movement is minimal. Generally, in all other directions, the bearing should be as stiff as possible as a high bearing stiffness is beneficial for controlling the motion. Stiffness is beneficial as it contributes to achieving a high control bandwidth and minimizes sensitivity to external forces or vibrations.

Mechatronic systems have to meet very strict targets in terms of positioning accuracy and settling times. The dynamics of mechatronic systems is dominantly dependent on the performance of their bearings [1]. Nowadays, the performance of a machine is predicted before building the physical machine through virtual prototyping. Virtual prototyping is becoming increasingly important: an accurate model in an early stage of a development project minimizes the risk of not achieving specifications in a later stage. For accurate modelling of precision machines using linear cross roller bearings, reliable data on the stiffness characteristics of these bearings is required. This thesis aims to assist mechatronic system integrators with virtual prototyping by providing a method to predict the stiffness of linear (crossed) roller bearings.

Rob Eling's doctoral thesis "*Towards robust design optimization of automotive turbocharger rotor-bearing systems*" [2] has been of enormous help, it inspired both the project approach as the structuring of this Thesis.

1.1. Bearings

A bearing is a machine element which constrains the degrees of freedom of a mechanical system. A bearing has a dual function, it prevents motion in specific directions by bearing a load and it allows movement in the other direction by minimizing friction.

1.1.1. Bearing principles

Minimizing friction in a bearing is vital for its efficacy. It reduces wear, facilitates operation at high speeds for longer periods of time, prevents excessive heat generation and minimizes premature bearing failure. Essentially, there are five working principles for bearings [3]:

Material This principle relies on the surface friction of the bearing materials. Using a material with low surface friction enables a sliding contact. This is the simplest, oldest and often least expensive bearing principle. The large contact area between the bearing surfaces makes sliding bearings extremely stiff and capable of carrying high loads. However, this bearing principle yields higher resistance and stick compared to other principles, making it less suitable for high speed or precision applications.

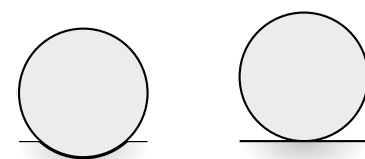
Fluid This principle relies on moving a pressurized fluid between the two bearing surfaces, creating a thin low viscosity fluid film. As the two components are not in mechanical contact, there is no dry friction. The load is supported by the pressure of the moving fluid. The friction in fluid-based bearings is low, constant and predictable. Together with a high stiffness and load capacity, these bearings are advantageous for particular high-end applications. However, the need for auxiliary apparatus and power to pressurize and recirculate the fluid makes this type of bearing costly and only suitable for certain applications. In hydro-static bearings, the pressure is maintained externally (e.g. a pump). In hydrodynamic bearings the pressure is created by the velocity of the bearing surfaces themselves.

Gas This principle is similar to that of a fluid bearing but uses pressurized air instead of fluid. The low viscosity of air causes the friction of this type of bearing to be low, thus making them suitable for high speed and high precision applications. Unlike fluids, gas is a compressible medium, making this bearing principle substantially more compliant. On the other hand, using air makes in many applications a the use of a recirculatory system superfluous. In aerostatic bearings, the bearing is externally pressured. In aerodynamic bearings, the gas is brought under pressure by the relative velocity between the bearing surfaces.

Electromagnetism This principle relies on the exploitation of electromagnetic fields to actively levitate bearings surfaces. In the absence of physical contact, there is no mechanical wear and very low friction. These types of bearings are capable of handling high speeds. However, the use of electromagnets makes this type of bearing costly and complex. Instead of electromagnets, permanent magnets can also be used.

Shape This principle utilizes geometry. The relative motion of bearing surfaces is converted into the rotation of rolling elements, in this way the friction is reduced to rolling friction. As rolling elements, either balls (spheres) or rollers (cylinders) are used. The geometries of the rolling element and bearing surfaces are non-conforming¹, the contact is concentrated as the contact area is small compared to the dimensions of the rolling element. For a spherical rolling element (ball bearings) an initial point contact grows as the load increases into an elliptical or circular contact area. For cylindrical rolling elements (roller bearings), an initial line contacts develops into an infinite strip or elliptical contact area. Typically, roller bearings are stiffer and have a higher load-rating than ball bearings, at the cost of a slight increase of friction. Rolling bearings are the most common type of bearings, both for rotation and linear motion, as they possess a favourable trade-off between cost, load-rating, stiffness, speed rating and durability.

In contact mechanics a distinction is made between conforming and non-conforming contacts. A contact is conforming when the surfaces of bodies "fit" without deformation, the initial contact is extended over an extended region. Bodies with mismatched profiles are non-conforming, the contact is initiated at one or more isolated points and the eventual contact area is dependent on the deformations of the bodies. Figure 1.1a shows a sphere in a conforming contact with a cavity of the same radius. Figure 1.1b shows a sphere in non-conforming contact with a plane surface.



(a) Conforming (b) Non-conforming
Figure 1.1: A conforming and non-conforming contact.

1.1.2. Types of rolling bearings

Figure 1.2 shows different types of rolling bearings. A main distinction is made between bearings where the principal degree of freedom is continuous rotation about an axis and those wherein the principal degree of freedom is continuous translation along an axis; these are called rotation rolling bearings and linear motion rolling bearings respectively.

Rotation rolling bearings Figure 1.2a and 1.2b show two rotation rolling element bearings. Generally, these consist of two bearing rings that incorporate a rolling track which is called a raceway. The rings are separated by a number of rolling elements. A cage ensures the distribution of these rolling elements, it prevents them from touching each other. Two distinctions are made. The first depends on the type of rolling element used; roller or ball bearings. The second depends on the direction in which the bearings are designed; to primarily support a load, perpendicular to or along the axis of rotation; these are called radial and thrust bearings respectively. Rolling bearings that support a combination of radial and axial load, are called angular contact rolling bearings.

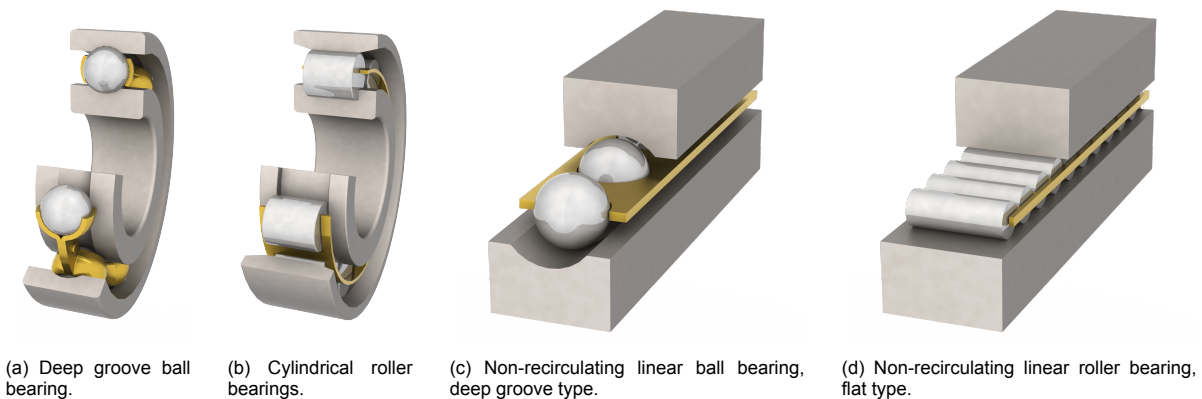


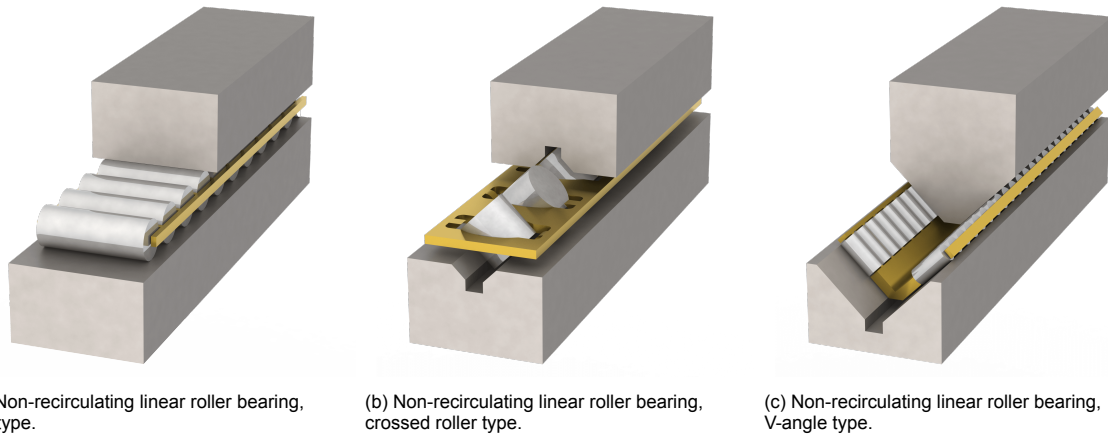
Figure 1.2: Example of two rotation and two linear bearings.

Linear motion rolling bearings Figure 1.2c and 1.2d show two linear motion rolling bearings. These bearings are based on the same working principle as rotation bearings, but facilitate translation instead of rotation. The rolling elements are placed between the two bearing guide ways. The rolling elements are pressed against the races and transmit the load.

Linear motion rolling bearings fall into two categories, recirculating and non-recirculating. Recirculating bearings have rolling elements that pass through the bearing and recirculate. This circulation allows for travel over the full length of the rail (unlimited stroke) and facilitates compact design. When the elements do not recirculate, the rollers travel half the distance of the moving rail, such that the stroke is limited to less than half of the rail length (limited stroke). The rolling elements in recirculating bearings move from the circulation zone to the loaded zone, the transition of elements between these zones causes vibration.

In limited stroke bearings all rolling elements are loaded continuously, providing an extremely smooth motion. Figure 1.3 shows the most prevalent types of non-recirculating linear motion bearings. Flat type bearings provide extremely high rigidity and high linear motion accuracy in one direction but only constrain motion in that same direction, they are mainly used on flat surfaces. The rolling elements of these bearings are often called needles as the diameter of is often small relative to their length. As needles are more compact, more needle rollers can be used in a cage to distribute the load, making the bearing more rigid and capable of carrying high loads.

Crossed roller bearing configurations are often used for accurate linear motion. Here, cylindrical rolling elements are positioned between two linear guide ways. Each guide way has V-groove raceways, having each roller positioned with its axis crosswise in relation to adjacent rollers. Effectively, the crossed roller bearings combines two sets of bearings and races at right angles to each other.



(a) Non-recirculating linear roller bearing, flat type.

(b) Non-recirculating linear roller bearing, crossed roller type.

(c) Non-recirculating linear roller bearing, V-angle type.

Figure 1.3: Example of three linear roller bearings.

1.2. The relevance of bearing stiffness quantification

It is important to have a good understanding of the stiffness of a bearing. Generally, bearing stiffness should be as high as possible. A limited bearing stiffness leads to deformations that cause machine errors. Furthermore, it also affects the dynamic behaviour of the machine, causing eigenfrequencies to be lower than desired, that trigger undesirable resonances [1]. In feedback controlled applications, the dynamic bandwidth is often limited by bearing stiffness [1].

1.2.1. The definition of stiffness

Stiffness is the extent to which a structure resists a certain deformation in response to an applied force. Hookes law defines the relationship for elasticity of an object. It equals the incremental change in force $\Delta \vec{F}$ that an elastic element produces in reaction to an incremental deformation $\Delta \vec{q}$. This force and displacement vector act in opposite direction. Expressed in generalised coordinates, Hookes law is defined as: $\delta \vec{F} = -\mathbf{K}(\vec{q}) \cdot \Delta \vec{q}$. Here $\mathbf{K}(\vec{q})$ is the stiffness matrix consisting of the elasticity terms for all generalized coordinates. If the stiffness of the element is independent of the deformation, the relation becomes linear and when acting in one single degree it can be written as: $\vec{F} = -\mathbf{K} \cdot \vec{q}$.

As the degrees of freedom of a system increase, the stiffness matrix becomes increasingly complicated. For bearings the stiffness in the degrees of freedom that it constrains is of interest, here stiffness is a measure of how well these degrees are constrained.

1.2.2. The role of stiffness in mechatronic system performance

Mechatronic systems performance of is often related to the ability to produce and control a certain motion of a body. As external forces are exerted on the body, reaction forces need to be generated to keep the body on track, i.e. it requires a stiffness. Constant external forces pose no real problems. In practice however, these forces are not constant, this makes controlling them difficult. The movements and forces vary in different ways both periodic and as a random process, therefore they are analysed by studying the system response to input forces of different frequencies.

Despite many decades of fine engineering, improving the mechanical construction in strength, lifetime and mass, the mechanical aspect of a mechatronic system is still the limiting factor of the performance of any mechatronic system [1]. It is therefore first and foremost essential to fully understand the system mechanics. The overall performance of a mechatronic system regarding speed and precision is determined by the static and dynamic properties of all elements making up the system.

1.2.3. Stiffness in relation to static system performance

Stiffness is a highly important property for reaching certain performance levels regarding positioning accuracy. Stiff systems will deform less in response to an exerted force. A high stiffness is often necessary for precision, minimizing random errors resulting from variations in forces.

An example of a system where a high stiffness is essential for performance is a motion stage in a wafer inspection machine, as shown in figure 1.4. Depending on the stiffness of the motion stage, the wafer moves away further from the targeted position due to the force of the load exerted on the stage. The force and related offset are rarely constant and accurately known. This limits both the accuracy and precision of this machine. In case a maximum deviation (positioning error x_e) of $1 \mu\text{m}$ is specified, and a force of 20 N is exerted by the load in x -direction, a minimum for the stiffness between motion stage and support frame of $2 \cdot 10^7 \text{ N/m}$ directly results from this requirement.

1.2.4. Stiffness in relation to dynamic system performance

Going back to the example of the wafer inspection equipment in figure 1.4, when performing the a task faster, the increased acceleration, together with the inertia of the moving components will generate higher internal force. These pseudo-forces directly pose a minimum on the stiffness between the motion stage and the support frame to limit the maximum error:

$$k \geq \frac{F}{x} = \frac{m a}{x} \quad (1.1)$$

For harmonic motions, the minimal stiffness is directly coupled with the undamped natural frequency ω_n . A system in balance, consisting of a body with a certain mass and compliance, will resonate in its natural frequency. The inertial force F_a will always be in balance with the reaction force from the bearing F_b , this can be written as:

$$F_a(t) + F_b(t) = m \frac{d^2 x}{dt^2} + k x(t) = 0 \quad (1.2)$$

When in resonance, the element has a harmonic movement of the form $x(t) = x_p \cdot \sin(\omega_0 t)$. Here, x_p is the peak amplitude. When substituting the harmonic movement in Equation 1.2, the following equation can be formulated:

$$-m x_p \omega_n^2 \sin(\omega_n t) + k x_p \sin(\omega_n t) = 0 \quad (1.3)$$

Equation 1.3 results in:

$$\omega_n = \sqrt{\frac{k}{m}} \quad (1.4)$$

From Equation 1.1 it can be understood that a smaller positioning error requires a higher stiffness. Which implies that the undamped natural frequency, Equation 1.4 has to increase. This illustrates how the natural frequency of a system is linked to its performance with regards its ability to deal with vibrations.

The eigenfrequency relates in a similar way to the performance of a feedback system tracking a reference. The maximum tracking frequency of a mechatronic system is called the control bandwidth. In the example of the wafer inspection machine, if the motion stage is perturbed with a high frequency; above the bandwidth, the error caused by this vibration adds up to the measurement error and the stage is not able to react on this input.

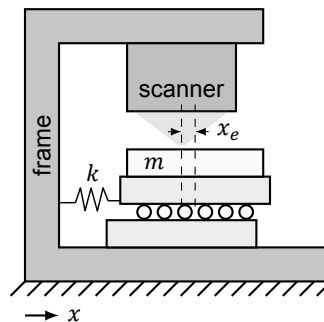


Figure 1.4: A wafer inspection machine tracing a waver along the microscope lens.

1.3. Research goal

Section 1.2 explained the relevance of quantifying bearing stiffness. This thesis aims to assist mechatronic systems integrators in performing virtual prototyping by providing stiffness estimations of linear crossed roller bearings. The final goal of this master thesis is stated as follows:

To create and validate a model for predicting the static stiffness of a linear crossed roller bearing as a function of its key design variables within a range of 20 %.

The scope of this thesis is limited to non-rolling, conditions, consequently excluding the effects as Elastohydrodynamic Lubrication and spin creepage. Furthermore, this thesis will not cover the mechanisms for applying preload and their corresponding error.

1.4. Structure of this Thesis

- Chapter 2 provides a literature review of fundamental concepts of rolling element bearings relevant for this study. It summarizes current knowledge of stiffness modelling for roller bearings and identifies open questions.
- Chapter 3 presents a first modelling effort of the roller-rail contact. The purpose of this study is twofold, first to determine which physical effects determine behaviour of roller-rail contacts. Secondly, to develop a method to accurately and computationally efficiently predict the stiffness of an individual roller-rail contact as part of a system.
- Chapter 3 validates this method with experiments on normally loaded rollers between two rails.
- Chapter 5 extends the model of the normally loaded situation of Chapter 3 and 4 to a configuration in which the rollers are loaded with an angle of 45° . Here the role of tangential stiffness components is investigated and quantified.
- Chapter 6 extends the model from single rolling elements to a full linear roller bearing assembly. This Chapter presents both a parametric and numeric multi body dynamics model based on the method and experimental data obtained in the previous chapters. Experiments on crossed roller slides evaluate the accuracy of this model.
- Lastly, an overview of the developed insights is given in Chapter 7, these conclusions are followed by recommendations on any further research.

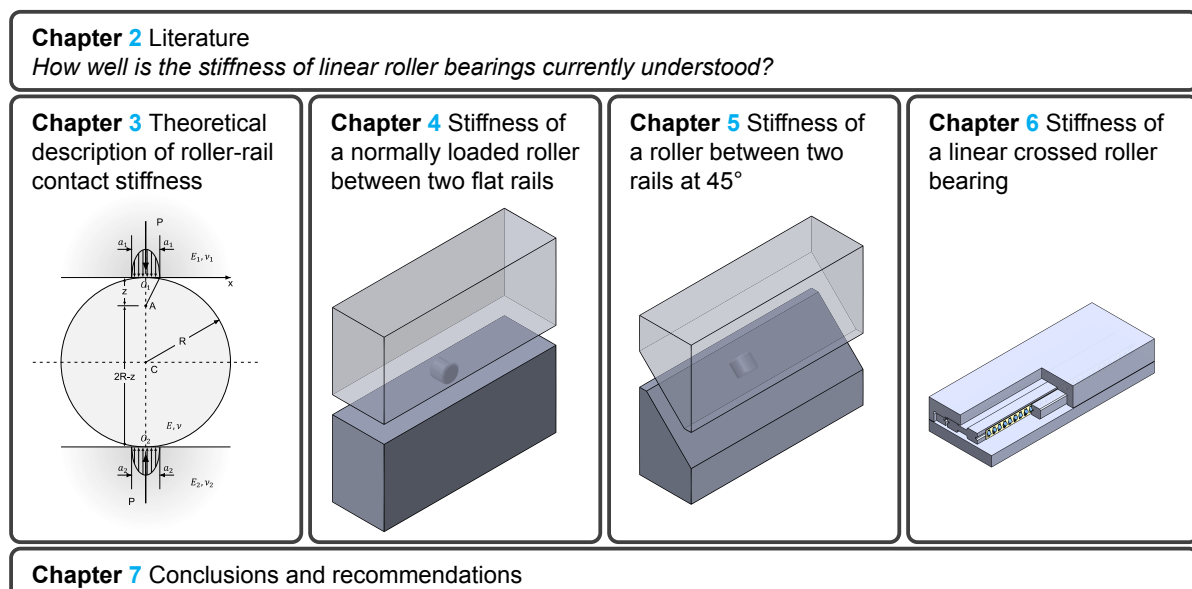


Figure 1.5: Structure of this thesis.

2

Literature

How well is the stiffness of linear roller bearings currently understood?

This literature review will elaborate on this question. First it will provide a brief history on rolling element bearings. Secondly, Section 2.2 covers the different methods for modelling the load-deflection relation of individual rollers. This includes the analytic fundamentals of Hertz Theory and its extension to 2D line contacts. This Section will cover the most common analytic models of the roller-rail contact in 2D. The study is extended to 3D, it will cover the effects such as roller profiling, end-effects, and misalignment.

After this, factors that influence the stiffness as surface roughness, lubrication and traction are covered. Section 2.7 elaborates on the modelling and experimental validation of bearing assemblies. Finally, Section 2.8 identifies open research questions.

2.1. A brief history of rolling element bearings

Efforts to replace sliding with rolling contact appear to have started already in the prehistoric age. Round wooden logs were used to transport stones for the construction of Megaliths like the Dolemens found in the Netherlands. This can be considered the first utilisation of a "linear roller bearing". It is disputed whether the Egyptians used a similar technique to transport stones up their pyramids. According to Rossi [4], the Celts used rolling elements in hubs of war chariots where the bearings consisted of a series of rollers placed between the hub and the axle. Larger rolling element bearings were used by the Romans as the finding of several roller bearings and ball bearings on the remains of Nemi's ships [4] indicated. Here the elements were installed between two horizontal circular platforms which appeared to function as a mobile base for valuable statues or used as a platform in a cargo crane.

The first concepts for rolling elements bearings in the form as we know today date back to the Renaissance; they were found in the work of Leonardo da Vinci [5]. In 1757 the first caged roller bearing was used in the H3 marine timekeeper which was invented by John Harrison [6]. The first patent for a roller bearing was granted to Philip Vaughan in 1794; UK Patent No 2006, London. 1794. "*Iron ball bearings for carriage wheel-axles*" [7]. However, the general, widespread use of rolling bearings did not occur until the Industrial Revolution as rolling element bearings could initially not compete in durability with hydrodynamic sliding bearings [8].

In 1907 SKF was founded by Sven Wingqvist who invented the self-aligning radial ball bearing that revolutionized the rolling element bearing. This is a type of bearing in which misalignment does not cause excessive wear [9]. Today, SKF is the world's largest bearing manufacturer. Throughout the 20th century rolling element bearings improved substantially with the development of superior rolling bearing steels and improvements in manufacturing that led to the production of extremely accurate geometries. Many variations of the rolling element bearing were developed during this period, linear and recirculating rolling element bearing were found in widespread applications. Standardization, automated mass production and global competition drove prices down which led roller bearings to become the most commonly used motion bearing. In 1941 the first patent for a linear crossed roller bearing was granted to Zwick [10], in 1948 the company Schneeberger started the first production of crossed guide ways and crossed roller slide tables [11].

Since the 90s a trend can be observed that linear roller bearings are reduced considerably in size. This follows the miniaturization in precision applications such as microscopes, optical systems, and semiconductor production equipment. Up to this day, this miniaturization demands higher requirements on the accuracy and predictability of linear rolling bearings.

2.2. Individual roller-rail contact models

The relationship between load and deformation is one of the most important issues in the field of rolling element bearing modelling [12]. For non-conforming contacts, the stresses very close to the point of contact are extremely large compared to the rest of the bodies. Therefore, when studying contact mechanics, the focus is usually confined to this section of the bodies. In contact stress theory it is common to treat the concentrated stress near the surface and the distributed load throughout the bodies separately [13].

In general, there are three methods that are widely used to determine the load-deflection relation in individual roller-rail contacts:

- **Analytic** models are typically extensions of Hertz Theory and a 2D analytic solution of the simplified mechanics problem based on the geometry and mechanics of the materials. Analytic models provide an elegant equation for the load-deflection relation but do so at the cost of many assumptions and simplifications.
- **Numeric** models allow to take into account the complex geometry and capture (local) effects including lubrication, surface roughness, and misalignment. These comprehensive models can model the many factors that govern the roller-rail contact. But they require an exact description of the geometry and are computationally expensive as they need to be numerically solved for each unique condition. These computational costs can limit the practical use of numeric models.
- **Empiric** models take into account all effects that influence the contact in practice thus no assumptions on the roller-rail contact have to be made. This method requires extensive experimental work which consumes time and labour. In addition, experiments introduce measurement errors, and inter-or extrapolation for all configurations not tested for.

2.2.1. Analytic models

A simplified geometry of an individual roller in a bearing assembly is a cylinder compressed between two rails. The most simplified model is to consider the situation where a cylindrical body is compressed between two rectangular bodies. When neglecting dynamics, lubrication, and surface asperities, only the geometry and mechanics of the materials determine the behaviour.

Heinrich Hertz with his paper *Ueber die Berührung fester elastischer Körper* [14] (*On the contact of elastic solids* [15]) is considered the founder of the subject of contact mechanics. As a result, these type of contacts are called Hertzian contacts (even when Hertz Theory cannot be applied). His interest in the problem of contact mechanics was aroused by optical interference experiments on contacting glass lenses. He was interested the influence of the load on the lenses on the interference pattern. He derived the formulae for calculating contact pressures and the dimensions of the concentrated contacts between two elliptical non-conforming bodies.

For point contacts Hertz provided an analytic solution for the load-deflection relationship. A cylinder is treated using Hertz Theory as the limit of an elliptical body where one radius goes to infinity, creating a line contact in plane strain. For this contact, the load-deflection relationship falls outside the realm of Hertz Theory. Here, it merely allows for calculation of the stress and strains in the vicinity of the contact. Over time, many authors addressed contact problems involving cylindrical bodies, all with slightly different assumptions and boundary conditions. A standard reference on the subject of contact mechanics is written by Johnson [13].

Tripp [16] derived a solution for the deformation of a 2D cylinder compressed between two half-spaces, a semi-infinite bodies bounded by a plane surfaces. The deformation of this infinitely deep half space can only be calculated in relation to a chosen evaluation depth. Nakhatakyan [17] derived a load-deflection relation identical to Equation 3.33 by means of a different but very clear model. This model is more commonly known as Johnson's model [13], however Johnson credits Tripp for this model. Throughout this Thesis it will be referred to as the Tripp model.

One major simplification of the Tripp model is the assumption of plane strain, this reduces the problem to 2D as a result this model does not consider effects at the roller ends. The Tripp model accurately models the bulk of the length of the roller, however rollers in bearings are of finite length, at the roller ends significant deviations are found. In most applications, the edge stresses have an important effect [13]. The stresses at a sharp edge as shown in Figure 2.1a are often more than twice the stress at the rest of the length [18]. These stress concentrations strongly influence the fatigue life of roller bearings as they initiate fatigue cracks [3]. To reduce the effect of the discontinuity at the end of the straight profile and distribute the load more consistently across the length of the bearing, roller profiles are modified, this is also known as crowning. Rollers have various lengths and profiles, different types of profiles are shown in Figure 2.1. These profiles, together with the assumptions for the boundary conditions of the rail constitute the basis of the differences between the many load-deflection models available.

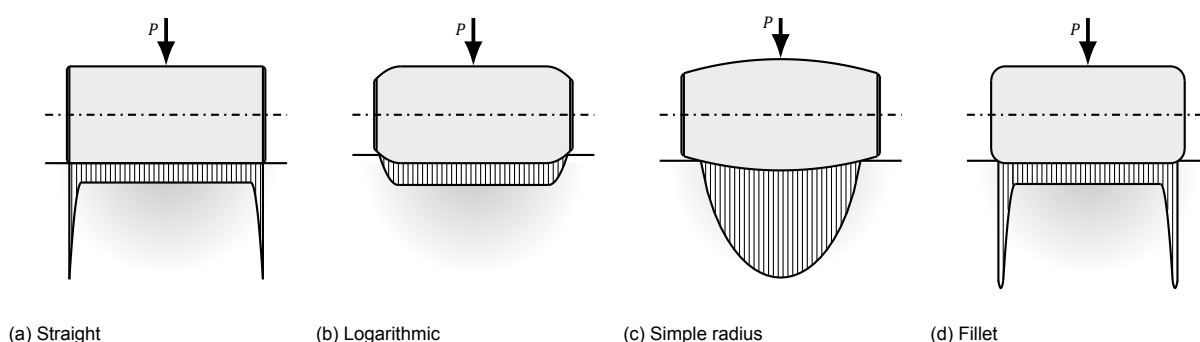


Figure 2.1: Different roller profiles. The profiles are only present at the micrometer scale, this is an exaggeration.

In 1939, Lundberg [19] was the first to suggest a profile to distribute the stress as uniform as possible, he proposed a logarithmic profile as shown in Figure 2.1b. Doing so, he assumed that the pressure distribution is constant along the roller axis. He uses deflection differences in order to obtain this profile. Lundberg also presented a load-deflection relation corresponding to this profile. An essentially identical profile is included in *ISO/TS 16281* (see Section 2.5). Kunert [20] proved Lundberg's profile as part of his dissertation in 1961. Kunert also presented a greatly simplified approximation of Lundberg's load-deflection relation. In addition, he also described how, when also considering subsurface stress concentrations and not only contact pressure, it is not possible to have a completely uniform stress distribution along the cylinder's axes. The optimum profile depends the loading conditions, therefore the logarithmic profile is of limited practical use.

The pressure distribution resulting from a barrel type roller with a simple radius (Figure 2.1c) is an elliptically distributed pressure, that can be solved using Hertz Theory. The disadvantage of this profile is that under light loads the circular crowned profile does not fully utilize the roller length. The load-deflection relation is given by Kowalsky¹.

The foregoing load-deflection relationships were compared by Teutsch and Sauer [21], in their case study only Lundberg's and Kunert's results deviate noticeably. This is expected since both relationships assume an optimized roller profile.

2.2.2. Numerical models

Many numerical models have been developed to estimate the interaction forces in roller-rail contacts. FEM models allow to model the complex geometry, capture local effects such as lubrication [23], surface roughness [24], misalignment [25], creep [26], spin, friction and wear. Each of the mentioned aspects can be solved with different methodologies; over the years many alternative methods were proposed. Typically, the most accurate and comprehensive models come with higher computational costs while simplified models come with larger errors. Most of these aspects are interdependent, such that complex models require simultaneous evaluation of the relevant sub-problems. These comprehensive models can model the many factors that determine the roller-rail contact, but require an exact description of the geometry and are computationally expensive as they need to be numerically solved for each unique condition.

The first successful numerical model of wheel-rail rolling program was proposed by Kalker [27] in the 1970's. He is the initial developer of CONTACT [28], a software tool for the numerical simulation of rolling contact situations, focused on railway applications. A standard reference on the subject of numerical contact modelling is written by Kalker [29].

The slicing method [21] is a method combining analytic and numerical models, the roller-rail contact region is sliced into a number of sections. The total contact forces and deformations are then calculated by the summation of deformations and loads in the individual slices. This is a relatively cheap method to include aspects such as misalignment and end-effects. The use of some slicing method can be advantageous when many contacts have to be solved simultaneously such as in a bearing assembly. However, compared to full numerical modelling, the accuracy may be reduced considerably.

¹Teutsch and Sauer [21] stated that Kowalsky considered an elliptically distributed pressure, they refer to Rothbart's book *Mechanical Design and Systems Handbook* [22]. Unfortunately after lending this book at the library, no single reference to Kowalsky. Neither is he mentioned in any other literature.

2.2.3. Experimental work

The classic method for measuring the load-compression relation is by statically loading a roller between two bodies with a flat surface, followed by measuring the deformation for different loads. A schematic of a typical test setup for this measuring method is shown in Figure 2.2a. This method is used by various authors (Nikpur et al. [30], Hoeprich and Zantopoulos [31]) and has shown good agreement with analytic work in some situations. However, often large discrepancies were measured with errors of over 40 % [31]. The rollers used were profiled [30] and the quality of the rollers and rail was not specified.

H. A. Sherif [32] proposed and demonstrated an elegant and promising experimental method to measure the stiffness of a roller between two plates using modal analysis. A schematic of his test setup is shown in 2.2b. His results were promising for small rollers. However, the asymmetric setup design inherently led to misalignment, resulting in large measurement errors. In addition, the limited mass led to the roller mass influencing the measurements for larger rollers. He used profiled rollers with a large diameter and length. The paper documents the rail and roller roughness, and material hardness, however the roller cylindricity is not specified. This setup requires the assumption of zero deformation of the setup base.

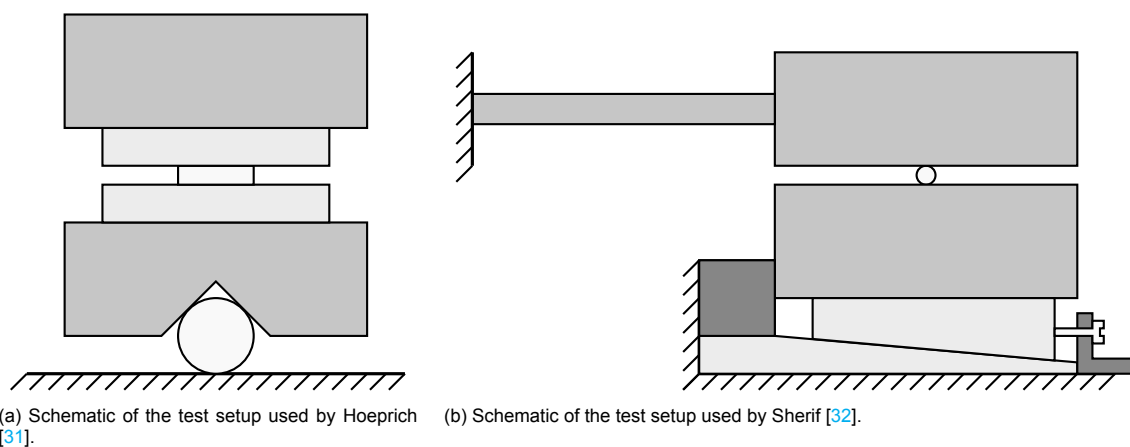


Figure 2.2: Schematics of test setups used for measuring the stiffness of individual rollers.

Palmgren [33] (head of SKF's technical department between 1937 and 1955 [34]) presented a load-deflection relation which by many authors [8, 12, 21, 32, 35] is believed to be based on laboratory testing of rollers loaded against raceways. However, as Nikpur et al. [30] point out, this load-deflection relation is² only a simplification of the analytic solution presented by Lundberg [19].

²All authors refer to *Ball and roller bearing engineering, 3rd edition*. After lending this book at the library, both in German and in English, it becomes clear that no experimental verification is mentioned. The relation Assumes a cylindrical body of infinite length, while the relation itself depends the roller length.

2.3. Surface roughness

Both Hertz contact theory as the extensions for rollers assume perfectly smooth contacting surfaces. These models are incomplete for real-world situations where two rough non-conforming bodies are brought into contact. Whether the assumption of smooth surfaces is justifiable, depends on the width of the contact relative to the dimensions surface asperities. For a contact concerning a rolling element with a large radius, high load, and small surface asperities, the influence of these asperities is relatively small.

In smooth non-conforming contacts, the stress is continuously distributed over the contact area. While in rough contacts only the asperity peaks are in contact, such that the contact occurs at a finite number of asperities. This reduces the effective contact area which ultimately results in a lower stiffness.

Surface roughness is predominantly studied in relation to the ways in which it influences surface stresses that impact the wear and fatigue life of rolling contacts. A classical study published by Greenwood and Tripp studied the influence of surface roughness on the elastic contact between smooth spheres and rough surfaces [36]. Here the Greenwood–Williamson [37] contact mechanics theory is applied to Hertz contacts. They found that the influence of surface roughness with regards to the stiffness scales dominantly with $(\frac{R}{p^2})^{\frac{1}{3}}$.

Greenwood and Tripp assumed:

- The asperities have spherical crests with a specified constant
- The crest heights follow a Gaussian distribution with a specified standard deviation
- There are taken to be specified number of asperities per unit area
- The deformations are elastic, there is no plastic flow

Machined surfaces after run-in are often assumed to have profiles that are described by a Gaussian distribution [37]. For bearings it is reasonable to assume plastic flow during the run-in. Since bearings make millions of traversals during their lifetime, it is logical to assume a steady state in which the rolling element is supported elastically. Kagami et al. [38] provided an analysis of this problem and found that the effect of the mode of deformation, the assumption of elastic, plastic or mixed deformation was of little importance.

The above-mentioned models exclusively considered spheres and none of these measured deformation. Solely the relation between roughness and contact area is measured, all other contact characteristics were deduced from this measurement. The majority of the studies on roughness is concerned with the effects on wear and failure of the bearing.

McCallion [39] presented a procedure to predict the deformation of a rough-turned circular cylinder compressed between smooth flat surfaces of two hard blocks. He verified his model by performing experiments with rough turned rollers and smooth rails. He found a good agreement between the predicted and measured influence on stiffness. His model is based on the assumption of plastic deformation of the asperities. Plastic deformations however do not create a stiffness as this requires elastic deformation. The hardness of the rollers used, were between 30 HRC and 77 HRB while a harness of 60 HRC is typical for rolling bearings.

The influence of surface roughness on roller-rail contacts has been studied with regards to the vibrations induced by the rolling over a rough surface [40], the relation with EHL [23] and roughness and with regards of wear of train-wheels [41].

summarized, there are many analytic and numerical theories that predict the behaviour of rough contacts. Yet, adequate experimental verification of these models is lacking. The influence of surface roughness of balls is not directly measured yet. For roller contacts the verification is very limited and performed with large and relatively soft rollers.

2.4. Lubrication

Lubrication of rolling contacts reduces the friction caused by micro slip [3]. Elastohydrodynamic lubrication (EHL) is present in all lubricated components whose elements roll together. Properly lubricated rolling bearings have a thin lubricant film with a height in the order of 0.1–0.5 μm while in motion. This film separates the contacts and protects the surfaces against wear and pressure concentrations caused by surface roughness [23]. The high contact pressures (order 1–4 GPa in roller contacts) increase the viscosity such that the film layer behaves rather as a solid instead of a liquid [3]. Spikes [42] gives a good overview of EHL for both point and line contacts.

Two relevant properties of EHL contacts are the film thickness of the and friction [3]. These two properties can be determined with numerical models of the elastohydrodynamic problem. Yet this requires detailed knowledge of the geometry, rheology and can be computationally expensive. A dry contact roller is stiffer than the lubricated roller, since the lubricant oil film adds a layer with a finite stiffness in series. No useful analytic solutions of the EHL problem exist to this day, instead regression-fitted equations have been developed from repeated numerical models and run over a wide range of contact and material conditions [43]. A often used film thickness equation is given by Dowson [44] which is based on three dimensionless parameters for the speed, material and load respectively:

$$\bar{U} = \frac{U^{D/2}\eta_0}{E'}, \quad \bar{G} = \alpha_p E', \quad \bar{W} = \frac{P}{E'^{D/2}L_{we}} \quad (2.1)$$

With U the velocity of the contact, base viscosity η_0 and pressure-viscosity coefficient α_p .
And a central film thickness h_c of:

$$\frac{h_c}{D/2} = 3.11\bar{U}^{0.69} \cdot \bar{G}^{0.56} \cdot \bar{W}^{-0.1} \quad (2.2)$$

It shows that these relations the film thickness is only marginally dependent on the load P . Taking the derivative towards the load gives:

$$k_{EHL}^{-1} = \frac{d}{dP}(-h_c) = D/2 \cdot 0.311 \cdot \bar{U}^{0.69} \cdot \bar{G}^{0.56} (E'^{D/2}L_{we})^{0.1} \cdot P^{-1.1} \quad (2.3)$$

Tsuha and Cavalca [45] compared EHL for different roller profiles, they found only moderate deviations. Furthermore, they showed that the film stiffness may be approximated as independent of load. For linear crossed roller bearings the stiffness of the lubrication is two to three orders of magnitude stiffer than the contacting solids [46]. The presence of an EHL film is often verified by measuring the electrical conductivity of the contact and the thickness is experimentally determined with capacitance, ultrasonic, optical interference and fluorescence measurements.

2.5. Standards for linear motion rolling bearing

Most rolling bearings are specified according to standard specifications, this enables comparison of bearings among manufactures. The design of rolling bearings is, in part, based on ISO and DIN standards, here semi-empirical formulas are used for computing the expected bearing performance [47]. A technical committee on rolling bearings (TC4) in the International Organization for Standardization (ISO) is concerned with the standardization of all types and sizes of bearing elements based on the principle of rolling motion. The focus of ISO standards is mainly towards rotational bearings, nine of the 80 standards published under this technical commission are concerned with linear motion bearings. Six of these nine standards regard linear ball bearings, while only three also cover linear motion bearings with rollers.

ISO 24393:2008 defines terminology applied in the field of linear rolling bearings and their components. The terms used throughout this thesis are chosen in accordance with this standard.

ISO 5593:2019 is the rotation bearing counterpart of this standard.

ISO 14728-1:2017 specifies methods of calculating the basic dynamic load rating (C) and basic rating life (L_{10}) for steel linear motion rolling bearings. The life of a linear bearing is the distance travelled before any evidence of fatigue develops in the bearing material. The basic rating life is defined as the life (distance) associated with 90 % reliability using the Weibull Distribution. The basic dynamic load rating of a linear bearing is the stationary load for which it could theoretically endure for a basic rating life of $1 \cdot 10^5$ m. For linear roller bearings, the basic dynamic load rating depends the dimensions of the bearing, manufacturing tolerances, and the number of rollers. Manufacturers often specify correction factors to account for temperature, material hardness, and lubrication.

ISO 281:2007 is the rotation bearing counterpart of this standard. This standard is more detailed, it takes into account various reliabilities, lubrication condition, contaminated lubricant, and fatigue load of the bearing. This standard can be extended with *ISO/TS 16281:2008* which covers additional influencing parameters such as radial clearance and tilt.

ISO 14728-2:2017 specifies methods of calculating the basic static load rating (C_0) for steel linear motion rolling bearings. The basic static load rating is the load such that approximately a total permanent deformation of 0.0001 of the rolling element diameter occurs. At this load, the most heavily loaded rolling element-raceway contact experiences a theoretical peak surface pressure of 4000 MPa, this is roughly the yield point of hardened bearing steel.

ISO 76:2006 is the rotation bearing counterpart of this standard.

ISO 12090:2011 establishes the boundary dimensions and tolerances for a series recirculating bearings, this allows for interchangeability among manufacturers.

2.6. Preload

The majority of all high-precision applications required a preload to improve their performance. According to *ISO 24393:2008*, preload is the continuous application of force on a bearing independent of the active service load. As the load-stiffness relation has a non-linear nature, rolling element bearings perform poorly under light or no-load conditions. Applying a preload yields a higher stiffness for loaded bearings and thus improves their performance.

Besides stiffness, other reasons to apply a preload include:

- Reduce noise level and running vibrations
- Remove clearances caused by manufacturing precision
- Extend bearing fatigue life
- Improve running accuracy
- Prevent skidding in high-speed applications with heavy acceleration
- Minimize cage creep

However, excessive preload results in increased friction, wear and fatigue; a good balance is therefore important.

In linear motion roller bearings, three major methods to apply preload are used: oversized rollers, set screws or applying an external load [12].

- Using oversized rollers ensures a play-free and preloaded bearing assembly. Yet this requires extremely tight tolerances such that the preload is in the desired range.
- Instead, a preload screw can be used. For this method, the rails are compressed against the rollers with set screws. A specific torque is applied to the preload set screws before completely fixating the guide rails to the rest of the assembly. Earlier investigations (unpublished data) into the exact relationship between set screw torque and resulting guide way preload have been conducted. It was found that no definite relation between axial preload force and set screw torque can be found through the assumption of a static, invariant screw thread friction coefficient. Nonetheless, this is the method of choice for most crossed roller slides.
- An external load is sometimes used. This is often a continuous load present in the application such as the weight of a part of the system the bearing is incorporated in.

2.7. Stiffness descriptions of bearing assemblies

The fundamental differences between the geometry of rotational and linear bearings makes them different fields of study. All assemblies are composed of individual contacts and are influenced by the factors that influence individual roller contacts. Despite the similarities, there is a distinction between bearings when comparing the stiffness of rotational and linear movement. Extensive research has been conducted on rotation rolling element bearings and recirculating roller guide ways. However, very limited information is found that investigates the stiffness behaviour of crossed roller guide ways. This section will review the current knowledge of the stiffness of various linear motion rolling bearing assemblies.

2.7.1. Rotation rolling bearings

The modelling and analysis of rotation rolling element bearings has been discussed extensively in a review by Hong and Tong [12]. This literature review covers both quasi-static (steady state operation) and dynamic models. They compare 24 different dynamic rotational bearing models, the different software tools provided by manufacturers. For rotational bearings the focus is often on the influence of the rotational speed on the dynamic characteristics of a bearing. A standard reference on the modelling of rotational rolling bearings is *Essential Concepts of Bearing Technology*, written by T.A. Harris [8]. The more numerical aspects are covered by H. Nguyen-Schäfer in his work *Computational design of rolling bearings*.

2.7.2. Linear motion rolling bearings

Table 2.1 lists different models for linear recirculating rolling element guides. The straightforward nature of a point contacts and the tendency of authors to focus on modelling recirculating ball bearings, has led to fairly accurate stiffness predictions. However, for recirculating roller bearings no such accurate predictions have been presented yet.

Table 2.1: Models for linear recirculating rolling element guides.

Ref.	Authors	Year	Elements	D mm	L_{we} mm	Contact	Experiment
[48]	Hung	2009	Balls	2.778	-	Hertz	Modal analysis, hammer impact
[49]	Ohta & Hayashi	2000	Balls	4.7625	-	Hertz ^a	Modal analysis, dynamic measurements
[50]	Otha & Tanaka	2010	Balls	4.7625	-	Hertz	Static displacement measurements
[51]	Majda	2012	Balls	4.7625	-	Hertz	Static displacement measurements
[46]	Soleimanian et al.	2020	Cylindrical	4.7625	2.5	Numerical	Modal analysis, dynamic measurements
[52]	Wu et al.	2007	Balls	4.763	-	Hertz	Modal analysis, hammer impact
[53]	Li & Zhang	2011	Balls	8	-	Hertz	Modal analysis, hammer impact
[54]	Toa et al.	2013	Cylindrical	5	5	Palmgren	Static displacement measurements
[55]	Kwon et al.	2019	Logarithmic	5.5	4.3	Palmgren	None, comparison with BEARINX® [56]
[57]	Jiang et al.	2019	Logarithmic	6	5	Palmgren	Static displacement measurements ^b

^aThis may be presumed as a linear stiffness for each element is presented as a fixed bearing characteristic.

^bExperimental data from external reference in Chinese, which could not be accessed.

Hung [48] found that modelling rolling elements as spring or surface elements would be an efficient way to build a multi body model with sufficient accuracy. Moreover, it was also demonstrated that the mass of the rolling elements may be neglected in such a model.

Rolling vs non-rolling conditions Otha & Hayashi [49] studied the influence of the running velocity on the eigenmodes of lubricated recirculating ball bearings. No substantial influence of the running velocity on the main eigenfrequencies was observed.

Slide body deformations Most models neglect the deformation of the slide body, for ball linear guides this simplification is not problematic, the compliance of the Hertzian point contacts are such that they dominate the overall bearing compliance. Yet, for linear roller guides, with stiffer line contacts, the influence of slide body compliance is considerate. Otha & Tanaka [50] found that, for their specific guide, the influence of the slide body accounts for more than 20 % of the total compliance.

Geometric errors Majda [51] investigated the influence of geometric errors on of slide body and rail. It was shown how straightness error in the raceway could lead to a reduced stiffness. Yet a method for predicting the influence of error on the stiffness is still an open question.

Lubrication Soleimanian et al. [46] developed a dynamic model incorporating EHL that focuses on friction. Experimental testing validated that the film thickness always remains in the sub-micron region, exhibiting a mixed-EHL regime. This model does not consider the presence of a tangential stiffness component when no EHL is in place. The stiffness variation during a cycle of sliding velocity was less than 1 %, this is in line with the effect based on Dowson [44] covered in Section 2.4.

2.7.3. Experimental stiffness validation methods

Wu et al. [52] presented a model for linear recirculating ball guides. This study challenges the use of linear springs as contacts, it considers the nonlinear characteristics of the Hertz load-stiffness relation. The rail and carriage are taken as rigid bodies. In their experiments no external mass is added to the guide. Both ceramic and steel balls were tested, the use of ceramic balls compared to steel showed to slightly increase the overall stiffness.

In the work of Hung [48] on recirculating ball bearings, the differences between the finite element predictions and experimental measurements are less than 10 %. The preload is applied with oversized balls.

Li & Zhang [53], developed a MBD model based on Hertz Theory and the assumption of a rigid carriage. Hammer impact measurements are performed on a recirculating ball guide with the goal of identifying the stiffness. The system is tested both with and without constraint, i.e. one side fixed to a table and suspended in mid air. With the suspended experiment mainly the flex modes of the rail were measured. Yet the exact model of bearing used is not specified, making this study not reproducible. The math in paper could be incorrect, the mass and eigenfrequency do not add up to the stiffness is given. This could be a result of specifying the stiffness with 3 significant figures while mass is given with only a single significant figure. They claim that the model is correct within 5% compared to modal measurements. It is unknown how the preload, based on oversized rolling elements, is exactly known.

Toa et al. [54] studied the influence of wear loss on the displacement of the linear guide. They also measured the load-displacement relation of a slide without wear. Static measurements with a dial gauge indicator are performed in horizontal, vertical, and roll direction. Their static displacements almost exactly match the predicted displacements without incorporating the deformation of the carriage in his model. The measurement instruments used have a measuring accuracy of 1 μm and are used to compare displacements of 2 μm with predictions.

Kwon et al. [55] took a systematic approach to developing a 5-DOF model for the static analysis of linear roller bearings subjected to external loading. The model uses Palmgren's load-deflection relation as the basis for a slicing technique since rollers with a logarithmic profile are used. It takes into account the deformations of the carriage. Yet, the tangential stiffness of the rollers is not considered. The model is compared to results obtained with the commercial program BEARINX®, developed by Schaeffler Technologies AG [56]. The calculated displacements using the proposed model have a good correlation with those from the commercial program. Unfortunately no experimental data is available for this configuration.

Jiang et al. [57] created a model in a way analogue to Kwon et al. Again Palmgren's - thought to be empirical - load-deflection relation is used. The model is verified via a case study, the simulation results are compared with experimental data based on static measurements taken from a doctoral thesis written in Chinese. Their results show that the general trend of both models is similar, for nearly all measurements the difference between experiments and model is less than 40%.

When comparing the work of Hung [48] with other work it is seen that adding a large mass to the guide is beneficial for making the relevant eigenmodes distinct.

Linear crossed roller bearings

Literature on the topic of linear crossed roller bearings is very limited. Liu et al. [58] developed a parametric 5-DOF multi body dynamics model of a linear crossed roller bearing. In this model the body is assumed rigid. Each roller element is represented by a horizontal and vertical stiffness element, this indirectly allows for incorporating tangential roller stiffness. The equations of motions are derived using Lagrangian mechanics. The stiffness and damping parameters are identified experimentally through hammer impact modal testing. Additional experiments with twice the preload show a 14.5% stiffness increase, while the preload, applied with set screws, increased from 10% to 20% of C_0 .

The exact model of bearing used and the roller diameter are not specified, making this study not reproducible. In the introduction the slide body is assumed to be rigid, however, in the following finite element modelling they also consider the stiffness of this component. Only the first two eigenmodes could be identified, no mass had been added to the system to bring down the eigenfrequencies. This paper successfully identifies the parameters for the used though unspecified linear bearing.

2.8. Status quo and identification of open challenges

Modelling a roller is fundamentally more complex than a ball. Hertz contact theory is an accurate analytic solution to model the stiffness of most real ball rail contacts. On the other hand, for a roller-rail contact many factors come into play. In particular, roller profiling, misalignment, traction, and requires the arbitrary choosing of an evaluation depth. Currently, many researchers assert to present a good model for predicting the stiffness of line contacts. Yet, the experimental validation of these models is limited. A well documented empiric load-stiffness relation for cylindrical roller-rail contact is lacking.

Different methods for experimentally determining the load-stiffness relation of a roller-rail contact have been developed with varying success. No comparison between static displacement measurements and modal testing is performed. The work of H. A. Sherif [32] presents modal analysis as a promising method for measuring the contact of a roller-rail contact despite some fundamental design flaws in this test setup that hindered accurate results. Ohta et al. [49] demonstrates the benefit of adding inertia to the test setup to isolate the modes of interest from flex modes. Finally, the reliance on a perfectly fixed reference appeared to limit accuracy in most of these papers[54].

Based on experimental work with balls, the effects of surface roughness on stiffness may be expected to be in the range of 1–10%. However, experimental validation with high quality rollers is missing. The presence of EHL would in only marginally influence the normal stiffness as the nature of the EHL is two to three orders of magnitude stiffer than the contacting solids [46]. Yet it could have larger consequences as it reduces the tangential stiffness to the shear stiffness of the lubrication film. The tangential stiffness of rolling elements is measured for balls [59]. For rollers this stiffness is still an open question.

The modelling efforts for linear ball bearings using Hertz Theory resulted in accurate stiffness predictions within 10% of the measured stiffness. However, for linear roller bearings no such accurate predictions have been presented yet.

Recent linear roller bearing models claim to be able to predict the stiffness within 40% of the measured stiffness. Incomplete documentation of the experimental methods limits the reproducibility of these claims [60]. Moreover, the basis of these most recent models is Palmgren's - presumed to be empirical - load-deflection relation. However, as Nikpur et al. [30] pointed out, this relation is not empirical but a fit of an analytic solution.

Instead of extending or altering existing linear roller bearing models, this Thesis will perform a step-by-step validation of models. Starting with an empiric determination of the load-stiffness relation for an individual cylindrical roller-rail contact as this is not affected by the uncertainties present in bearing assemblies. This is followed by an analysis of the tangential effects that come into play when a roller is loaded at 45°. Once the roller-rail model at 45° is validated, this empirical roller-rail model will be used to develop a model that predicts the stiffness of linear roller bearing assemblies.

3

Theoretical description of roller-rail contact stiffness

A single roller compressed between two rails is the fundamental building block for modelling bearing assemblies. It is essential to understand the behaviour of a single roller to arrive at a model of full bearing assemblies.

The literature review of Chapter 2 showed that the following physical effects determine the stiffness of roller-rail contacts:

- Load
- Roller profiling
- Dimensions
- Young's modulus
- Poisson's ratio
- Lubrication
- Surface roughness

Most of the analytic load-deformation relations assume plane strain, are based on half-space theory and rely on the choice of an evaluation depth in this half-space. Teutsch [21] and Hoeprich [31] compared different deflection-load relationships and found only a modest discrepancy. The Tripp model [16] will be derived as it is the most common analytical solution to this problem up to this day. This model is used by many authors [3, 8, 13, 61, 62].

This chapter investigates how to practically apply the Tripp model to the finite dimensions of linear roller bearings.

First, the chapter describes the system of a normally loaded roller-rail contact.

Section 3.3 will provide an explanation and derivation of Tripp's analytical model, this model considers a 2D cylinder compressed between two half-spaces and is thus based on the assumption of plane-strain and a half-space.

Section 3.4 introduces the boundary conditions of a finite rail width (W_{rail}) and thickness (T_{rail}) with a 2D FEM model. It challenges the half-space of Tripp's model.

Section 3.5 introduces the boundary conditions of a finite roller length (L_r) and rail length (L_{rail}) with a 3D FEM model. It challenges the plane-strain of Tripp's model. This Section covers end-effects and the different roller profiles introduced in Subsection 2.2.1.

Section 3.6 presents a method to efficiently model more complex rail geometries.

3.1. Description of the roller-rail system

The geometry considered in this chapter is shown in Figure 3.1a. The total deformation of the system is the sum of the deformation in the rails and the deformation of the roller. Figure 3.1b represents the roller-rail contact modelled as a set of nonlinear springs in series.

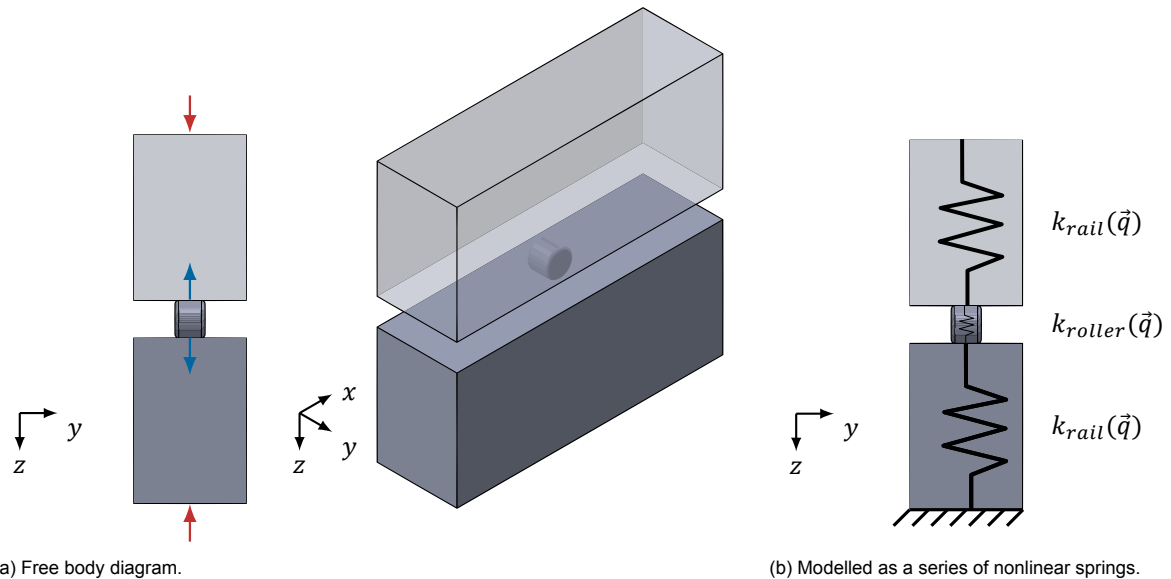


Figure 3.1: Schematic of a roller normally loaded roller between two flat rails.

The investigations in this chapter will disregard friction, tangential loading, surface roughness, and misalignment. The size of the rolling element used in this study is typical for linear bearing applications. Table A.1 lists the specifications of all roller types used throughout this Thesis. This is a simple radius (as in Figure 2.1c), made out of bearing steel (1.3505). The dimensions of the rail are shown in Figure B.1, and is also made out of bearing steel (1.3505). In models, the load is varied in steps identical as in the test setup.

The lead roller type is 1; unless stated otherwise the following parameters are used:

- Diameter $D = 3$ mm
- Roller length $L_r = 2.2$ mm
- Contact length $L_{we} = 1.793$ mm
- Young's modulus $E = 210$ GPa
- Poisson's ratio $\nu = 0.29$ (–)
- Rail thickness $T_{rail} = 22$ mm
- Rail width $W_{rail} = 100$ mm
- Rail length $L_{rail} = 15$ mm

The measured contact length of 1.793 mm is rounded during modelling to 1.80 mm for convenience.

For numerical models, when appropriate, symmetry planes are used to stabilize the model and limit computational complexity. For all symmetry planes, an identical model, but without that symmetry is constructed to verifying the conditions at these boundaries and assure if their use is appropriate. COMSOL Multiphysics 5.6 is used for all numerical models.

3.2. Modelling steps

The model is created in steps, in each step new boundary conditions are introduced.

1. The basis of the model is the analytic Tripp model [16] this is covered in Section 3.3.
2. A 2D FEM model with an actual width and thickness challenging the infinite depth and width assumed in Tripp's model. It evaluates the influence of varying these dimensions.
3. Extending the 2D FEM model to 3D introduces a finite length for the roller and rail. It tests the assumption of plane strain and it briefly covers the effects of roller profiling.
4. Subsequently, a more real-life geometry of the rail is considered and an efficient method for modelling these systems is proposed.
5. Finally this method to model contacts is applied to entire assemblies, this method is used for modelling the test setups in Section 4.

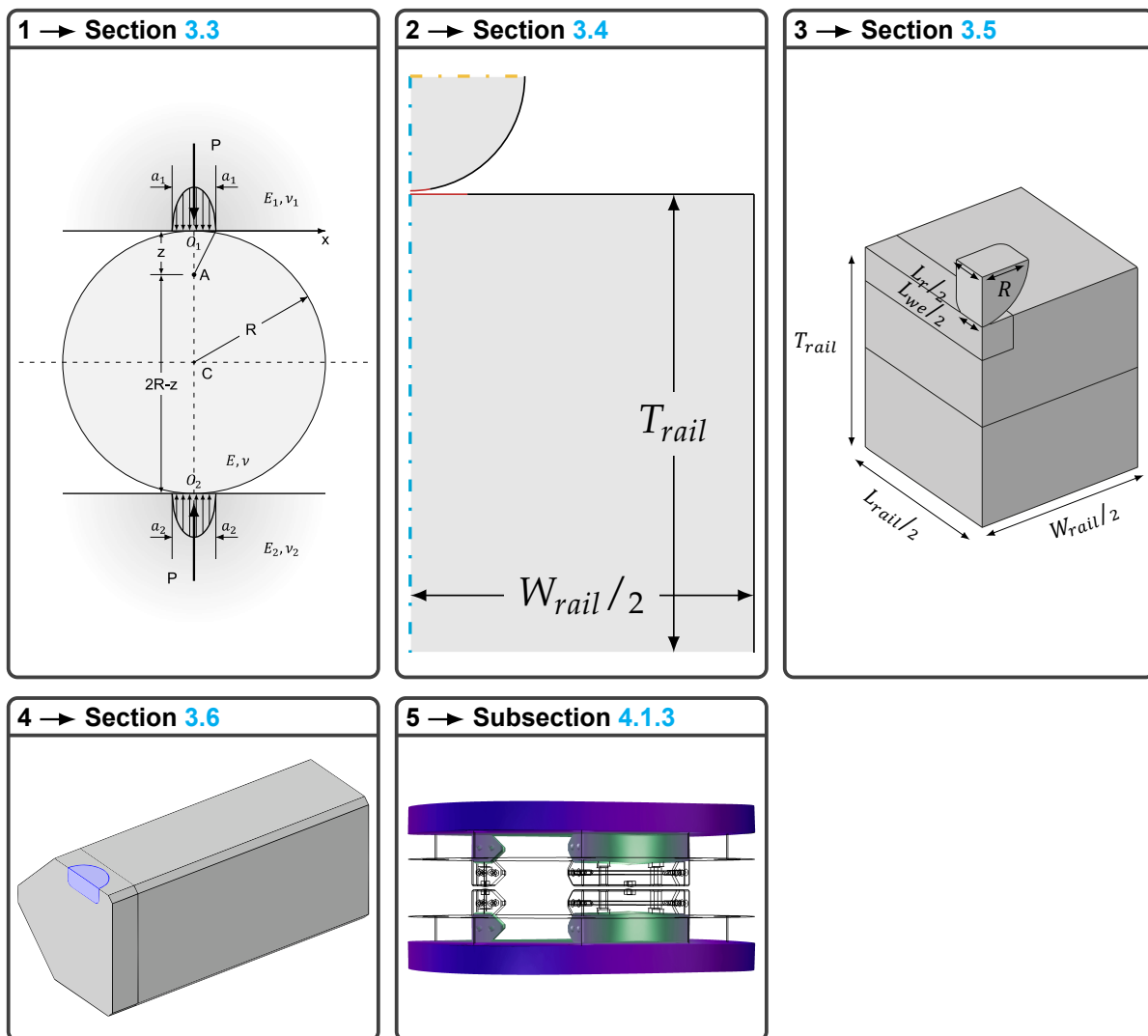


Figure 3.2: Chapter structure.

3.3. 2D analytical model

The following Section will derive Tripp's model [16]. Before doing so, it will lay down the kinematics of contact mechanics, the concept of a half-space in plane strain, and the stress and strains for distributed normal loads. Using this background, the Hertz contact theory for cylinder plane contact is derived to find the dimensions and pressure distribution of the contact region. Provided that the conditions at the contact are defined, the stresses and strains throughout the bodies can be found using Tripp's derivation.

Kinematics of contact mechanics

A frame of reference needs to be established in order to describe the kinematics of the contact. A quasi-static situation is chosen; no rolling, sliding or spin are present.

Consider the two bodies in contact as shown in Figure 3.3, the initial point of contact is taken as the origin of a Cartesian coordinate system $Oxyz$. With bodies 1 and 2 being smooth, the common tangent is the xy -plane with the x -axis to the right and the z -axis pointing down into body 2. With regards to symmetry, it is convenient to choose the x - and y -axis appropriately. So for a cylinder the y -axis is parallel with the axis of the cylinder and the x -axis is parallel with the cross section.

The undeformed shapes of bodies 1 and 2 are respectively:

$$\begin{aligned} z_1 &= f_1(x, y) \\ z_2 &= f_2(x, y) \end{aligned} \quad (3.1)$$

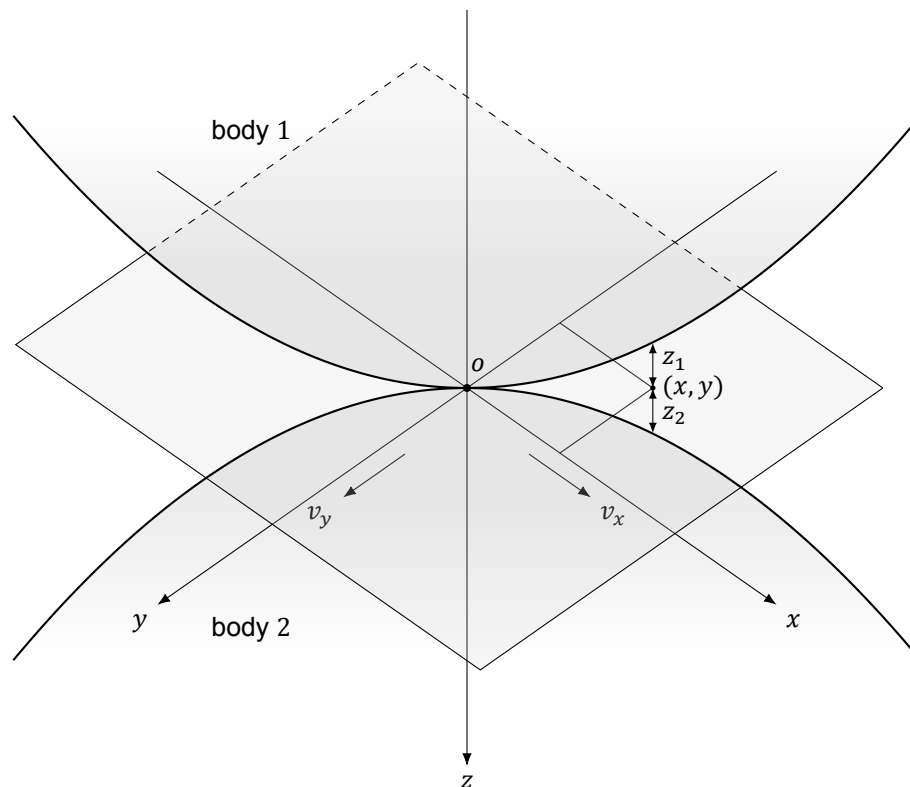


Figure 3.3: Two non-conforming surfaces in contact at O.

z_1 and z_2 represent the distance from a point on the surfaces to the xy -plane. The separation between the bodies at initial contact is given by:

$$h = z_1 + z_2 = f(x, y) \quad (3.2)$$

If the bodies are pushed together with a normal force P acting in the z -direction, a reaction force of the same magnitude of P would arise in the xy -plane. If both bodies would be rigid, the contact pressure

at O would become infinite as the contact area is zero. Real materials will deform, resulting in a finite contact region A . This contact region is defined as the region where the gap $h(x, y) = 0$, as given in Equation 3.3. The distributed normal forces between the bodies in this region are $p(x, y)$, as given in Equation 3.4, the distributed traction forces are $q(x, y)$. The integral of $p(x, y)$ over A is P . Likewise; the integral of $q(x, y)$ over A is Q , with the friction coefficient limiting the friction i.e. $Q \leq P\mu$.

The integral of these distributed loads over A can also result in a moment, in dynamic rolling problems this is the rolling friction. For static practical problems, this is small enough to be ignored [13].

$$h(x, y) = 0 \quad (x, y) \in A \quad (3.3)$$

$$p(x, y) = 0 \quad (x, y) \in \bar{A} \quad (3.4)$$

The elastic half-space

When non-conforming bodies are in contact, A will be small relative to their overall dimensions. The stresses and strains will be highly concentrated in a small region. As for calculating the stresses and strains near the contact, the rest of the geometry of the bodies are of less importance since these regions experience mostly a rigid-body motion.

In some cases the assumption of a half-space can be made, i.e. replacing the body by a semi-infinite body bounded by a plane surface. This assumption simplifies the boundary conditions and allows for the use of elasticity theory developed for the elastic half-space. This approximation does not hold up if the radii of curvature near the contact are small or in the presence of any sharp corners.

Figure 3.4 shows the cross-section of a half-space. At the surface there is a normal load $p(x)$ and a tangential load $q(x)$ in the region $-b < x < a$. No loads are applied to the rest of the surface. In the following calculation a state of plane strain ($\epsilon_y = 0$) is assumed. This assumption is justifiable if the thickness of the solid is large compared to the width of the loaded region.

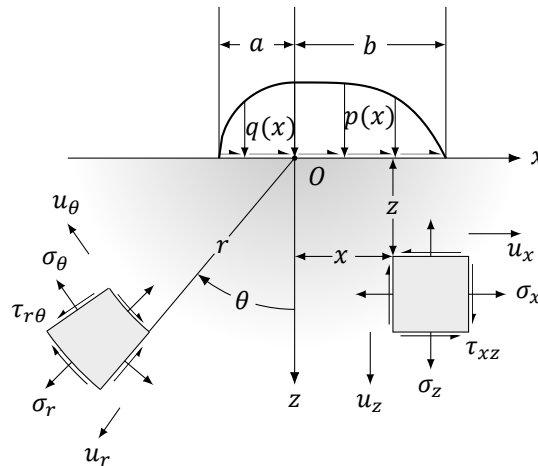


Figure 3.4: A half-space in a state of plane strain loaded by $p(x)$ and $q(x)$.

If the material properties are constant throughout the body, continuum mechanics may be applied. Furthermore the material is assumed to be homogeneous isotropic and perfectly elastic. Infinitesimal strain theory is here the mathematical tool of continuum mechanics to model the mechanical behaviour in the half-space, i.e. to calculate the deformations caused by the surface forces $p(x)$ and $q(x)$.

Using the static continuum description, only three sets of equations have to be handled. The first set ensures continuity or compatibility; it ensures that the material remains connected such that no gaps or overlaps arise. It establishes the connection between the displacements field u and local deformations i.e. strains. The second set reflects the equilibrium, as it links the stress distribution in the material with the external forces on the surface. It ensures that the body is in static equilibrium such that the material will not (locally) accelerate. Lastly, the set that describes the relationship between the deformations and stresses is the material model. The material model is also called the constitutive relations.

A detailed derivation of the elastic equilibrium equations is given by Timoshenko and Goodier [63].

For the stress distribution caused by the loads the following equilibrium has to be satisfied throughout the body:

$$\begin{aligned}\frac{\partial \sigma_x}{\partial x} + \frac{\partial \tau_{xz}}{\partial z} &= 0 \\ \frac{\partial \sigma_z}{\partial z} + \frac{\partial \tau_{xz}}{\partial x} &= 0\end{aligned}\quad (3.5)$$

For σ_y , such an equilibrium is already in place as the stresses are not a function of y .

The displacements can be obtained by integrating the strains as they are the partial derivatives i.e.:

$$\epsilon_x = \frac{\partial u_x}{\partial x}, \quad \epsilon_z = \frac{\partial u_z}{\partial z}, \quad \gamma_{xz} = \frac{\partial u_x}{\partial z} + \frac{\partial u_z}{\partial x}\quad (3.6)$$

So, for the strains following the stresses the following two-dimensional compatibility condition applies:

$$\frac{\partial^2 \epsilon_x}{\partial z^2} + \frac{\partial^2 \epsilon_z}{\partial x^2} = \frac{\partial^2 \gamma_{xz}}{\partial x \partial z}\quad (3.7)$$

The third set of equations, the material model, is Hooke's law. With the condition of plane strain and Hooke's law for a strain tensor:

$$\epsilon_y = \frac{1}{E} \{ \sigma_y - \nu(\sigma_x + \sigma_z) \} = 0\quad (3.8)$$

From Equation 3.8 it follows that:

$$\sigma_y = \nu(\sigma_x + \sigma_z)\quad (3.9)$$

Such that the other strain tensors become:

$$\begin{aligned}\epsilon_x &= \frac{1}{E} \{ (1 - \nu^2) \sigma_x - \nu(1 + \nu) \sigma_z \} \\ \epsilon_z &= \frac{1}{E} \{ (1 - \nu^2) \sigma_z - \nu(1 + \nu) \sigma_x \} \\ \gamma_{xz} &= \frac{1}{G} \tau_{xz} = \frac{2(1 + \nu)}{E} \tau_{xz}\end{aligned}\quad (3.10)$$

The stress distribution, i.e stress function $\phi(x, z)$ in the material is defined as:

$$\sigma_x = \frac{\partial^2 \phi}{\partial z^2}, \quad \sigma_z = \frac{\partial^2 \phi}{\partial x^2}, \quad \tau_{xz} = -\frac{\partial^2 \phi}{\partial x \partial z}\quad (3.11)$$

When the material model (3.10) and the equilibrium equations (3.5) are substituted into the compatibility condition (3.7), it follows that the stress function $\phi(x, z)$ satisfies the bi-harmonic equation:

$$\left\{ \frac{\partial^2}{\partial x^2} + \frac{\partial^2}{\partial z^2} \right\} \left\{ \frac{\partial^2 \phi}{\partial x^2} + \frac{\partial^2 \phi}{\partial z^2} \right\} = 0\quad (3.12)$$

The following boundary conditions need to be satisfied (over-bar denotes variables at the surface $z = 0$):

$$\begin{aligned}\bar{\sigma}_z = \bar{\tau}_{xz} &= 0, & x < -b \vee x > a \\ \bar{\sigma}_z &= p(x) \\ \bar{\tau}_{xz} &= -q(x)\end{aligned}\quad (3.13)$$

Distanced from the loaded region, $(x, z \rightarrow \infty)$, the stresses must become negligible ($\sigma_x, \sigma_z, \tau_{xz} \rightarrow 0$). \bar{u}_x and \bar{u}_z are the normal and tangential displacements respectively.

Normal line loading in the half-space To solve the stress distribution caused by a distributed load the superposition of concentrated normal loads at lines along the y -axis can be used. Firstly the case of a concentrated normal load along the y -axis is considered. The intensity of the load is P per unit length. This problem was solved by Flamant [64] (explained in [63]). It is convenient to express the stress distribution in polar coordinates:

$$\phi(r, \theta) = \frac{P}{\pi} r \theta \sin \theta \quad (3.14)$$

The bi-harmonic function can be derived in a similar fashion to that in Equation 3.12 which gives the stress components [63]:

$$\begin{aligned} \sigma_r &= \frac{1}{r} \frac{\partial^2 \phi}{\partial \theta^2} = -\frac{2P \cos \theta}{\pi r} \\ \sigma_\theta &= \frac{\partial^2 \phi}{\partial r^2} = 0 \\ \tau_{r\theta} &= \frac{\partial}{\partial r} \left(\frac{1}{r} \frac{\partial \phi}{\partial \theta} \right) = 0 \end{aligned} \quad (3.15)$$

This system of stresses is a simple radial distribution directed towards the point of application. All the boundary conditions are satisfied as at the surface ($\theta = \pm \frac{\pi}{2}$) the normal stress $\bar{\sigma}_\theta = 0$ holds (apart from origin). Far away from the point of application ($r \rightarrow \infty$) the stresses become vanishingly small. At the origin the stresses go to infinity, this is a logical consequence of the load being concentrated in a line.

Expressing the stress tensors of Equation 3.15 in Cartesian coordinates gives:

$$\begin{aligned} \sigma_x &= \sigma_r \sin^2 \theta = -\frac{2P}{\pi} \frac{x^2 z}{(x^2 + z^2)^2} \\ \sigma_z &= \sigma_r \cos^2 \theta = -\frac{2P}{\pi} \frac{z^3}{(x^2 + z^2)^2} \\ \tau_{zx} &= \sigma_r \cos \theta \sin \theta = -\frac{2P}{\pi} \frac{z^2 x}{(x^2 + z^2)^2} \end{aligned} \quad (3.16)$$

The strains given this stress distribution will be:

$$\begin{aligned} \epsilon_r &= \frac{\partial u_r}{\partial r} = -\frac{(1 - \nu^2) 2P \cos \theta}{E \pi r} \\ \epsilon_\theta &= \frac{u_r}{r} + \frac{\partial u_\theta}{r \partial \theta} = \frac{\nu(1 + \nu) 2P \cos \theta}{E \pi r} \\ \gamma_{r\theta} &= r \frac{\partial u_r}{\partial \theta} + \frac{\partial u_\theta}{\partial r} - \frac{u_\theta}{r} = 0 \end{aligned} \quad (3.17)$$

Integrating the previous first two equations gives, respectively [63]:

$$\begin{aligned} u_r &= -\frac{(1 - \nu^2) 2P}{E \pi} \cos \theta \ln r - \frac{(1 - 2\nu)(1 + \nu)}{\pi E} P \theta \sin \theta + C_1 \sin \theta + C_2 \cos \theta \\ u_\theta &= \frac{(1 - \nu^2) 2P}{E \pi} \sin \theta \ln r + \frac{\nu(1 + \nu)}{\pi E} 2P \sin \theta - \frac{(1 - 2\nu)(1 + \nu)}{\pi E} P \theta \cos \theta \\ &\quad + \frac{(1 - 2\nu)(1 + \nu)}{\pi E} P \sin \theta + C_1 \cos \theta - C_2 \sin \theta + C_3 r \end{aligned} \quad (3.18)$$

In case the material does not tilt, it only displaces in z -direction, $C_1 = C_2 = 0$. The last integration constant depends on the choice of a reference for the displacement.

Distributed normal loading When considering a load that is distributed such as is depicted in Figure 3.4 with a load $p(x)$ over the strip $-b < x < a$ the stresses and displacements can be found by superposition of the results of the line loading problem. The normal load on an elemental surface element ds can be considered a line load with magnitude $p ds$. The stresses at a location in the material due to the normal line load are given by Equation 3.16.

The displacements at the surface are:

$$\begin{aligned}\bar{u}_x(x) &= -\frac{(1-2\nu)(1+\nu)}{E} \left\{ \int_{-b}^x p(s) ds - \int_x^a p(s) ds \right\} + C_1 \\ \bar{u}_z(x) &= -\frac{2(1-\nu^2)}{\pi E} \int_{-b}^a p(s) \ln|x-s| ds + C_2\end{aligned}\quad (3.19)$$

Again C_1 and C_2 depend on the choice of a datum for calculating the displacements. The displacements can be differentiated with respect to the horizontal position x such that the integration constants are eliminated:

$$\begin{aligned}\frac{\partial \bar{u}_x}{\partial x} &= -\frac{(1-2\nu)(1+\nu)}{E} p(x) \\ \frac{\partial \bar{u}_z}{\partial x} &= -\frac{2(1-\nu^2)}{\pi E} \int_{-b}^a \frac{p(s)}{x-s} ds\end{aligned}\quad (3.20)$$

Here the gradient $\partial \bar{u}_x(x)/\partial x$ represents the tangential component of the strain at the surface and the gradient $\partial \bar{u}_z(x)/\partial x$ is the slope of the deformed surface.

Hertz Theory applied to cylinders

Assumptions in Hertz Theory When two non-conforming bodies come into contact they initially touch at a single point or line. The contact grows with increasing load into an elliptical or strip shaped contact area respectively. An elliptical contact has radii a_1 and a_2 , a strip has length l and width $2a$. A theory of contact allows for the prediction of the dimensions of this contact area, this theory is based on several assumptions and elastic theory.

Hertz Theory makes the following assumptions:

- The surfaces are smooth and non-conforming
- The shape of the bodies in the region of contact (Equation 3.1) is continuous up to the second derivative
- a is small compared with the geometry of the body
- Strains are small, thus linear theory is applicable
- No friction ($q_x = q_y = 0$)
- Each body can be considered as an elastic half-space (see requirements in Subsection 3.3)

Kinematics of the Hertz contact The second and third assumption together allow for a reasonable approximation of the surface close to the origin as a second order Taylor polynomial of the surface. For elliptical bodies, this is a function of their principal x and y radii of curvature R' and R'' respectively. The xy terms can be eliminated by aligning symmetry planes of the body with the axis of the coordinate system, for the two bodies in Figure 3.3, Equation 3.1 becomes:

$$\begin{aligned}z_1 &= \frac{1}{2R'_1} x_1^2 + \frac{1}{2R''_1} y_1^2 \\ z_2 &= \frac{1}{2R'_2} x_2^2 + \frac{1}{2R''_2} y_2^2\end{aligned}\quad (3.21)$$

In the following section, the situation shown in Figure 3.5 is considered, here body 1 and 2 are a half-space and an infinitely long roller of radius R respectively, equivalent derivations can be performed for

spheres or ellipsoids. The bodies are compressed with a load P (applied at infinity). In this situation $R'_1 = R''_1 = R''_2 = \infty$ and $R'_2 = R$.

Figure 3.5 shows the cross section near the contact between the bodies. The undeformed separation between two surface points $S_1(x, z_1)$ and $S_1(x, z_1)$ (Equation 3.2) becomes: $h = \frac{1}{2R}x^2$.

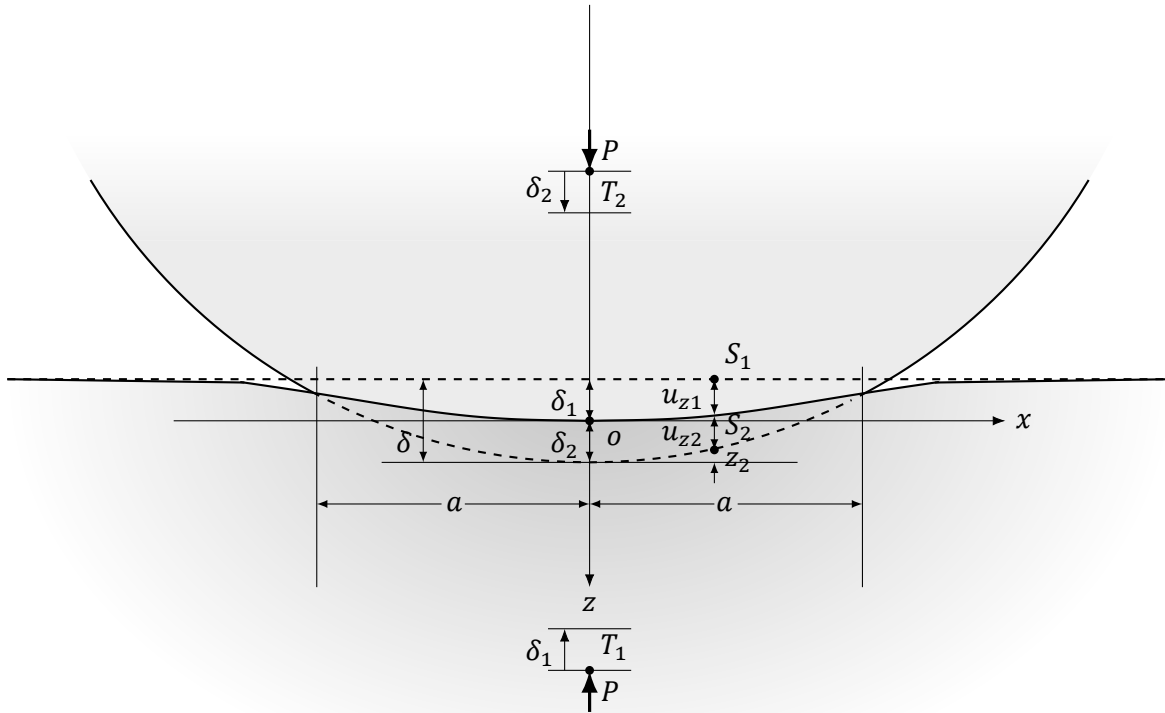


Figure 3.5: Displacements in a roller-rail contact.

As the bodies are compressed, the distant points T_1 and T_2 move in z -direction towards O by displacements δ_1 and δ_2 respectively, if the bodies do not deform they will overlap (see the dashed lines in Figure 3.5). The surface pressure compresses the surfaces points $S_1(x, z_1)$ and $S_1(x, z_1)$ in z -direction by an amount \bar{u}_{z1} and \bar{u}_{z1} relative to T_1 and T_2 respectively. If after deformation the following is true for the elastic displacements:

$$\begin{aligned} \bar{u}_{z1} + \bar{u}_{z2} &= \delta_1 + \delta_2 - h, & (x, y) \in A \\ \bar{u}_{z1} + \bar{u}_{z2} &> \delta_1 + \delta_2 - h, & (x, y) \in \bar{A} \end{aligned} \quad (3.22)$$

Solution and limitations of the Hertz problem in plane strain At this point, the problem is reduced to finding the mutual distribution of the pressure on the surfaces. This distribution should result in elastic displacements that satisfies Equation 3.22. The integral of this distribution is load P transmitted between the two surfaces.

In 2D, the elastic compression of the bodies cannot solely be derived from the Hertz stress distribution. As shown in Subsection 3.3, the displacement of a two-dimensional loaded half-space, can only be expressed relative to an arbitrary datum. Hertz Theory can still be used to find the dimensions and pressure distribution along the contact area.

Differentiating Equation 3.22 for $x \in A$ gives:

$$\frac{\partial \bar{u}_{z1}}{\partial x} + \frac{\partial \bar{u}_{z2}}{\partial x} = -\frac{x}{R}, \quad x \in A \quad (3.23)$$

Using Equation 3.20 and the notion that the contact pressures on both bodies are equal, Equation 3.23 can be written as:

$$\begin{aligned} \frac{\partial \bar{u}_{z1}}{\partial x} + \frac{\partial \bar{u}_{z2}}{\partial x} &= -\frac{2(1-\nu_1^2)}{\pi E_1} \int_{-a}^a \frac{p(s)}{x-s} ds - \frac{2(1-\nu_2^2)}{\pi E_2} \int_{-a}^a \frac{p(s)}{x-s} ds \\ &= -\frac{2}{\pi E^*} \int_{-a}^a \frac{p(s)}{x-s} ds = -\frac{x}{R} \end{aligned} \quad (3.24)$$

Where E^* denotes the effective elasticity modulus defined as [14]:

$$E^* = \frac{1-\nu_1^2}{E_1} + \frac{1-\nu_2^2}{E_2} \quad (3.25)$$

The following integral has to be solved:

$$\frac{2}{\pi E^*} \int_{-a}^a \frac{p(s)}{x-s} ds = \frac{x}{R} \quad (3.26)$$

The initially smooth continuous surface has to remain continuous, thus, the pressure distribution should fall continuously to zero at the boundary. The integral that follows has been solved by Mikhlin [65], which results in $p(s)$ of the form:

$$p(x) = -\frac{\pi E^*}{2R} \frac{x^2 - \frac{a^2}{2}}{\pi \sqrt{a^2 - x^2}} + \frac{P}{\pi \sqrt{a^2 - x^2}} \quad (3.27)$$

As the pressure has to be positive throughout the contact area (only compression) and the pressure should be finite we get:

$$P = \frac{\pi a^2 E^*}{4R} \quad (3.28)$$

Thus:

$$p(x) = -\frac{2P}{\pi a^2} \sqrt{a^2 - x^2} \quad \text{with} \quad a = \sqrt{\frac{4PR}{\pi E^*}} \quad (3.29)$$

The compression of a half-space relative to a datum d can be calculated by integrating Equation 3.19 with the pressure distribution of Equation 3.27. When evaluated at $x = 0$:

$$\delta_{half-space} = P \frac{1-\nu^2}{\pi E} \left\{ 2 \ln \left(\frac{2d}{a} \right) - \frac{\nu}{1-\nu} \right\} \quad (3.30)$$

Now the dimensions and pressure distribution along the contact area are found. Furthermore, it is possible to calculate the stresses within the bodies given this pressure distribution. However, to find the stiffness of a roller-rail contact this is less relevant.

Deflection in the roller-rail contact

The load-deflection relationship cannot be calculated solely on Hertz Theory. Here the shape and dimensions of the bodies are considered to obtain a load-deflection relationship. With the conditions at the contact defined, the stresses and strains throughout the bodies can be found using Johnson's derivation [13].

The stress distribution at a point A in the cross section of the roller between two half-spaces, as shown in Figure 3.6, is given by Timoshenko & Goodier [63]. It is a combination of the stress field due caused by load P at points O_1 and O_2 and the bi-axial tension:

$$\sigma_z = \sigma_x = \frac{P}{\pi R} \quad (3.31)$$

The bi-axial tension ensures that the section of the roller boundary not in contact, is free from stress. As O_2 is far from A it can be considered a concentrated load, such that the stressed at A are:

$$\begin{aligned} \sigma_x &= \frac{P}{\pi} \left\{ \frac{1}{R} - \frac{2(a^2 + 2z^2)}{a^2 \sqrt{a^2 + z^2}} + \frac{4z}{a^2} \right\} \\ \sigma_z &= \frac{P}{\pi} \left\{ \frac{1}{R} - \frac{2}{2R - z} + \frac{4z}{a^2} \right\} \end{aligned} \quad (3.32)$$

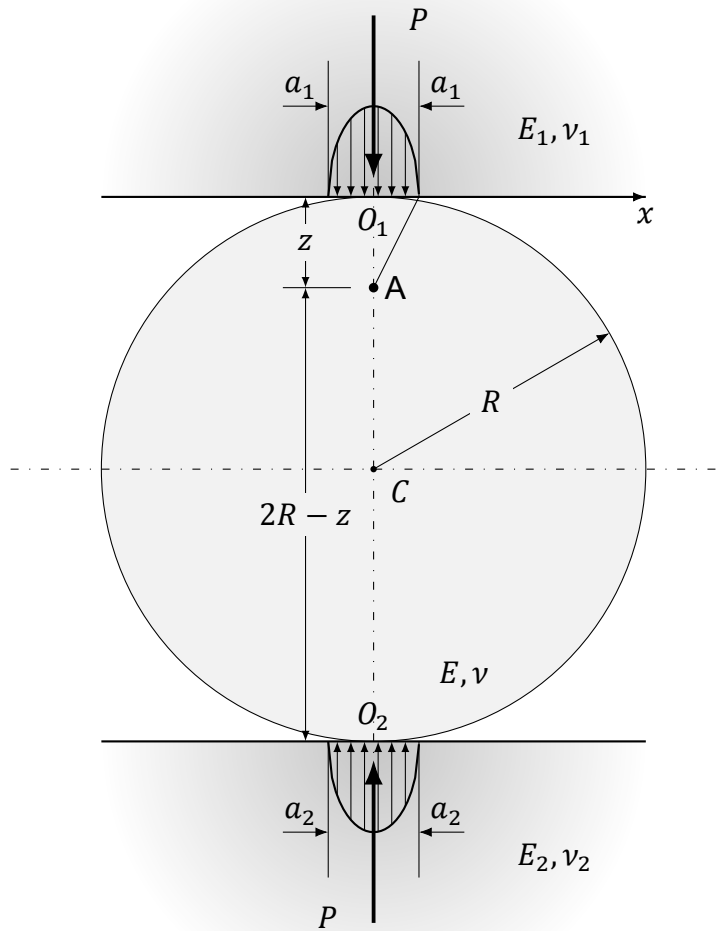


Figure 3.6: A roller between two half-spaces in a state of plane strain, compressed by load per length P .

Integrating the strain, Equation 3.9, from O_1 to C gives the compression for the upper part of the roller, compression of the lower part can be done in a similar fashion, such that the total compression of the cylinder between O_1 and O_2 becomes:

$$\delta_{roller} = 4P \frac{1 - \nu^2}{\pi E} \left\{ \ln \left(\frac{4R}{a} \right) - \frac{1}{2} \right\} \quad (3.33)$$

Now the simplification can be made that the compression of rail in a bearing assembly, taking the shape of a rectangular block of thickness t , can be calculated by modelling it as a half-space evaluated at a depth $d = t$. Such that the compression becomes:

$$\delta_{rail} = P \frac{1 - \nu^2}{\pi E} \left\{ 2 \ln \left(\frac{2t}{a} \right) - \frac{\nu}{1 - \nu} \right\} \quad (3.34)$$

As $a \ll t$, this assumption is an appropriate estimate, though arbitrary when the objective is to exactly solve the problem. The majority of the strain will take place in the vicinity of the contact; the impression scales with $\ln t$. In practical assemblies a datum of zero impression does not exist as the whole system has some compliance.

3.4. 2D finite element model

This Section introduces a 2D FEM model with the boundary conditions of a finite rail Width (W_{rail}) and thickness (T_{rail}), it challenges the half-space assumption of Tripp's model.

The basic geometry for the 2D Tripp model is presented Figure 3.6, in this figure the reflectional symmetry axes around roller center C are also depicted. These symmetries allow for modelling merely one fourth of the geometry, as is shown in Figure 3.7.

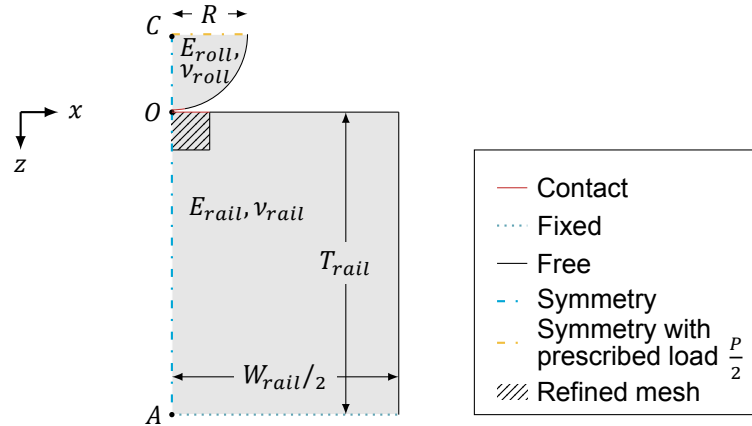


Figure 3.7: 2D finite element model: a roller of radius R compressed between rails of thickness T_{rail} and width W_{rail} .

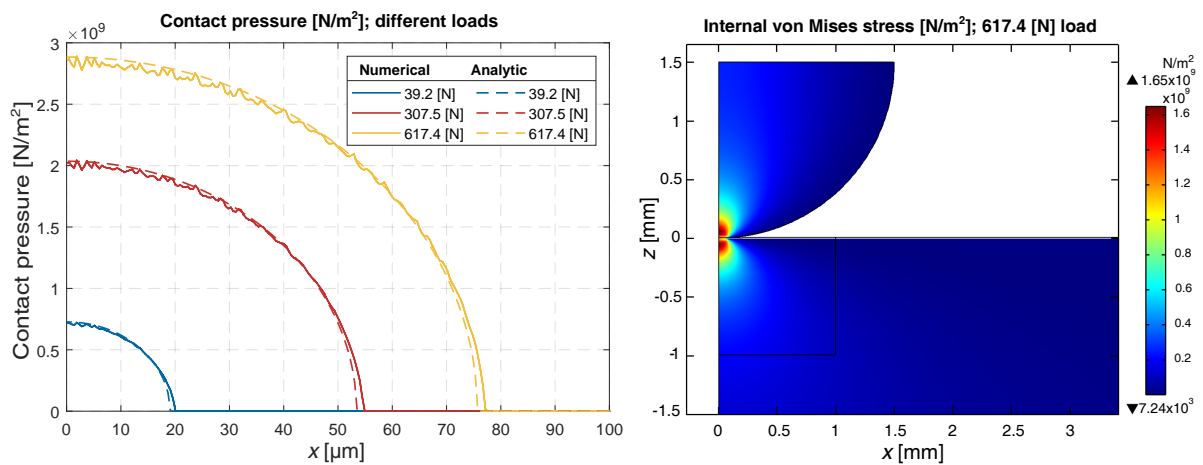
In this FEM model, the roller mesh is composed of triangular elements with a maximum size of $2.35 \mu\text{m}$ near the contact. The rail is meshed with quadrilateral elements in the hatched refinement region with a maximum element size at the contact of $1.28 \mu\text{m}$. The rest of the rail is meshed with a triangular elements. The meshes have been checked for convergence.

The analysis is performed in two consecutive steps. First the contact is initiated in a sweep in which a load is increased to the lowest tested load. Simultaneously a weak spring element is phased out to ensure a stable closing of the initial gap between the roller and rail. In a second step, the spring is removed and the load is varied. For the contact model, the penalty method is used. For validation, analysis with analytically prescribed pressure distributions were performed, this brought about identical results.

3.4.1. Contact pressure and internal stress

First the contact pressure and internal stress are examined and compared with the analytic model.

Figure 3.8a compares the contact pressure along the x -axis resulting from the FEM analysis with Equation 3.29. Figure 3.8b shows the von Mises stress in close proximity of the contact.



(a) Graph of contact pressure along x (boundary): Numerical and analytic results for roller type 1 under different loads.

(b) Graph of von Mises stress in the vicinity of the contact: roller type 1 under a load of 617.4 N.

Figure 3.8: Graphs of contact pressure and von Mises stress of 2D FEM model.

The analytic and numerical contact pressures highly correspond over the load range studied, the max discrepancy at an individual node is 3.5 %. It also demonstrates how the analytic and numerical contact widths correspond.

The maximum von Mises stress in the FEM analysis is 1646 MPa. An analytic calculation of this situation yields a peak pressure of 1631 MPa.

3.4.2. Compression of the roller

Second, the compression of the roller is presented as the compression of the roller is not dependent on an arbitrary datum. This is in contrast to the compression of a half-space.

Figure 3.9 shows the compression of the roller along the symmetry axis as a function of load for different values of W_{rail} .

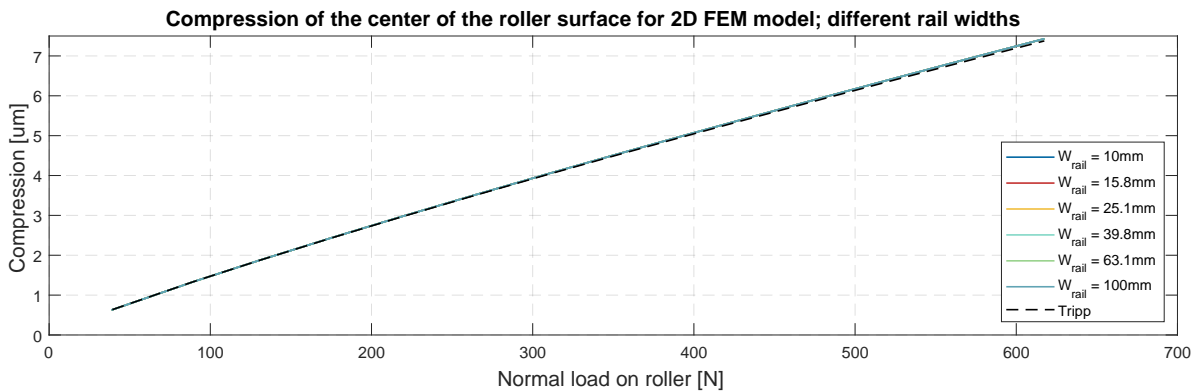


Figure 3.9: Graph of compression of the roller along the symmetry axis: 2D Numerical and analytic results for roller type 1 and rail thickness $T_{rail} = 22$ mm with variation of rail widths W_{rail} .

The found roller compression and Tripp (Equation 3.33) are equal within 1.0 % for the entire load range. Varying W_{rail} has no influence on the compression of roller.

3.4.3. Compression of the rail

Last, the influence of the finite dimensions on the compression of the rail is studied. Both the rail width and thickness are varied and compared to the Tripp model.

Rail width variation It is expected that narrow rails have a lower stiffness as the rest of the material cannot support and distribute the load and will partially act as a body in compression with stiffness EA/L .

Figure 3.10 shows the compression of the rail center (distance OA in Figure 3.7) a function of load for different values of W_{rail} .

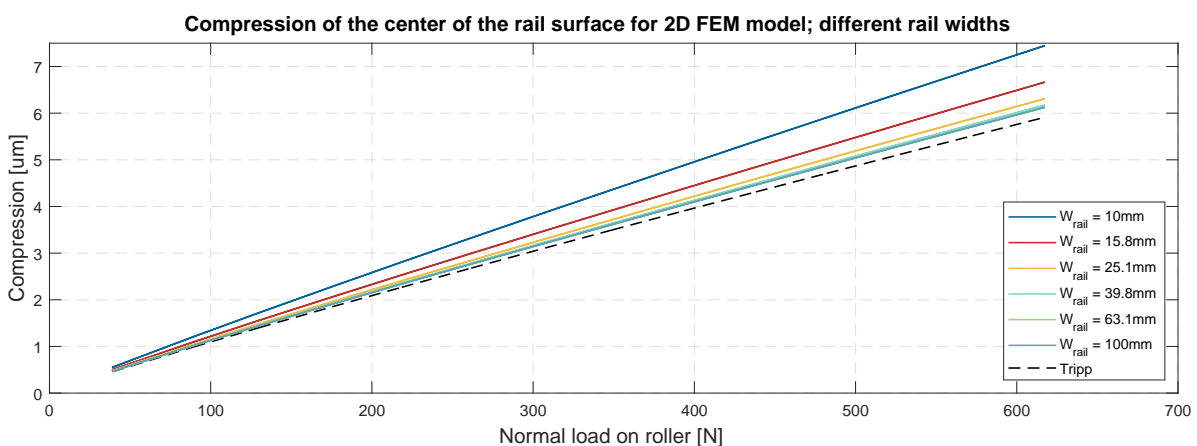


Figure 3.10: Graph of compression of the rail along the symmetry axis: 2D Numerical and analytic results for roller type 1 and rail thickness $T_{rail} = 22$ mm; variation of rail widths W_{rail} .

The rail stiffness increases as W_{rail} increases. For the widest rail geometry, the compression approaches and Tripp (Equation 3.34) by an offset of 3.3%. For $W_{rail} = 10$ mm and the highest load, the compression of the rail exceeds Tripp by 20.5%. At a width of 39.8 mm this difference is already reduced to 4.0%.

By setting the outer boundary of the rail to rigid it is verified that a further widening of the rail does not influence the stiffness. On the other hand, setting the outside boundary of the rail to rigid for small widths, results in a stiffness that exceeds Tripp.

Rail thickness variation The analytic function for compression of the half-space, Equation 3.30 cannot be used to calculate the relative strain at all depths as it evaluates to a negative values near the surface, this is physically not meaningful. The influence of rail thickness is investigated with a logarithmic sweep for T_{rail} .

Figure 3.11 presents the compression along the vertical axis (z), as illustrated in Figure 3.7, relative to the initial contact point O with a marker indicating the compression of point O relative to A .

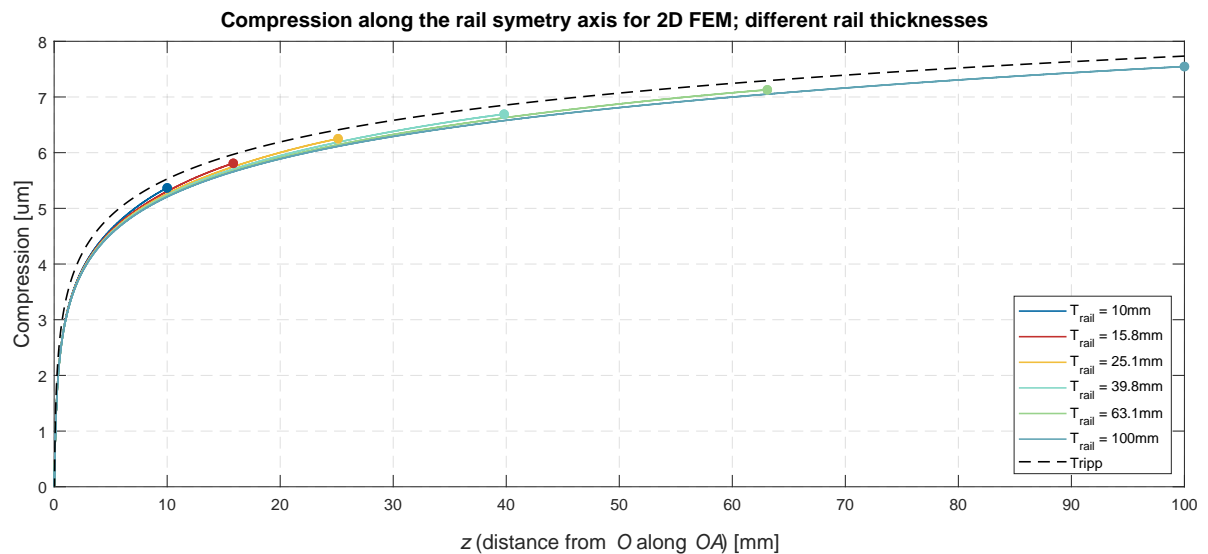


Figure 3.11: Graph of compression of the rail along the symmetry axis: 2D Numerical and analytic results for roller type 1 and load 617.4 N; variation of rail thickness T_{rail} .

The influence of rail thickness is minimal for the dimensions and loads modelled. It is important that the fraction $\frac{W_{rail}}{T_{rail}} > 1$ as otherwise the width is insufficient to distribute the load through the body.

3.4.4. Synopsis of the 2D model

These results show that the 2D finite element model is highly in line with Tripps model for the deformation of the roller, and for the rail as well, provided that W_{rail} relative to T_{rail} is sufficient. In a situation where multiple rollers are placed in an assembly, W_{rail} is shared with other rollers. An adequate model for this situation would be to set the width of the roller to roller pitch and add a symmetry plane on the free end of the rail. These experiments are performed in 4.2 using rails with $T_{rail} = 22$ mm and $W_{rail} = 100$ mm. For these dimensions, good accordance between the FEA and Tripp is found for these specific dimensions.

The next Section will investigate the validity of the plain strain assumption made in the 2D models by extending the model to 3D.

3.5. 3D finite element model

This Section introduces a 3D FEM model with the boundary conditions of a finite rail length (L_{rail}) and roller length (L_r), it challenges the plane strain assumption of Tripp's model.

Figure 3.12a shows the 3D geometry of a roller compressed between two rails, the symmetries around the roller center allow for modelling one eighth of the geometry, as shown in Figure 3.12b.

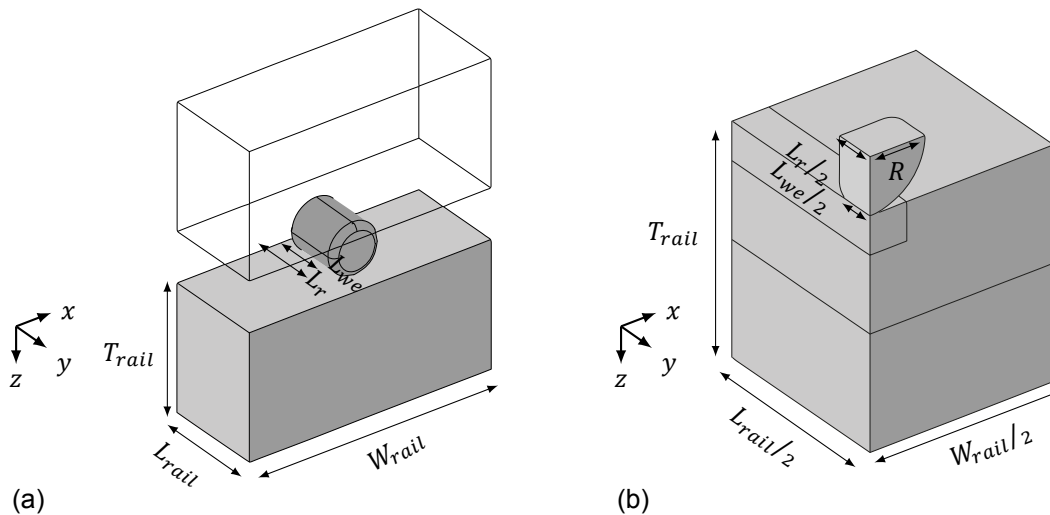


Figure 3.12: Geometry of the 3D finite element model; a roller of radius R , length L_r , compressed between rails of thickness T_{rail} and width W_{rail} . The roller and rail are in contact over the length L_{we} .

The mesh of the 3D model is built like that of the 2D model. The roller mesh consists of Tetrahedral elements with a maximum size of $3.26 \mu\text{m}$ near the contact. The rail is meshed with quadrilateral elements in the refined area (maximum element size at contact of $5 \mu\text{m}$). Outside the refinement area a mapped and swept mesh is implemented. This mesh is also checked for convergence. The Analysis is performed in two consecutive steps, similar to the 2D FEM model. Again the penalty method is used as the contact model.

3.5.1. Contact pressure and internal stress

Section 2.2.1 covered the assumption of plane strain, roller profiling and its influence on stress concentrations.

Four different roller profiles have been modelled:

1. Rounded profile with fillets of 0.2 mm, and a total roller length of 2.2 mm, as depicted in Figure 2.1d.
2. Straight profile of 1.8 mm with a symmetry plane at both ends, enforcing a state of plane strain, as assumed by Tripp.
3. Straight profile of 1.8 mm with sharp edges, as depicted in Figure 2.1a.
4. Logarithmic profile of 1.8 mm, according to Fujiwara [66], as shown in 2.1b and assumed by Lundberg [19].

Figure 3.13 shows the von Mises stress in the internal symmetry plane for these four different profiles.

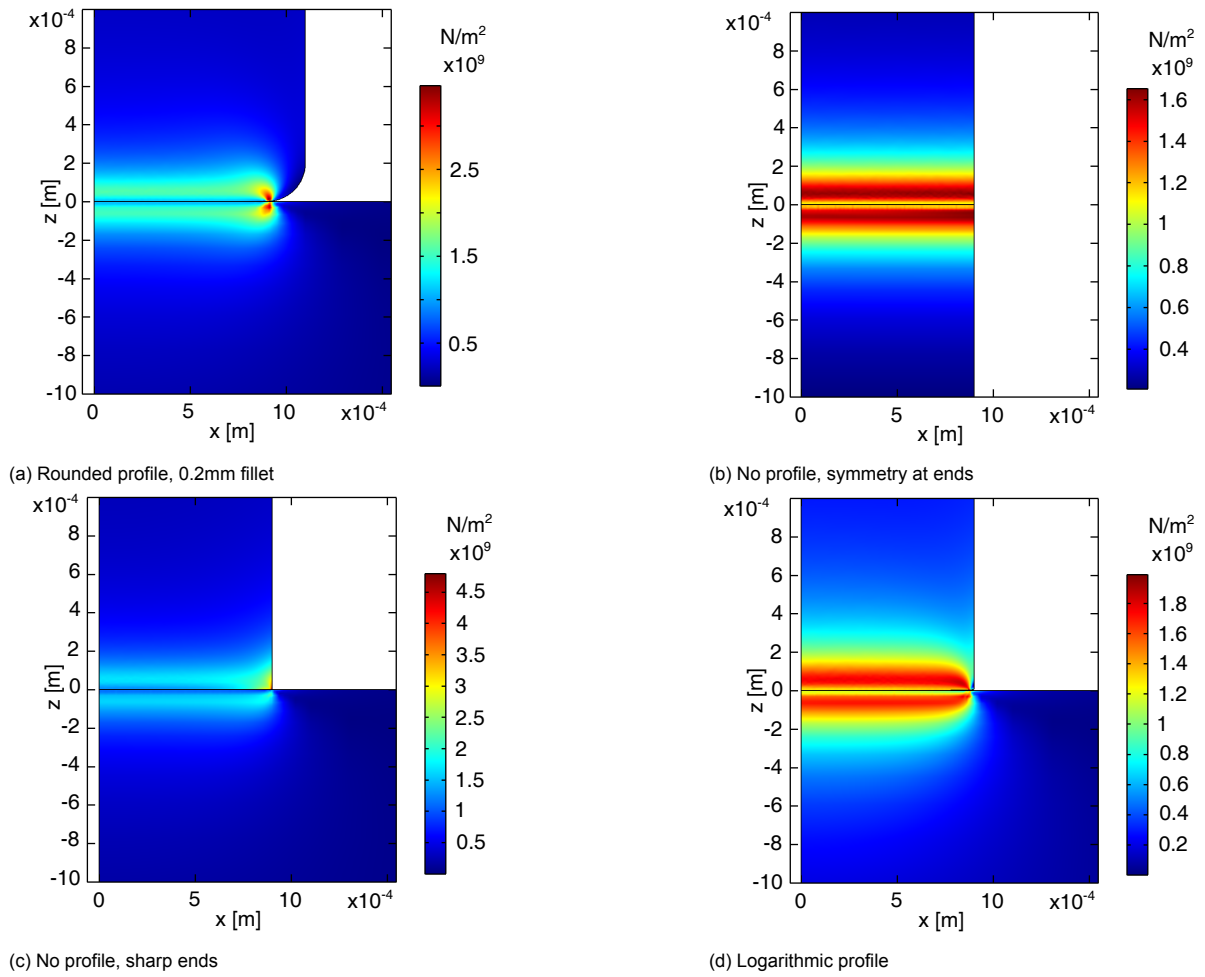


Figure 3.13: Graph of von Mises stress in the vicinity of the contact: different roller profiles subjected to a normal load of 617.4 N.

The maximum stress in Figure 3.13b is 1652 MPa, this is in line with 1631 MPa found when evaluating Equation 3.29 at $x = 0$. The pressure concentration is minimal at the end of the logarithmic roller in Figure 3.13d.

Figure 3.14 shows the contact pressure along the rail profile (y) for the four different rollers.

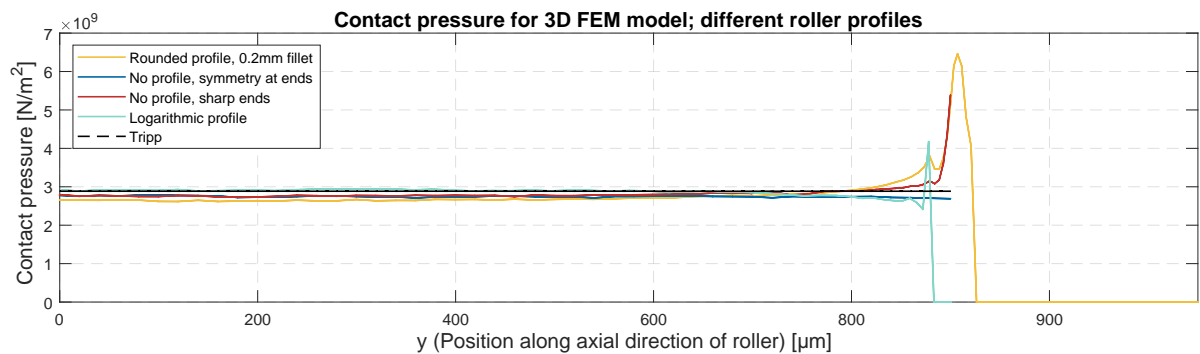


Figure 3.14: Graph of contact pressure along roller profile: different roller profiles subjected to a normal load of 617.4 N.

For the logarithmic roller, the contact pressure along the rail profile shows a small peak at higher loads, for lower loads no peak is seen. This underlines that the optimum profile depends on the loading conditions.

3.5.2. 3D compared to 2D

The 2D model can be compared to the 3D model by means of the profile with the double symmetry at the sides. When restricting the normal displacement of the symmetry plane, this boundary condition prescribes a state of plane strain. This allows for a direct comparison with the 2D model.

Figure 3.15 shows the compression of the rail center a function of load for both the 2D and 3D FEM.

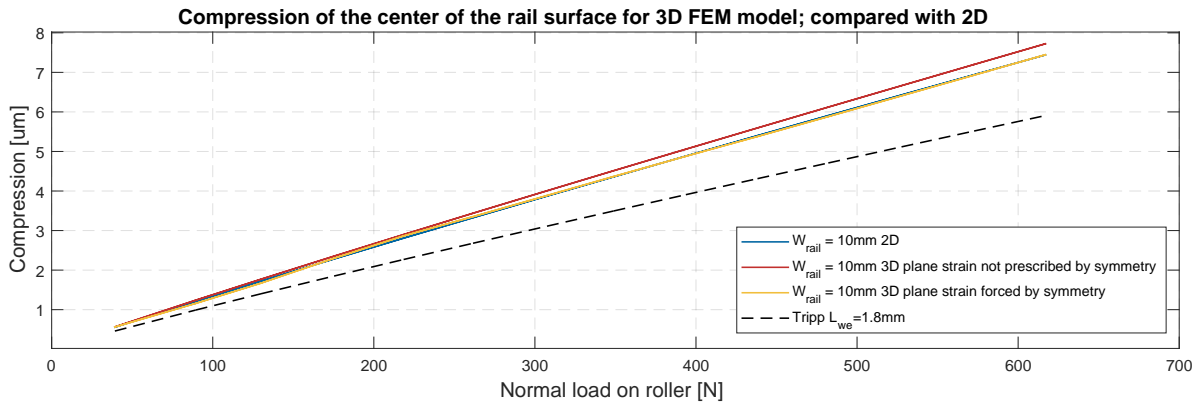


Figure 3.15: Graph of compression of the rail along the symmetry axis: Numerical and analytic results for roller type 1 and rail thickness $T_{rail} = 22$ mm; 3D compared to 2D.

The transition from 2D to 3D does not influence the results provided that the same conditions are in place; plane strain. Once this condition is loosened by allowing a translation of the symmetry plane, the rail relaxes and the compression increases by 3.7 % for the highest load. The rail width was limited to $W_{rail} = 10$ mm to limit the computational cost, for each roller profile the calculation of the 3D model took more than 5 hours, this would increase with rails of greater width, it would also take more runs to add a parametric sweep.

3.5.3. Compression of the roller

Figure 3.16 depicts shows the compression of different rollers along their symmetry axes as a function of load.

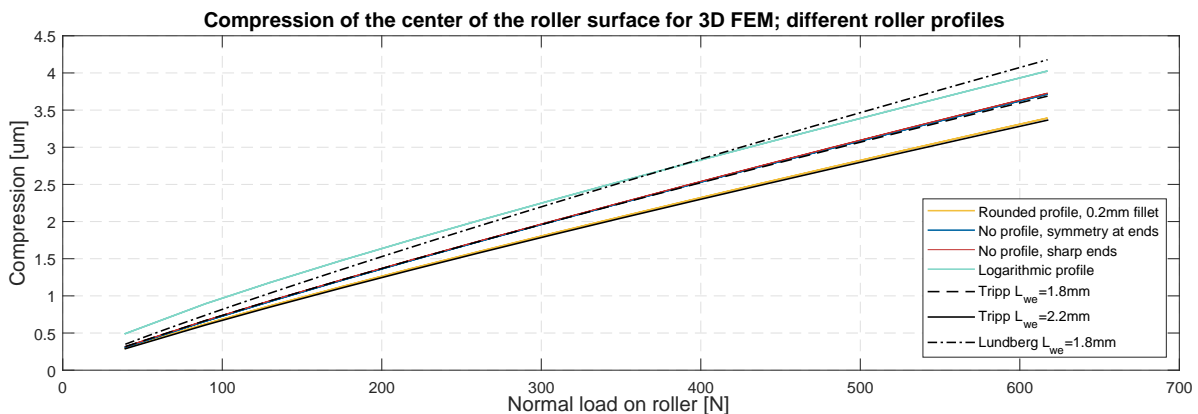


Figure 3.16: Graph of compression of the roller along the symmetry axis: 3D Numerical and analytic results for rail width and length $W_{rail} = L_{rail} = 10$ mm and rail thickness $T_{rail} = 22$ mm; variation of roller profile.

With a maximum deviation below 1.0 % for the entire load range, the Tripp accurately models the FEA compression of both the roller profiles with sharp ends and with two symmetry planes. The influence of loosening the plane strain condition and end-effects at the roller with the sharp edges appear to be insignificant, the compression difference between the two aforementioned profiles is 0.3 %. A logarithmic roller will yield a low stiffness at initial loading due to its profiling as the contact length has to grow with load. This was also seen in the model where it results in the offset observed in Figure 3.16.

This offset will not necessarily influence the roller stiffness at practical loads as the slope is in line with Equation 3.33. Remarkably, the compression of the roller with rounded edges with length $L_r = 2.2$ mm coincides with that of a roller of length 2.2 mm. Here, the fillets at the end limit the contact length to $L_{we} = 1.8$ mm. As the bulk of the compression takes place near the surface it would be expected that the compression corresponds with a length equal to the contact length.

3.5.4. Compression of the rail

Figure 3.10 shows the compression of the 3D rail as a function of load for the four different roller profiles.

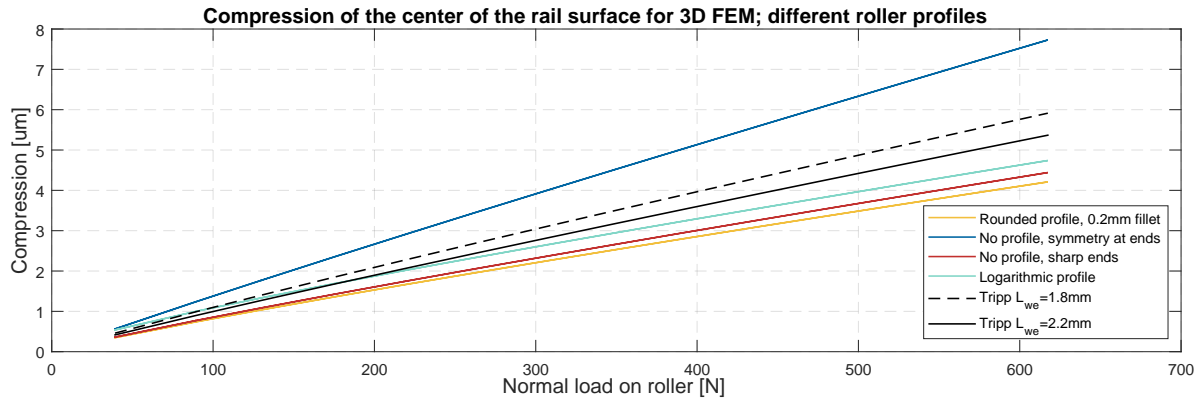


Figure 3.17: Graph of compression of the rail along the symmetry axis: 3D Numerical and analytic results for rail width $w_{rail} = 10$ mm and rail thickness $T_{rail} = 22$ mm; variation of roller profile.

The compression of the rail when loaded with a logarithmic profile shows similar characteristics as that same roller. An initial lower stiffness results in shifted load-deflection relationship, though the load-deflection relationship is nearly parallel to the rollers with a length of 1.8 mm. The filleted roller shows a slightly stiffer behaviour in comparison with the profile with sharp ends, though this difference becomes insignificant when compensating for the difference in length over which the two bodies are in contact (Figure 3.14). The most significant outcome of this 3D finite element analysis is evident when the results are compared to Tripp. The finite element model is much stiffer with a 33 % lower compression for the straight profile with sharp ends. It is important to emphasize that this behaviour was seen for a rail with $W_{rail} = L_{rail} = 10$ mm. Conversely, the 2D finite element modelling in the situation of plane strain and $W_{rail} = 10$ mm, exceeds the compression found with Tripp by 20.5 %. An explanation of this behaviour is that in the 3D model, the roller and rail do not have equal lengths, as is the case for the analytic and 2D model. As drawn in Figure 3.18, rail length which is not in contact provides support for the roller. This stiffening effect of the sides diminishes with either a small rail thickness or large roller lengths, in these situations the geometry does not allow for an ideal distribution of the load.

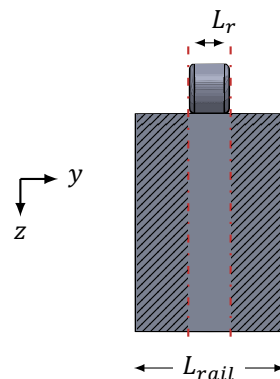


Figure 3.18: Geometry of the 3D model, hatch pattern shows the part of the rail length without loading, but which is providing support for the roller.

3.5.5. Synopsis of the 3D model

Figure 3.15 shows that the results of the 2D and 3D model are equivalent, provided that the same situation is modelled, i.e. two symmetry planes as boundary conditions prescribing plane strain. The compression of the rail depends, similar to the 2D numerical models, on w_{rail} . The stiffness of the rail decreases slightly when plane strain conditions are loosened, although this loosening is insignificant with regards to the roller stiffness. Removing the symmetry conditions from the roller and rail end introduces a discontinuity at the roller ends. This discontinuity causes stress concentrations as shown in Figure 3.13 where the von Mises stress is up to three times as high as in the rest of the profile. Different roller geometries (profiles) cause different stress distributions as shown in Figure 3.14.

Regarding the roller, the 3D FEM model and Tripp yield identical compression for different profiles, granted that L_r , and not L_{we} , is used in Tripp. The end-effects at the roller without any profiling appear to be insignificant, as presented in Figure 3.16.

Logarithmic roller profiles have a reduced stiffness which shows predominantly at the initial loading. At higher loads, the gradient of the load compression relation becomes similar to that of other profiles. This corroborates Teutsch's [21] findings that the load-deflection relation of Lundberg [19] and Kunert [20] deviate noticeably from Tripp.

In the 3D model, the rail length is not equal to the roller length as observed in Figure 3.12. The stiffness of the roller is not influenced by the rail length, comparable to how the roller stiffness is not influenced by the rail width in 2D. The additional material on both sides of the rail has a stiffening effect on the rail, resulting in almost double the stiffness than what was modelled when symmetry is in place at the roller ends, as shown in Figure 3.17.

Therefore, although the Tripp model is effective for modelling the roller compression, it is inaccurate for modelling the compression of an entire rail as the geometry depicted in 3.1a.

3.6. Compression of a full 3D rail geometry

The 2D numerical model showed the influence of the presence of material in the width (x) and thickness (z) direction, the 3D model extended its insights into the length (y) direction. In order to accurately model the compression of a rail with an identical geometry to the one used in the experiments, that exact geometry will have to be modelled. The dimensions of the rails used in experiments are given in Figure B.1. On the other hand, the compression of the roller was found to be successfully modelled using Tripp.

Incorporating contact conditions in numerical models is computationally expensive. Since the geometry of interest is solely the rail, a pressure distribution, equal to what was found in earlier models, is prescribed on a full rail geometry. This method was verified to yield equal results for a contact simulation of the rectangular rail geometry. The bottom of the rail is fixed and a symmetry plane allows to model half of the rail width. The meshed geometry is shown in Figure 3.19 with the region where the pressure is applied marked in blue. In this blue boundary a mapped mesh is defined, the mesh in the rail material is made out of tetrahedral elements.

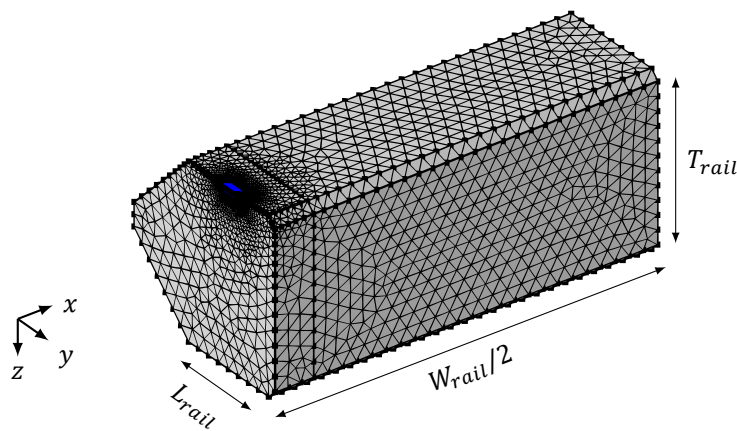


Figure 3.19: Rail Geometry of 3D finite element model; compression of a rail of thickness T_{rail} , length L_{rail} and width W_{rail} . The rail is loaded over a length of L_{we} by an applied pressure.

Even with an applied pressure, the computation of this rail is still too expensive for a multi-body dynamics analysis. The mesh is the most refined near the contact, this region has the greatest contribution to the computational cost. The compression along the thickness (z) is shown in Figure 3.20.

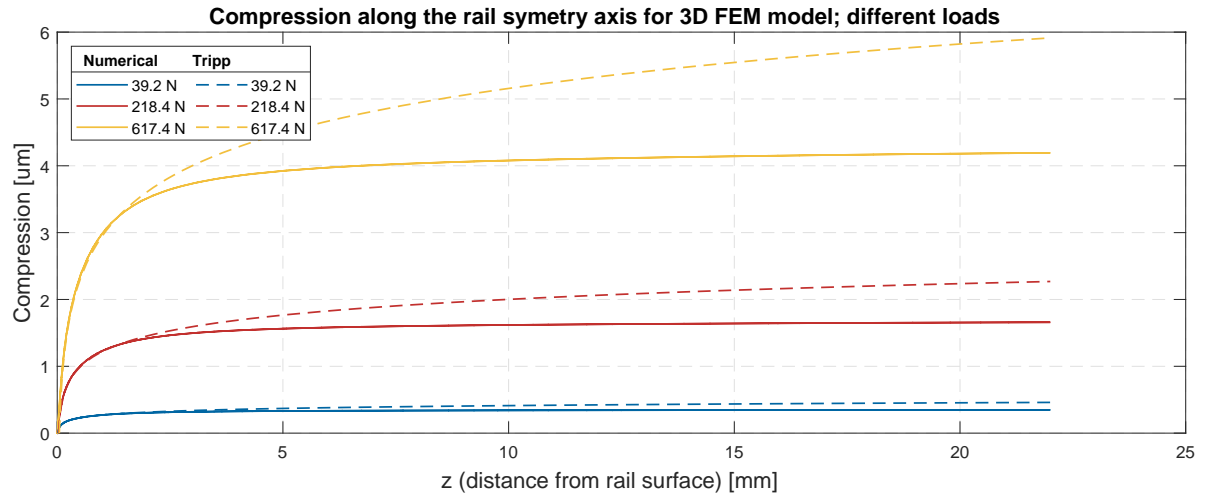


Figure 3.20: Graph of compression of the rail along the symmetry axis: 3D Numerical and analytic results for roller type 1 variation of load.

Figure 3.20 shows how in region near the contact, the numerical and Tripps model greatly agree. Here strains are dominantly prescribed by the concentrated contact. Outside of this region, the stress is more distributed and the influence of the geometry becomes significant, this is also corroborated by Figure 3.21 where an isoline is plotted at 10% of the maximum displacement. This means that 90% of the displacement in the thickness (z) direction takes place in the region enclosed by the isoline.

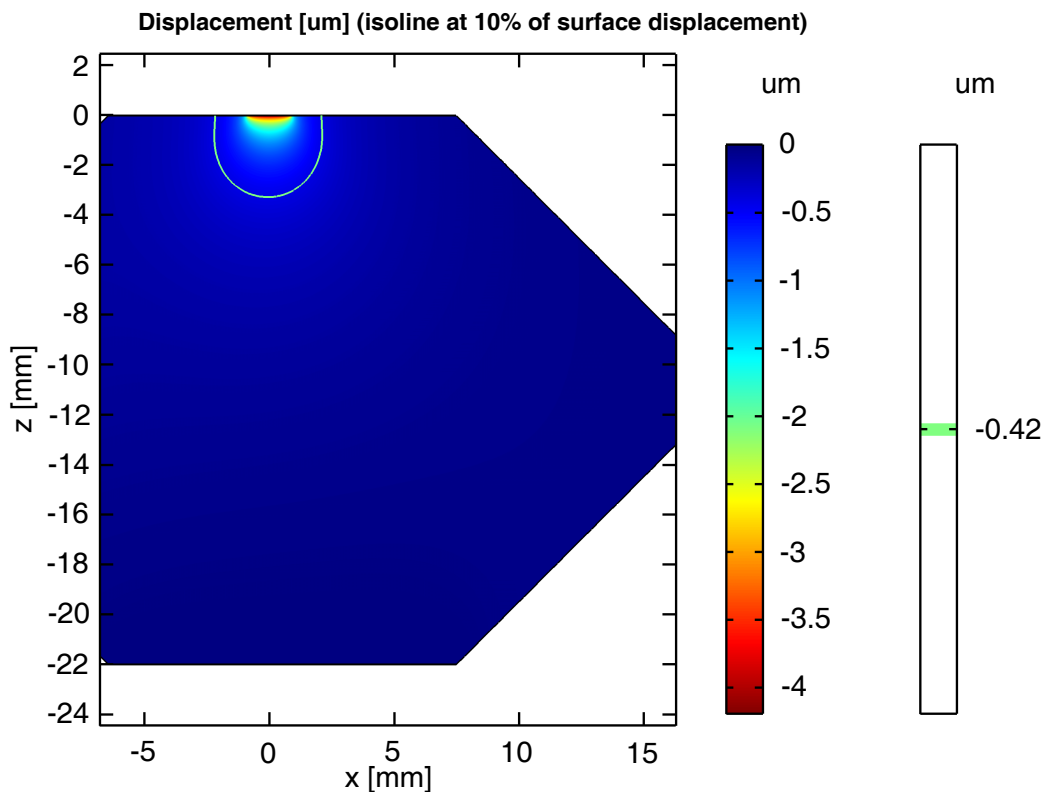


Figure 3.21: Graph of displacement in symmetry plane of 3D rail geometry: roller type 1 under a load of 617.4 N.

To efficiently and accurately model an assembly containing roller-rail contacts the following is proposed:

1. Place a simple domain in the two contact regions where the roller contacts the rest of the assembly.
2. Set the bodies to rigid and model a spring element between these two rigid bodies.
3. Set the spring element the load compression relation equal to the Tripp compression of a roller (Equation 3.33) and two rigid elements (Equation 3.34 with the thickness equal to the thickness of the rigid region).

The choice of this thickness is arbitrary. The thickness is set to 3 mm which is the depth at which 90% of the displacement has taken place for the highest considered load. At this isoline, the Mises stress reduces to less than 1% of the peak stress, the elastic strain energy density is reduced to less than 0.01% of its peak value. For this specific model a thickness of 3 mm and a radius of 4 mm gives satisfactory results for all conditions tested.

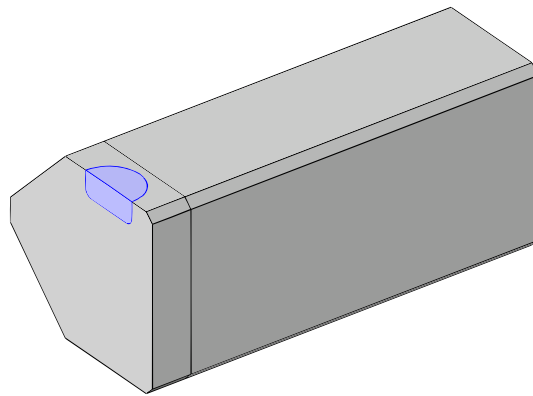


Figure 3.22: Rail geometry of 3D finite element model with a rigid inlay with a thickness of 3 mm and a diameter of 8 mm.

Figure 3.23 shows the compression of both the full numerical model and the combination of the rigid inlay with analytic compression. The geometry of the model with the rigid inlay is shown in Figure 3.22. The compression along the thickness (z) is shown in Figure 3.20.

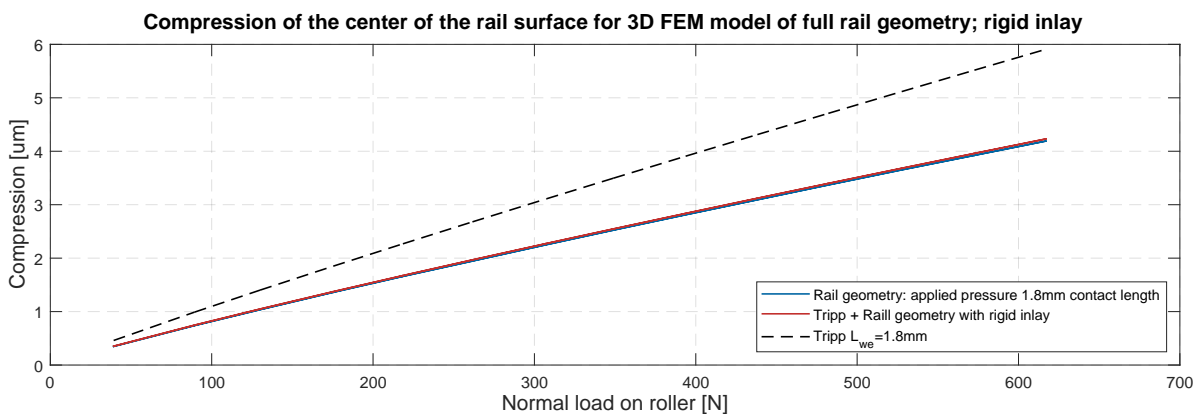


Figure 3.23: Graph of compression of the rail along the symmetry axis: 3D Numerical of full rail geometry vs combination of a rigid inlay and analytical compression.

3.7. Synopsis

Tripp [16] derived a solution for the deformation of a 2D cylinder compressed between two half-spaces, semi-infinite bodies bounded by a plane surfaces. This model is thus based on the assumption of plane-strain and a half-space. The deformation of this infinitely deep half space is calculated in relation to a chosen evaluation depth.

A 2D finite element model introduces the boundary conditions of a finite rail Width (W_{rail}) and thickness (T_{rail}) challenging the half-space assumption of Tripp's model. The 2D FEM model highly agrees with the Tripp model for the deformation of the roller. Tripp is also accurate for the rail, provided that W_{rail} relative to T_{rail} is sufficient. Narrow rails (small W_{rail}) have a stiffness lower than Tripp as the rest of the material cannot support and distribute the load and will partially act as a body in compression with stiffness EA/L . The influence of rail thickness is minimal for the dimensions and loads modelled.

A 3D finite element model introduces the boundary conditions of a finite rail length (L_{rail}) and roller length (L_r), it challenges the plane strain assumption of Tripp's model. From modelling different roller profiles it was found that roller profiling has a large effect on the contact pressure and internal stress but minimal influence on the stiffness. Regarding the roller, the 3D FEM model and Tripp yield identical compression for different profiles, granted that L_r , and not L_{we} , is used in Tripp. Logarithmic roller profiles have a reduced stiffness which is predominantly at initial loading. In the 3D model, the rail length is not equal to the roller length. The additional material on both sides of the rail has a stiffening effect on the rail, resulting in almost double the stiffness than what was modelled when symmetry is in place at the roller ends. Therefore, although the Tripp model is effective for modelling the roller compression, it is inaccurate for modelling the compression of an entire rail.

For the rail, in the region near the contact, the numerical and Tripp model greatly agree. Here strains are dominantly prescribed by the concentrated contact. However, incorporating contact conditions in numerical models is computationally expensive. To efficiently and accurately model an assembly containing roller-rail contacts, it is proposed to place a simple domain in the two contact regions where the roller contacts the rest of the assembly. Then these two domains are modelled as rigid and spring elements are placed between them. The load-compression relation of these springs is based on Tripp, the stiffness for a roller and two half-spaces with at an evaluation depth equal to the depth of the rigid bodies. The rest of rail geometry is modelled with a 3D FEA. For this specific rail and roller, the boundary of the rigid body is set at a location where roughly 90 % of the displacement has taken place. This method yields satisfactory results for all situations modelled.

4

Stiffness of a normally loaded roller between two flat rails

As outlined in the Chapter 2, relatively little experimental research has been performed on the stiffness of individual rolling elements, in particular on rollers. The published experimental results have large measurement errors and concerns rollers with a significantly larger or have very different length to diameter ratios than rollers commonly used in bearing assemblies.

The goal of the experiments performed in this chapter is to validate the method proposed in Section 3.6. All experiments in this chapter are performed on individual rollers compressed between two rails.

The influence of the following parameters is investigated:

- Load
- Product variations
- Lubrication
- Length
- Diameter
- Material
- Surface roughness
- Number of rollers

This chapter with begins Section 4.1 which describes the test setup, the experiment procedure, and the means by which the setup is validated. The results are presented and discussed in Section 4.2. Finally, the chapter concludes with Section 4.3 that synthesizes the model and experiments, it covers a methodology in which the measurement data on individual contacts can be applied in other complex geometries.

4.1. Test setup

This section elaborates on and substantiates the setup. First, it will briefly touch upon considerations when designing a setup for measuring contact stiffness. Secondly, it will lay down the workings of the setup and outline the test procedure. A list and brief description of the equipment used and its accuracy is given. All the actions taken to verify the validity of the setup and its characteristics are covered in Appendix D.

4.1.1. Considerations on a contact stiffness measurement setup

Section 1.2 described how stiffness influences system behaviour in both a static and dynamic way. These two ways in which stiffness influences a system allow analogical for two methods for measuring that same stiffness. Either statically; applying a load and measuring the displacement in the contact. Or by a study of the dynamic properties; performing a modal analysis on a system that incorporates the roller-rail contact. Traditionally a static method for stiffness measurements is chosen as it entails simpler measurement equipment. Modal analysis is the most common method for testing full high-tech systems, it allows for very accurate measurements on systems with minimal displacements. It gives information on the full frequency domain and can easily be extended to multiple directions. The literature showed how this is predominantly relevant for assemblies such as entire motion systems. There are several methods to do modal testing, hammer impact and shaker testing are the most common. Mechanical energy is supplied with known frequency content (perfect impulse for an ideal hammer impact) and the frequency response function (FRF) is studied. An example of a FRF is plotted in Figure C.2 in Appendix C.

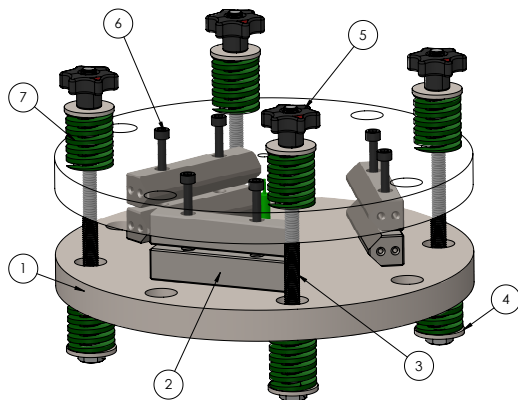
Equation 3.33 and 3.34 showed that the load-deflection relation, and therefore the stiffness is non linear. Stiffness will increase with load as the contact width of the roller-rail contact increases. An external loading mechanism needs to be in place in order to measure the stiffness for different loading conditions.

Figure 3.1b shows, the bottom of the lower rail is considered fixed. In theory this is quite easy, in practice however this is difficult and not always possible. Even a granite table, which is often considered a rigid base, will have a finite stiffness, see the half-space discussed in Subsection 3.3. The rail will have to be connected to such a base, this connection will add some compliance.

Utilization of symmetry could help here, it eliminates the need for a perfectly fixed point in the setup. The plane of symmetry could function as a place where the displacement is zero. When looking at Figure 3.1a, the center of the roller can be seen as a symmetry plane. When considering the roller-rail system as a mass spring system with the contact stiffness as the spring. With symmetry, a single mass spring system becomes a two mass spring system where the natural frequency goes from $\omega_0 = \sqrt{k/m}$ to $\omega_0 = \sqrt{2k/m}$ (with m the mass of a single moving component). It could be seen as having the center of the roller fixed and a spring of only half the length and thus double the stiffness. The mass of the rollers is insignificant compared to the mass of the rails and may be neglected in regards to the mass spring system.

When designing a setup for measuring contact stiffness it is desirable that the stiffness of the setup is higher than the stiffness of what is to be measured. The setup dynamics ought to be such that the eigenfrequencies of the setup itself are much higher than those to be measured. The eigenmodes should be distinctive and not interfere. The equipment used to capture the FRF poses limits on the frequency of the eigenmodes of interest.

4.1.2. Description of the setup



(a) CAD model of normally loaded setup



(b) Picture of normally loaded setup

Figure 4.1: The test setup used for the experiments in this section. Three pairs of rails are bolted to the two masses. The rollers are placed between the rails. The green springs exert load on the rollers and rails. The distance between the masses is measured with a capacitive probe (bright green). The frequency response is measured with accelerometers. The setup is isolated from the external world by a suspension with a tube (both not in CAD).

The setup shown in Figure 4.1 allows for two concurrent measurements, both a static measurement where a load is applied and the displacement is measured and a dynamic measurement where the FRF is determined. The setup consists of two steel disks (1) with the rails (2) between which the rollers are compressed. The dimensions of the rails used are given in Figure B.1. The load is applied by four pairs of compression springs (7) which are compressed by threaded rods (3). All components are specified in Appendix B.

Three pairs of rails and rollers are used in parallel to form a statically determinate structure, this ensures alignment of the roller-rail contacts and allows for measuring the distance between the two masses (1). The masses bring the eigenfrequency of the system down to what is desirable for the measurement equipment. The three rail pairs are bolted to the disks such that they are oriented with each 120° relative rotation around the center of the disk. This orientation results in an equal load distribution among the rollers. The point symmetry also warrants that the three other dominant modes have the same eigenfrequency. The radius at which the rollers are mounted is such that the eigenmode with normal translation of the disks is separated as far as possible from the three other eigenmodes where the two disks tilt relative to each-other. The disks are robust and ensure that the setup is an order of magnitude stiffer than the contacts measured, flex modes are isolated in the FRF. The contact faces of both the disks and rails are ground to ensure a conforming and stiff contact between the components. The setup is placed on a tube to isolate the setup from its surroundings. A mask is taped on the rails, this mask has a rectangular pocket such that the axis of the roller is parallel to the grinding direction at the rail, as this is the orientation found in bearing assemblies. The FRF is determined with Muller BBM's PAK measurements system. The static displacement between the flanges is measured with a Lion Precision capacitive displacement probe.

All setup components are standard machine elements, such that this setup can easily be reproduced. The total costs are only a few hundred euros. All machining operations consist of drilling holes in the flange for mounting the rails, and grinding the surface for smooth contact with the rails. The measurement equipment used for determining the FRF is over-specified, performing a FFT on a webcam microphone identifies the eigenfrequencies of interest.

A schematic of the setup is shown in Figure 4.2. The setup is modelled as a two mass spring system in which the mass of the roller may be neglected. Total mass is the sum of the mass of the rails, bolts and the two disks as nearly all displacement happens near the contact. The influence of the tube is insignificant, the system may be assumed to be isolated. The stiffness of the load springs are of such magnitude that they do not influence the eigenfrequency significantly. The stiffness of all the load spring pairs combined is $1.6 \cdot 10^5$ N/m, whereas for example three pairs of roller of type 1 in series have a stiffness in the order of $7.5 \cdot 10^7$ N/m in the situation where the lowest load is applied.

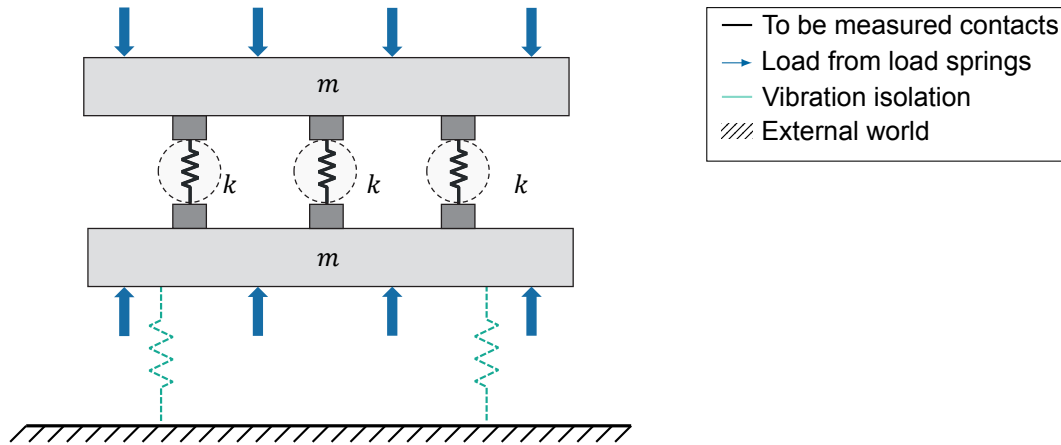


Figure 4.2: Schematic depiction of the normally loaded setup.

The stiffness k in Figure 4.2 is the sum of the elements in Figure 3.1b, i.e. Equation 4.1. This setup has three roller contacts parallel, the stiffness sum of the measured contacts is $3k$ with k :

$$\frac{1}{k} = \frac{1}{k_{rail}} + \frac{1}{k_{roller}} + \frac{1}{k_{rail}} \quad (4.1)$$

The natural frequency of this idealized two mass spring system is $\omega_0 = \sqrt{\frac{6k}{m}}$, with m the mass of one solid steel disk with attached rails and bolts.

4.1.3. Numeric multi body dynamics analysis of the setup

A rigid setup does not exist, it will always have some compliance and therefore influences the frequency response. The goal of this model is to verify if the eigenmodes are distinguishable and to determine the stiffness of the setup itself. The stiffness of this setup is calculated with a multi-body FEM model. The contacts in this FEA are modelled as proposed in section 3.6. Spring elements are placed between the created rigid inlays. The stiffness of these elements is swept over the range expected during the experiments. The multi body dynamics analysis is described in more detail in Appendix C.

The stiffness was found to be $1.45 \cdot 10^9$ N/m, and properly modelled to be in series with the three rail pairs. All the measurements discussed in this chapter are compensated for the finite setup stiffness. Yet insignificant, the stiffness of the load springs is also deducted from the measurements for completeness. Appendix C specifies how the measured FRF is linked to a roller-rail contact stiffness.

4.1.4. Test procedure

All rollers are sorted and stored in assortment boxes such that each individual roller can be uniquely identified, this allows for measurements with the same rollers in different conditions or setups. Prior to a test, the rollers and rails are cleaned with isopropanol. When the rollers are stored after a test, oil is once again applied to inhibit corrosion. Clean rollers are always handled with tweezers.

All measurements are repeated three times. Except for the precision measurements of Subsection 4.2.1 which is repeated 10 times. This entails: for each configuration the load is increased step-wise to 30 % of $C0$ three times. In-between the repetitions, the upper disk is removed from the lower disk and rollers are lifted with tweezers and placed back, this ensures a new contact every repetition. Initially the load is solely the weight of the upper half of the setup, after this initial setting the load is increased

by fastening the star knobs in steps of 180° . For each load setting within a repetition, three hammer impacts are applied. All hammer impacts are aimed at the center of the upper disk and normal to the surface. In case of an incorrect impact, e.g. a double tap, the impact data is removed and the impact is repeated.

The PAK software saves the average FRF based on three impacts. The measurement data of the captive probe is saved for the duration of the sampling window, the RMS value of the distance is determined for each impact based on the last 2.5 seconds of the sampling window. This is such that the vibration energy of the system is already dampened out.

4.1.5. Test equipment

Both the modal analysis and the static displacement measurement are logged using a PAK MKII measurement system. The vibrations are measured with four triaxial accelerometers from PCB Piezotronics, model 356A16. The modes are excited with a PCB Piezotronics impact hammer model *086D05* and *084B04* hammer tip. The distance between the two masses is measured with a Precision Lion C8 capacitive sensor. This sensor is driven by a Precision Lion CPL350 whose output is connected to the PAK MKII. A sampling window is set to 3.2 s with a sampling rate of 20 480 Hz. The PAK Measurement system is connected to a laptop running PAK software. Both the FRF as the raw time data are saved and after the experiment converted and exported to MATLAB for data analysis. The equipment used to verify the setup is covered in Appendix D. The PAK software visualizes measured eigenmodes such that the eigenshape can be compared with the FEM model.

4.2. Test results and discussion

This section presents and discusses the results of the experiments performed with the normal setup. Table A.1 lists the specifications of the rollers used. Table A.2 lists the surface roughness, roundness, and cylindricity of these rollers. All the results in this section account for, and deduct, the stiffness of the rest of the geometry. The all stiffness plotted represent the stiffness of the rolling element and two times the highlighted region of Figure 3.22.

4.2.1. Precision of the setup

The goal of this experiment is to verify the test–retest reliability of the setup.

Figure 4.3 shows the stiffness per roller as a function of the normal load on a set rollers of type 1 that are tested 10 times. The spread of the data is expressed as a percentage of the mean stiffness for a certain load level.

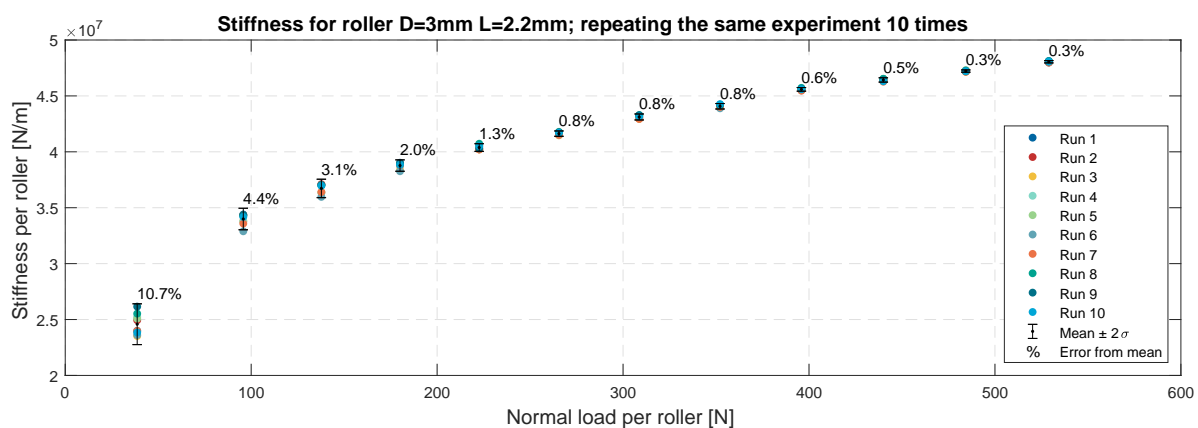


Figure 4.3: Hammer impact data: Load-stiffness relation of roller type 1 under normal conditions; 10 runs, estimating repeatability.

When a load is applied, the total spread of the measured stiffness is less than 5% and at higher loads this spread decreases to 1% ($\sigma = 5 \cdot 10^4$ N/m). This increase of accuracy is probably caused by a decrease in the error arising from setting the load knobs by hand ($\pm 10^\circ$), which decreases relatively with the total load. Furthermore, as given by the load-deflection relationships from Section 3.3, the sensitivity of the stiffness to load variations is higher at light loads. This explains the high spread of a just under 11% ($\sigma = 10^6$ N/m) when only the weight is present as load.

The roller-rail contact stiffness is also calculated by means of taking the derivative of the absolute distance measured with the capacitive probe. The results obtained with the capacitive probe are given in Appendix E. The precision of this method is lower, the mean load-stiffness relation of both methods highly agree. A regression on the static stiffness measurements shows that all single hammer impact measurements lie in the 95 % confidence interval. A lower accuracy for stiffness calculated through the capacitive probe is expected as a consequence of the error propagation. Subsequent results will only consider the hammer impact data.

The high sampling rate of the capacitive measurement allow studying the frequency spectrum of the time data. The found peak frequencies match the eigenfrequencies obtained with accelerometers.

4.2.2. Accuracy of the setup

The goal of this experiment is to verify the accuracy of the setup. Experiments should be performed with elements for which the stiffness is known. From Section 2.2.1 it is evident that the stiffness of a roller-rail contact is arbitrary. However, for a ball-rail contact there is general consensus, under small strains, Hertz Theory is unambiguous and accurate for dry and smooth contacts [13].

Figure 4.4 shows the stiffness per ball as a function of the normal load for bearing steel balls with a diameter of 3, 6, and 9 mm, rolling element 10, 11, and 12 in Table A.1.

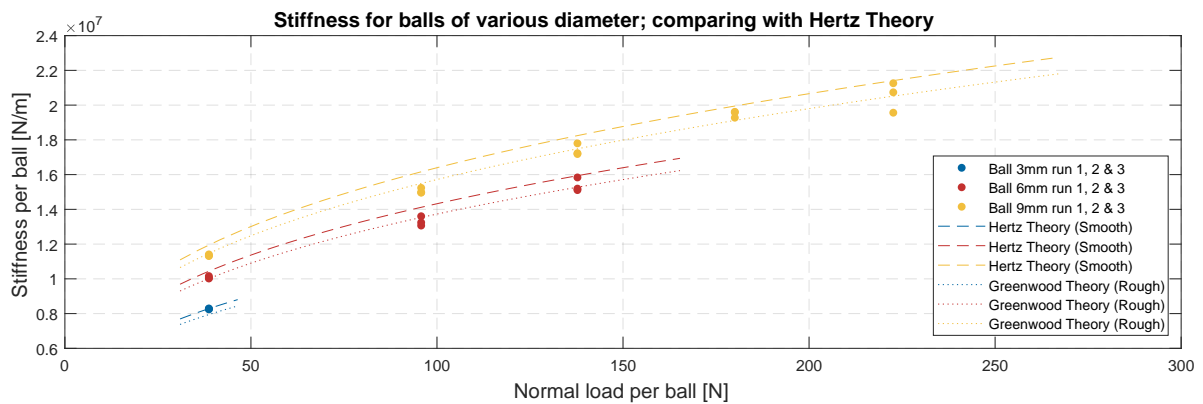


Figure 4.4: Hammer impact data: Load-stiffness relation of balls of 3, 6 and 9mm under normal conditions; 3 runs, estimating setup accuracy.

The measured stiffness is close to the stiffness expected from theory, the difference between the rough and smooth contact model is more significant than the discrepancy between the rough model and rough measurements. Following from this experiment, and the uncertainty and error analysis measurements in Appendix D it can be assumed that the measurements are accurate.

4.2.3. Product variations of rollers

All rollers are manufactured according to predefined tolerances, dimensions range within these tolerances. Surface typologies and grain structures are unique and vary from roller to roller. As a consequence, every roller will have an unique mechanic behaviour. Studying the spread in load-stiffness relationships for the same roller type gives an upper limit for the accuracy of meaningful roller modelling.

Figure 4.5 shows the stiffness per roller as a function of the normal load for three different sets of type 1 rollers.

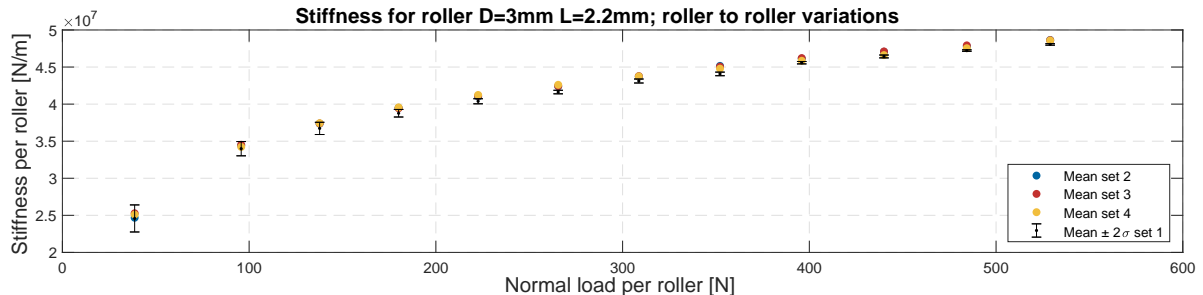


Figure 4.5: Hammer impact data: Load-stiffness relation of roller type 1 under normal conditions; Mean values roller to roller variation.

The measured roller set to roller set variation is greater than the variation among repetitions of the same set. The mean data presented for roller set 1 is the mean of the data shown in Figure 4.3. For the highest load, the difference in stiffness between the sets is small, 1 %. A One-way ANCOVA is conducted to determine whether there is a statistically significant difference between the roller to roller variations on the stiffness while controlling for the load. This analysis is reported in Appendix F. From the analysis, it is evident that there is a significant effect of roller set to roller set variation on the measured stiffness after controlling for load, $F(3, 199) = 4.941$, $p = 0.002$. Since there is already a significant difference measured between rollers of the same type, performing statistical tests on the mean of different roller types will yield uninterruptible results as roller to roller variation is highly significant already. Even if the difference in their type would not cause a significant effect, the fact that they are not the same rollers will likely already result in a significant result.

4.2.4. Influence of lubrication

The presence of lubrication might influence the damping in the roller-rail contacts. Experiments are performed using both grease and oil, *Lubcon Thermoplex ALN 1001/00* [67] and *Klüber Summit SH 32* [68] respectively. It is important to point out that these experiments are performed under non-rolling conditions so no EHL layer can be formed.

Figure 4.6 shows the stiffness per roller as a function of the normal load for rollers of various lubrication conditions.

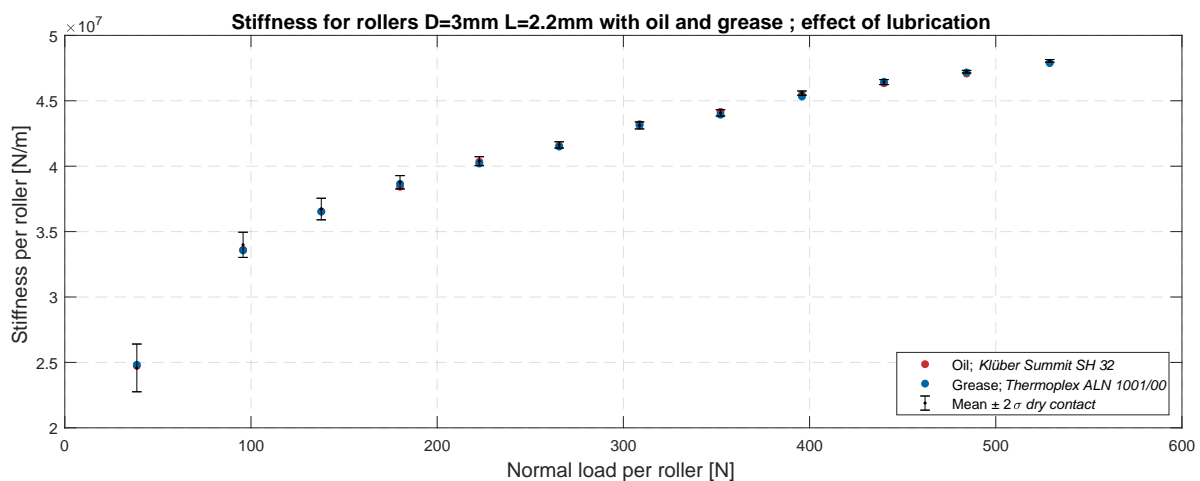


Figure 4.6: Hammer impact data: Load-stiffness relation for roller type 1 under normal conditions; Mean values for rollers with different lubrication conditions.

Figure 4.6 shows that applying oil or grease to the roller-rail contact does not significantly influence the stiffness, One-way ANCOVA $F(2, 188) = 1.182$, $p = 0.309$. This analysis is reported in Appendix F. The mean Q factor for the dry contacts from experiments of Subsection 4.2.1, is 47. The average damping coefficient for grease and oil are 43 and 48 respectively. The standard deviation of the Q factors are such that these differences are not significant.

4.2.5. Variation of contact length

Section 2.2.1 discussed the influence of roller profiling and end-effects. Experiment are performed using rollers type 1, 5, 6, and 7 with length $L_r = 2.2, 2, 2.8,$ and 4mm , and contact length $L_{we} = 1.793, 1.947, 2.569,$ and 3.734mm respectively.

Figure 4.7 shows the stiffness per contact length (L_{we}) as a function of the normal load for rollers of various contact length.

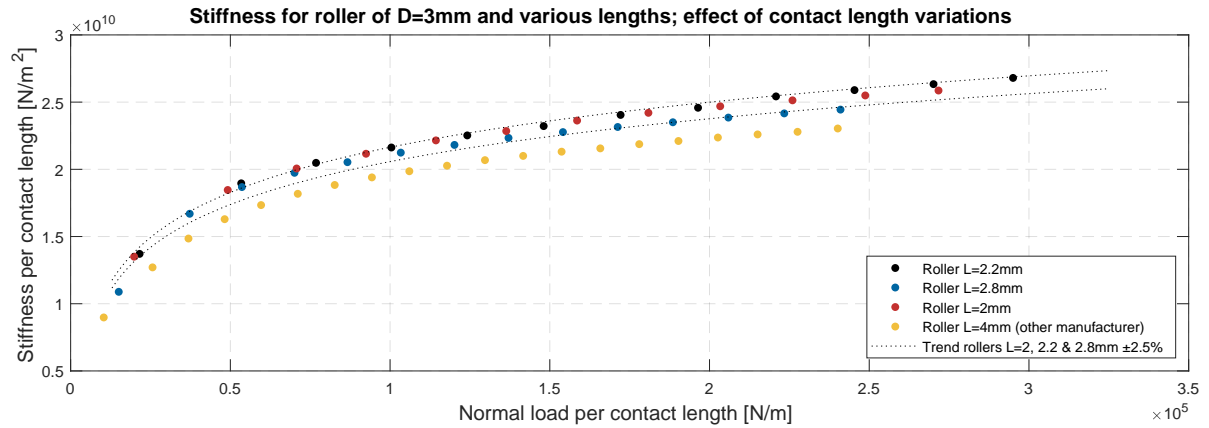


Figure 4.7: Hammer impact data: Load-stiffness relation for roller types 1, 5, 6, and 7 under normal conditions; Mean values for rollers of various contact length.

A trend is noticeable, the stiffness per contact length decreases with contact length. A logarithmic curve fit of roller types 1, 5, and 6 has been fitted with a $\pm 2.5\%$ offset to illustrate the spread among the different roller lengths. Interestingly, the results demonstrated a substantial lower stiffness per contact length for the roller of type 6. This roller is produced by a different manufacturer as the other rollers. When inspecting this roller with an optical comparator (i.e. a profile projector as done in Appendix D), it is evident that this roller has more surface defects compared to the other rollers. Table A.2 quantifies the contrast in roller quality. These results suggest it is important include roller quality when modelling roller-rail contacts.

4.2.6. Variation of roller diameter

There no consensus as to whether there is an effect of roller diameter on load-stiffness relationship. For some relationships, such as the Tripp model, the influence of the roller diameter cancels out when the rail and roller have identical mechanic material properties. The relative influence of surface defects is expected depend on roller diameter. To investigate the role of roller diameter on the stiffness, experiments are performed using rollers with diameters of 1.50, 3, 6 & 9 mm. Due to availability, the contact length is not held constant during this experiment.

Figure 4.8 shows the stiffness per contact length (L_{we}) as a function of the normal load for rollers of various diameter.

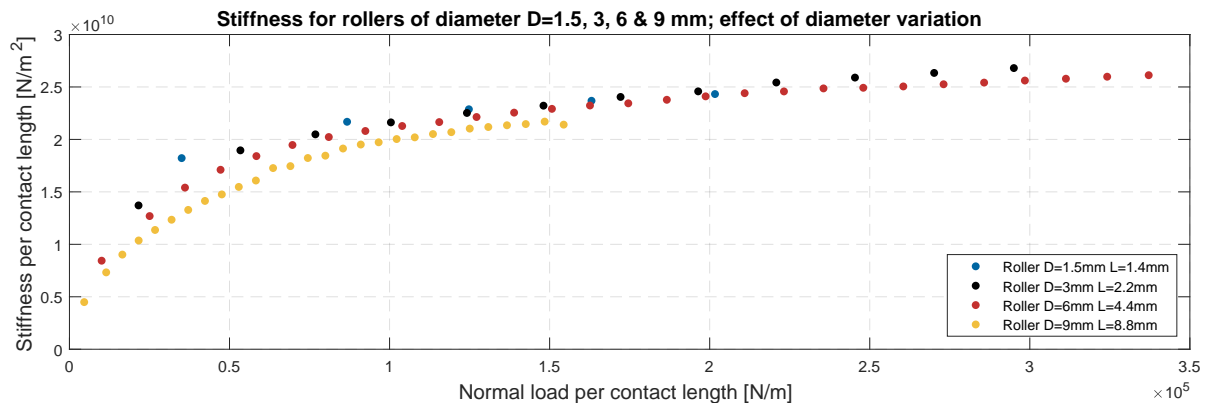


Figure 4.8: Hammer impact data: Load-stiffness relation for roller types 1, 2, 3, and 4 under normal conditions; Mean values for rollers for the various diameters.

A decreasing in the stiffness per contact length is seen when comparing the different diameters. However, no conclusions can be drawn as in the rollers measured, as the diameter is coupled with contact length. The static load rating C_0 scales linear with roller diameter so for larger diameters measurements could be performed with greater loads, yet the springs limited the maximum applied per contact length for the $D = 9$ mm rollers. Measurements on the $D = 9$ mm rollers are difficult as the FRF and showed multiple peaks, as can be seen in Figure C.3. This data is not as clean as measurements with the other rollers as depicted in Figure C.2.

4.2.7. Variation of the number of rollers

Experiments with an increased number of rollers allow for the investigation of the influence of misalignment and parallelism and the tolerance on roller diameter. Therefore experiments are performed with 3, 6, and 9 rollers in the setup. The rollers used are of type 1. Individual MBD FEA are performed for the different number of rollers. The stiffness values for the setups with 3, 6, and 9 rollers are $1.45 \cdot 10^9$ N/m, $2.25 \cdot 10^9$ N/m and $2.05 \cdot 10^9$ N/m respectively.

Figure 4.9 shows the stiffness per roller as a function of load applied for 3, 6, and 6 type 1 rollers.

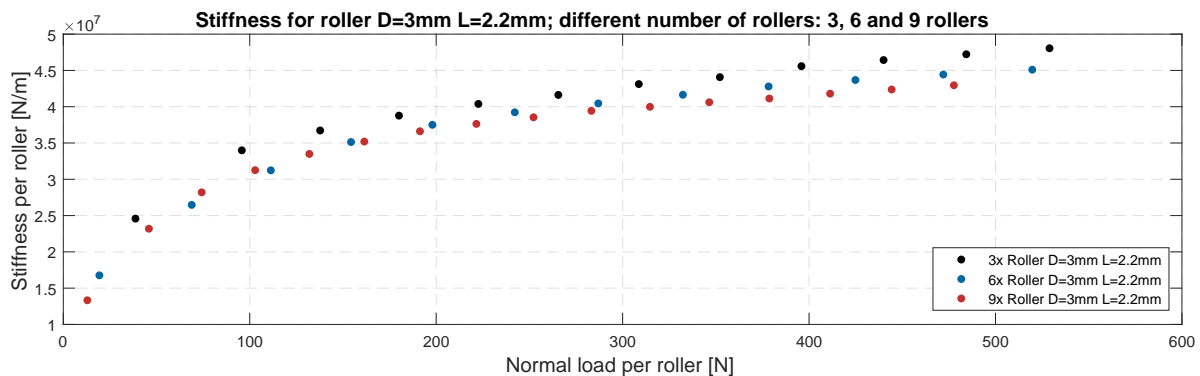


Figure 4.9: Hammer impact data: Load-stiffness relation for roller type 1; Mean values for different number of rollers.

The effective stiffness per roller decreases with the number of rollers. The stiffness for a load of around 475 N is $4.72 \cdot 10^7$ N/m, $4.44 \cdot 10^7$ N/m and $4.30 \cdot 10^7$ N/m for 3, 6, and 9 rollers respectively.

4.2.8. Influence of roller material

Existing empiric load-stiffness relations are based on rollers made out of bearing steel. Bearing steel is the most common material for rolling elements, however, in some situations ceramic and stainless steel are used. Both stainless steel (1.4034), roller type 9, and ceramic (Si_3N_4), roller type 8, are tested. Not only the roller material varied, also the contact length varies slightly due to differences in roller profiling. To account for this, the stiffness and loads are plotted per contact length. Figure 4.10 shows the measured load-stiffness relation of ceramic (Si_3N_4), and bearing steel rollers, type 8 and 5 respectively.

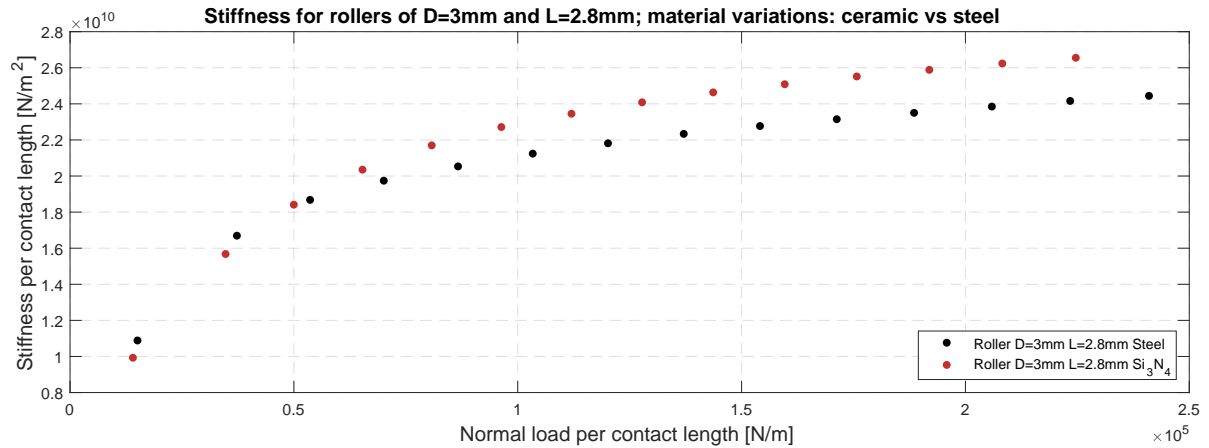


Figure 4.10: Hammer impact data: Load-stiffness relation of rollers of different materials under normal conditions; Mean values for Ceramic and steel rollers.

Figure 4.10 shows that ceramic roller is stiffer than a steel roller of the same length, this is expected as deformation is a function of the effective elasticity modulus defined in Equation 3.25. Quantifying the expected difference between the two materials is difficult as no accurate data is available on the material properties of the ceramic roller.

Figure 4.11 shows the measured load-stiffness relation of stainless and steel rollers, type 9 and 1 respectively.

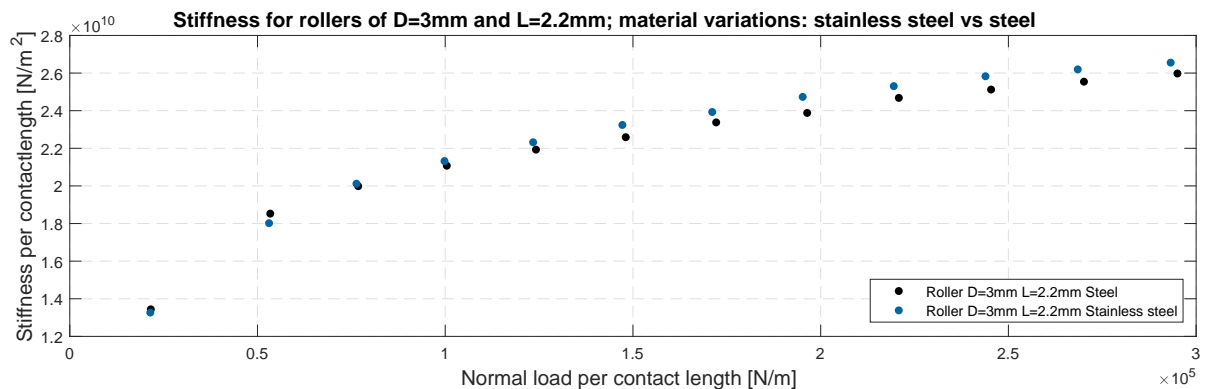


Figure 4.11: Hammer impact data: Load-stiffness relation of rollers of different materials under normal conditions; Mean values for stainless and steel rollers.

Figure 4.11 shows that the stainless steel roller is considerably stiffer than a bearing steel roller of the same length. This is surprising as the Young's modulus of the stainless steel used is 200 GPa, this is lower than the 210 GPa for bearing steel. The roller profiling and contact length are identical for the two roller types. The variance of the stainless steel measurement was similar to that of other measurements. One possible explanation is the difference in hardness. The lower hardness of the stainless steel roller allows it to deform plastically and conform to the roughness profile of the rail, and thus increase the effective contact area. The difference between the two roller materials is further assessed in Subsection 4.2.9 where the influence of different surface finishes is studied.

4.2.9. Influence of the rail surface finish

Section 2.3 covered the influence of surface roughness on the contact stiffness. While prior research thoroughly investigated the theoretical influence, especially for spheres, experimental validation for rollers is limited large rough-turned rollers [39] or train wheels [41]. Experiments are performed with mirror finish treated rails with a surface roughness of $R_a=0.03 \mu\text{m}$, while initially the rails had a ground surface with a roughness of $R_a=0.2 \mu\text{m}$.

Balls Firstly, steel balls are measured as there exists a widely accepted model for modelling the influence of surface roughness on balls [69]. The influence of surface roughness scales with $(\frac{R}{p^2})^{\frac{1}{3}}$.

Figure 4.12 shows the results both for the original rails as the mirror finished rails for balls of diameter 3, 6, and 9mm. Both the Hertz model for smooth contacts and the Greenwood stiffness are plotted as this allows for incorporating the influence of the surface roughness.

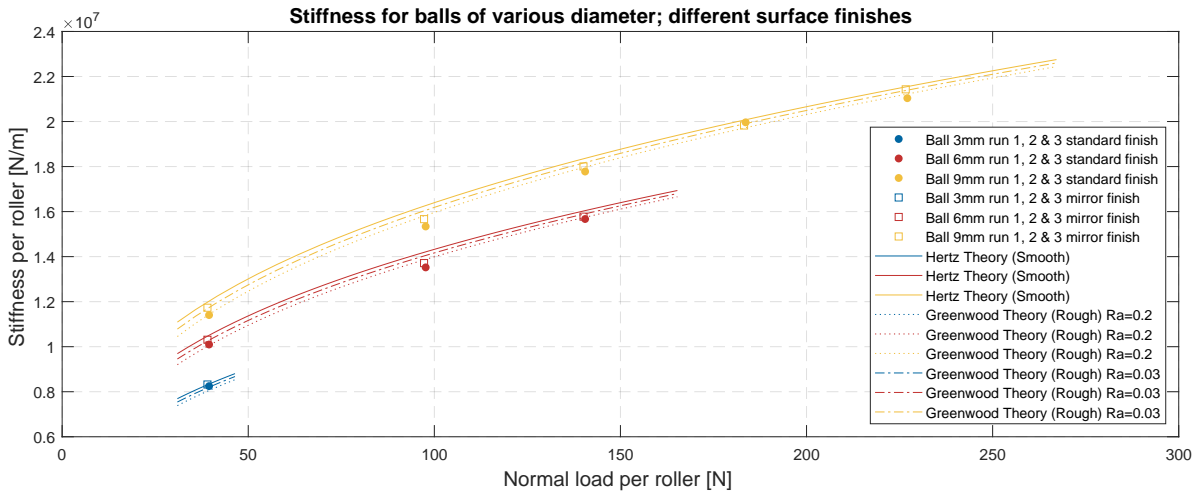


Figure 4.12: Hammer impact data: Load-stiffness relation of balls of 3, 6, and 9mm under normal conditions; Mean values for different surface finishes.

The magnitude of the influence of the surface finish change on the stiffness is in line with what is expected from the theory presented by Greenwood et al. [69].

Rollers Figure 4.13 shows that similar effect is measured for rollers, the stiffness increases with a smoother surface.

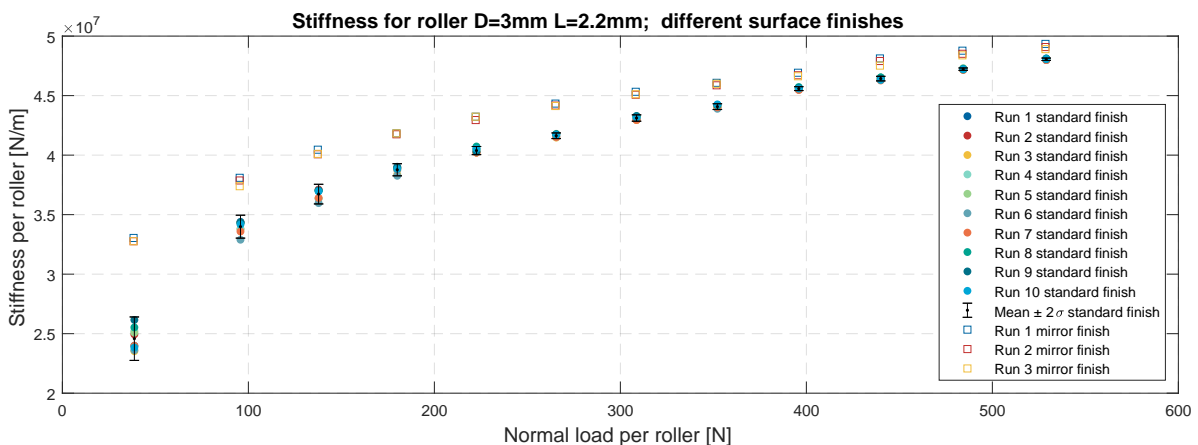


Figure 4.13: Hammer impact data: Load-stiffness relation of roller type 1 under normal conditions; different surface finishes.

The initial variance of the measurements is lower, in this region the influence of surface topology prevails. The smaller the contact area is, the larger the influence of individual roughness peaks.

Roller length Figure 4.14 shows the influence of the surface finish on the load-stiffness relation for different roller lengths.

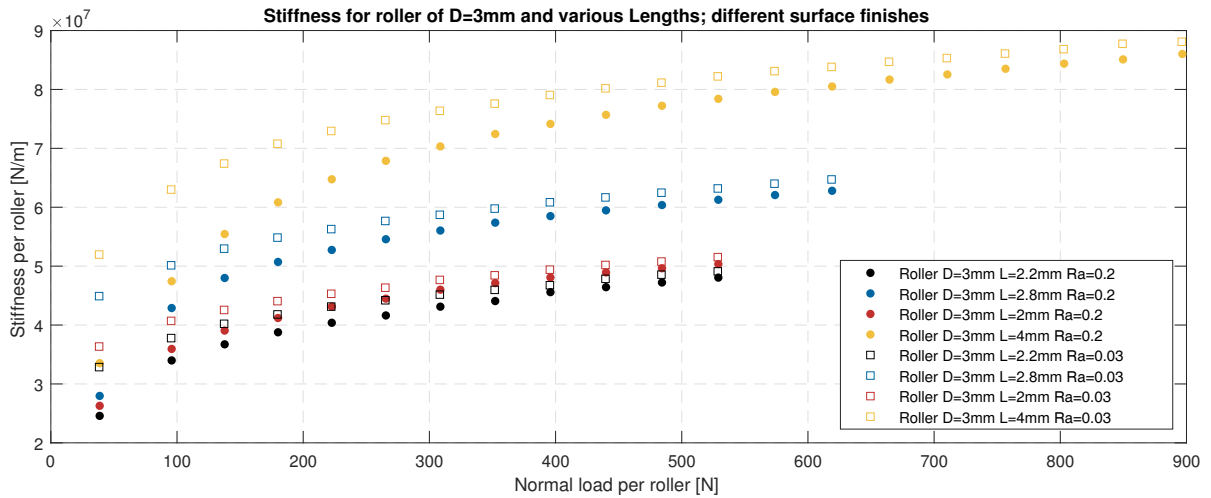


Figure 4.14: Hammer impact data: Load-stiffness relation for roller types 1, 5, 6, and 7 under normal conditions; Mean values for different surface finishes.

At a load of 30 % of C_0 , with $Ra=0.03 \mu\text{m}$ a stiffness increase between 2 % and 3 % relative to the standard finish is measured. The largest influence of the surface finish is measured for the longest rollers and the lowest load, this is expected as this is the lowest load per contact length. At a load of 10 % of C_0 , a typical preload in linear bearing assemblies, the measured stiffness increase is between 6 % and 8 %.

Roller material The influence of the rail surface finish for ceramic and stainless steel rollers is also tested.

Figure 4.15 shows the standard and mirror finish data for ceramic rollers.

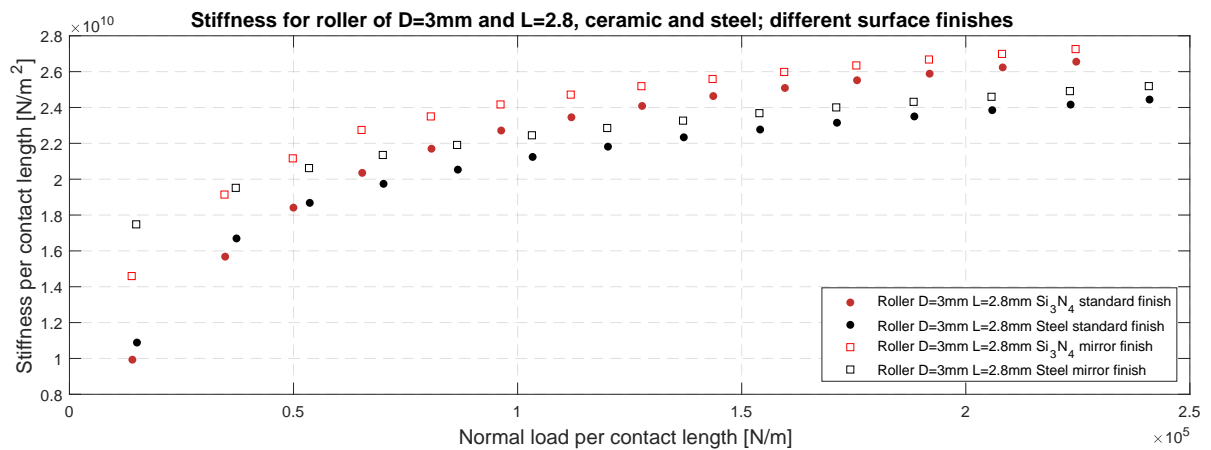


Figure 4.15: Hammer impact data: Load-stiffness relation of Ceramic and steel rollers under normal conditions; Mean values for different surface finishes.

The surface finish has the similar effect on ceramic rollers as on steel rollers.

Figure 4.16 shows the standard and mirror finish data for stainless steel rollers.

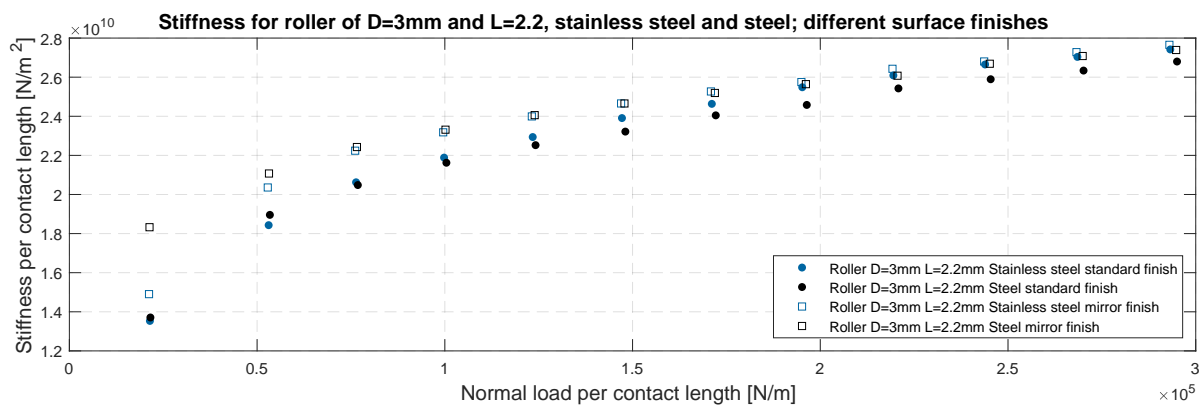


Figure 4.16: Hammer impact data: Load-stiffness relation of Stainless steel and steel rollers; Mean values for different surface finishes.

For stainless steel, only a small difference between the standard and mirror finish is measured. Again, stainless steel shows a higher stiffness at high loads compared to bearing steel. The hypothesis posed in Subsection 4.2.8 is backed by the measurements on mirror finish rails, as here the difference between stainless steel and bearing steel recedes.

When considering the results for all rollers it becomes clear that the stiffness increases with a smoother surface. This is in accordance with McCallion and Truong [39]. Considering Greenwood and Tripp it may be expected to see larger fluctuations in the measured load-stiffness relation for rough contacts as the number of asperities is small, this is most dominantly at lower loads, this was also measured.

4.3. Relating the experimental data to theory

With all the data presented in the previous section, a comparison can be drawn with the modelling in Section 3 and the experimental data obtained in this Chapter. The main question of this chapter is how to practically apply the Tripp solution to the finite dimensions in linear roller bearings. This section will make an effort to answer this question. No data on direct stiffness measurements of cylindrical roller-rail contacts is present in the literature yet. Based on the experiments presented in Section 4.2, two empiric load-stiffness relations are given, each of a simple logarithmic form.

Section 3.6 introduced a method for numerically modelling a complex geometry with non-conforming contacts as the same geometry with the contacts replaced by rigid inlays and stiffness elements, with the stiffness set using the Tripp solution.

The experimental results showed a clear distinction between the two surface finishes, these two conditions are also parted when comparing the data to the theory.

Standard finish Figure 4.17 presents all normal steel measurements performed on rails with a normal surface finish combined in one figure. The stiffness obtained by taking the derivative of the Tripp solution is also depicted. The compression of a roller and two half-spaces with a depth of the rigid inlays as modelled according to 3.6.

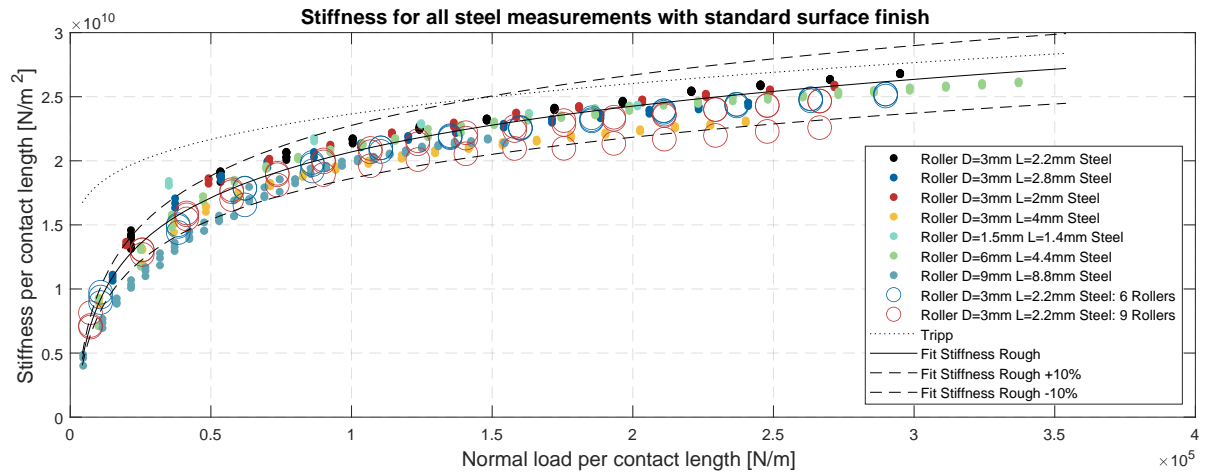


Figure 4.17: Hammer impact data: Load-stiffness relation of all steel rollers and normal surface finish under normal conditions; Mean values for different geometries and conditions. Curve fit of Equation 4.2.

The Tripp solution shows to be an upper limit for the stiffness measured, this is in line with what may be expected from the literature as the model assumes ideal conditions. Especially for low loads a reduced stiffness is measured, this lower stiffness is likely a result of the surface roughness. It is important to point out that the roller of type 1 is over-represented in this data set as most measurements are performed with this roller type. A least squares logarithmic fit of the data is also plotted, almost all data points fall in a $\pm 10\%$ range around this fit which is described in Equation 4.2.

$$k_{Ra_{0.2}} = 5.15 \cdot 10^9 \text{ N/m}^2 \ln \frac{P/L_{we}}{1.80 \cdot 10^3 \text{ N/m}} L_{we} \quad (4.2)$$

Mirror finish Figure 4.18 shows the combined data of all steel measurements with a mirror finish.

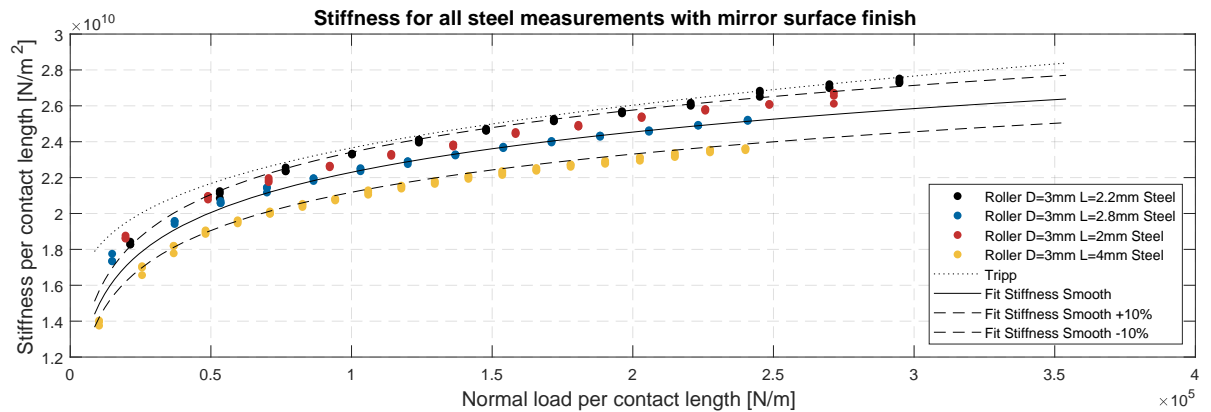


Figure 4.18: Hammer impact data: Load-stiffness relation of all steel rollers and mirror surface finish under normal conditions; Mean values for different geometries and conditions. Curve fit of Equation 4.3.

Here the measured stiffness aligns more closely with Tripp, it still can be seen as an upper limit, this is reasonable as Tripp does not account for the surface roughness which is most dominantly present in rough contacts. In this data set all roller types are represented with an equal weight, the lower quality of roller type 6 lowers the overall stiffness fit given in Equation 4.3. Overall, the Tripp solution appears to be a reasonable approximate for modelling the stiffness of rollers in contact with mirror finished rails.

$$k_{Ra_{0.03}} = 3.23 \cdot 10^9 \text{ N/m}^2 \ln \frac{P/L_{we}}{1.00 \cdot 10^2 \text{ N/m}} L_{we} \quad (4.3)$$

4.4. Synopsis

These experiments have shown that the test setup is a method with great precision and accuracy for measuring the stiffness of roller-rail contacts.

- Experimental quality
 - Modal analysis experiments have a high precision, especially at higher loads with variations smaller than 1 %, see Table F.3.
 - Stiffness calculated using the capacitive probe shows the same load-stiffness relation as modal analysis experiments but with a lower precision, see Appendix E.
 - Measurements with steel balls as known reference yield good results on the absolute accuracy of the setup, see Subsection 4.2.2.
 - The repeatability of the setup is greater than the product variations within a roller batch, statistically significant, see Table F.1.
- Roller geometry
 - Longer rollers of the same diameter show lower stiffness per contact length, this is a logic result when comparing to Figure 3.18 in Subsection 3.5.4. This view might be distorted due to the low roller quality of the longest roller, or this could be a non-linearity in the setup. Another cause could be the limited straightness of rollers, which results in a nonuniform contact for longer rollers.
 - No direct conclusions can be drawn from varying the roller diameter, as it was not varied independent of roller length, these measurements support the claim that the stiffness per contact length reduces with contact length, see Subsection 4.2.6.
 - Measurements with an increased number of rollers placed parallel in the setup resulted in a lower effective stiffness per roller. This could be a result of an over-constrained geometry such that the contacts are less than ideal. This reduced effective stiffness could also be attributed to roller to roller variations in roller diameter which makes rollers with a slightly smaller diameter less contributing. Again non-linearity in the experiment setup cannot be ruled out. See Subsection 4.2.7.
- Lubrication
 - In static conditions no significant change in behaviour was measured by adding either oil or grease. see Table F.2. Note that static conditions do not allow for the formation of an EHL Film.
- Roller material
 - Ceramic rollers are 6 % stiffer compared to steel rollers, this is in line with literature as ceramic has a higher Youngs modulus, see Table A.1.
 - Stainless steel rollers are stiffer than steel rollers of same length, this could be explained by the difference in material hardness. A lower hardness of the roller can result in better conformation in the contact, see Subsection 4.2.8.
- Surface roughness
 - The Influence of the rail surface finish has been studied by comparing mirror finish rails with standard ground rails.
 - For balls the influence of the surface finish on the stiffness is in line with what is expected from the theory of Greenwood.
 - Figure 4.13 shows how a similar effect is measured for rollers, the stiffness increases with a smoother surface. An increase in stiffness was measured for all measurements performed with mirror finish rails.
 - A smoother surface results in a lower stiffness variance, especially for low loading conditions.
- Modelling
 - The Tripp model is an upper limit for measurement on real rollers with tolerances.
 - Equation 4.2 predicts the stiffness of a rough ($R_a=0.2 \mu\text{m}$) roller-rail contact within 10 % for all rollers measured¹.

¹one outlier, the largest rollers of type 12

5

Stiffness of a roller between two rails at 45°

Chapter 4 investigated the modelling and experimental validation of individual rollers normally compressed between two flat rails. The step to a full bearing assembly, a complex geometry with multiple rollers loaded at 45°, is too complex without further comprehending the characteristics of the individual components.

This Chapter bridges this gap by studying individual rollers loaded at 45°. It identifies a practical model for this geometry and investigates how normal and tangential stiffness components coexist.

As discussed in Chapter 2, there is no consensus on how to model a roller loaded at 45°. Some authors [46, 52, 54, 54, 55] solely rotate the normal load components and do not account for any tangential effects. Some model the geometry as a "black box" with both a horizontal and vertical stiffness [58]. No experimental data on the stiffness of individual rollers loaded at an angle exists yet.

Experimental data on the tangential stiffness of normally loaded rolling elements does exist for spheres [59], yet data is not extended to cylinders. The effect of the tangential contact force component is greatly discussed in train wheel-rail contact, though the profiling of train rails is such that no line contact is present.

This Chapter will discuss performed experiments on individual rollers compressed between two rails at an angle of 45°. The goal of the conducted experiments is to extend the insights gained with the normal experiments of Chapter 4 and determine how this extended system should be modelled. The traction stiffness of normally loaded rollers is measured.

In this chapter, the influence of the following parameters is investigated:

- Load
- Roller orientation
- Product variations
- Lubrication
- Length
- Diameter
- Material
- Number of rollers

First, this Chapter describes the system of roller-rail contact at an angle. Section 5.2 covers the experimental setup on which the experiments are performed. Section 5.3 address the results, first it presents the measurements at 45° and second the traction stiffness of normally loaded rollers. Section

5.4, draws a comparison between the normal and 45° conditions, shows the significance of the results and presents a model to predict the stiffness of a roller in a 45° orientation.

5.1. Description of the roller-rail system at 45°

Figure 5.1a shows a schematic of the geometry considered in this chapter. This geometry is an extension of the normal system shown in Figure 3.1a of Chapter 4.

Merely loading the roller-rail contact at 45° results in a situation shown in Figure 5.1b. The applied load (F_z , \rightarrow) is supported by the roller. The reaction force of the roller (F_n , \rightarrow) has to act in a direction normal to the rail surface, as the reaction forces have to share a line of action not to cause a couple that rotates the roller.

The reaction force of the roller expressed as a function of the vertically applied load is $F_n = \frac{F_z}{\cos(\alpha)}$, with α the angle between the load and the rail surface. Here the stiffness in the direction of the applied load is $k_z = k_n \cos^2(\alpha)$.

In bearing assemblies, the roller axis is oriented parallel to the rolling direction, as shown in Figure 5.1a. With friction in place, the applied load is here also supported by tangential components (F_t , \rightarrow). The sum of the normal and tangential load projected in the z -direction form the equilibrant force for the applied load i.e. $F_z = F_n \cos(\alpha) + F_t \sin(\alpha)$ with α the angle between the load and the rail surface. The total deformation of the system is the sum of the deformation in the rails and the deformation of the roller in both the normal and the tangential direction.

The stiffness in the z -direction, the direction of the applied load is $k_z = k_n \cos^2(\alpha) + k_t \sin^2(\alpha)$. The tangential components create a couple on the roller, a nonuniform normal load (\rightarrow). Misalignment will emerge to ensure a static equilibrium. It is assumed that the rails are supported such that the normal and tangential components do not need to cancel out in y -direction.

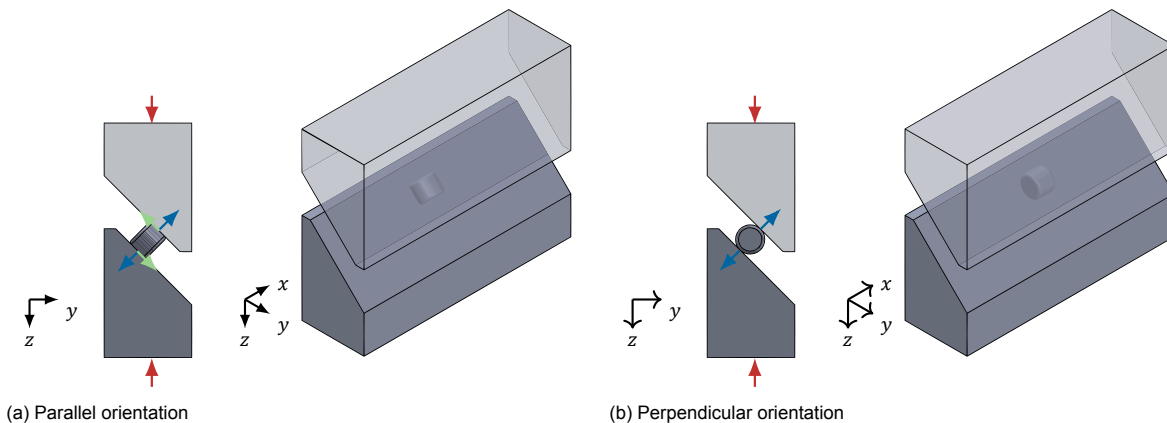


Figure 5.1: Schematic of a rollers compressed between two rails at an angle of 45°.

Besides the factors that determine a normally loaded contact, preliminary research found the following effects to come into play when loading at an angle:

- Friction
- Creep
- Misalignment

The consequences of including the tangential contact interactions are far reaching and complicated. The applied load is supported by both tangential and normal components of the reaction force. The reaction forces in turn interact with the stiffness and the slip limit. Developing a numerical model of this problem would require many assumptions on the contact conditions and behaviour at asperity level. There is a high probability of developing a model with little connection to reality, hence no numerical model is made here.

5.1.1. LEGO demonstration

Friction is required for the tangential load, in the case of slip no tangential stiffness component can exist. An LEGO mock-up as shown in Figure 5.2 demonstrates the fundamental influence of friction. A roller (a rubber LEGO tire) is loaded between two 45° rails (two LEGO roof tiles) and compressed. The left rails have been polished and lubricated while the right is a rough and dry contact as shown in Figure 5.2a. In the deformed situation of Figure 5.2b, there exists a clear difference between the lubricated and dry contact. The lubricated roller maintains a rectangular shape, while the dry roller becomes a parallelogram, this shear deformation results in a tangential reaction force and corresponding tangential stiffness.



(a) Undeformed



Video



(b) Deformed

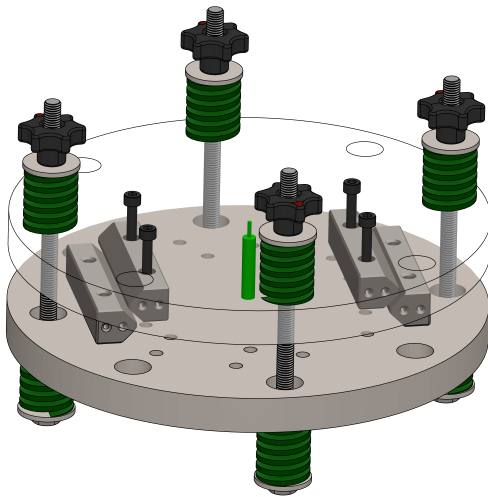
Figure 5.2: LEGO demonstration of a roller (here a rubber Lego tire) loaded between to rails (here LEGO roof tiles) at 45°. The left rails have been polished and lubricated while the right is a rough and dry contact.

5.2. Test setup

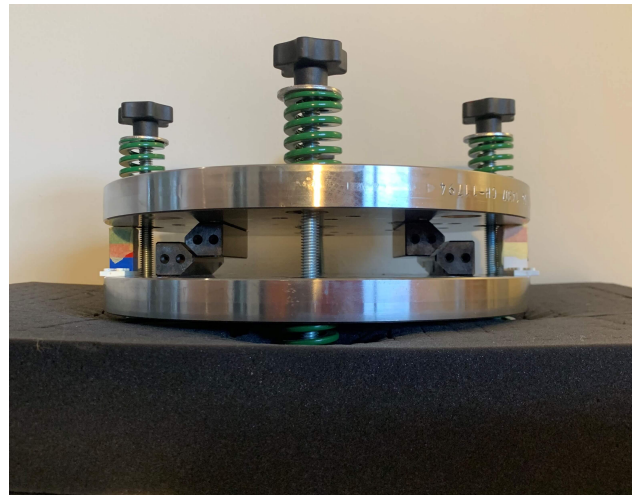
This section presents a new test setup, this setup is used to perform experiments of rollers loaded at an angle of 45° .

5.2.1. Description of the setup

The setup, as shown in Figure 5.3, is nearly identical to the setup used in Chapter 4, except that here the orientation of the rails is positioned to orientate the roller-rail contact at 45° .



(a) CAD model of 45° loaded setup



(b) Picture of 45° loaded setup

Figure 5.3: The test setup used for the experiments in this section. Two pairs of rails are bolted to the two solid disks. The rollers are placed between the rails in the rolling direction. When compressed, the green springs exert load on the rollers and rails. The distance between the masses is measured with a capacitive probe (bright green). The frequency response is measured with accelerometers. The setup is isolated from the external world by a suspension with a tube (both not in CAD).

Figure 5.4 shows a schematic of the test setup. The setup is modelled as a suspended two mass spring system. Here, k_n and k_t are each the sum of the components caused by the roller and rails, i.e. Equation 4.1. This setup has two rollers in parallel, the stiffness sum of the measured contacts is $\vec{k}_n + \vec{k}_t$.

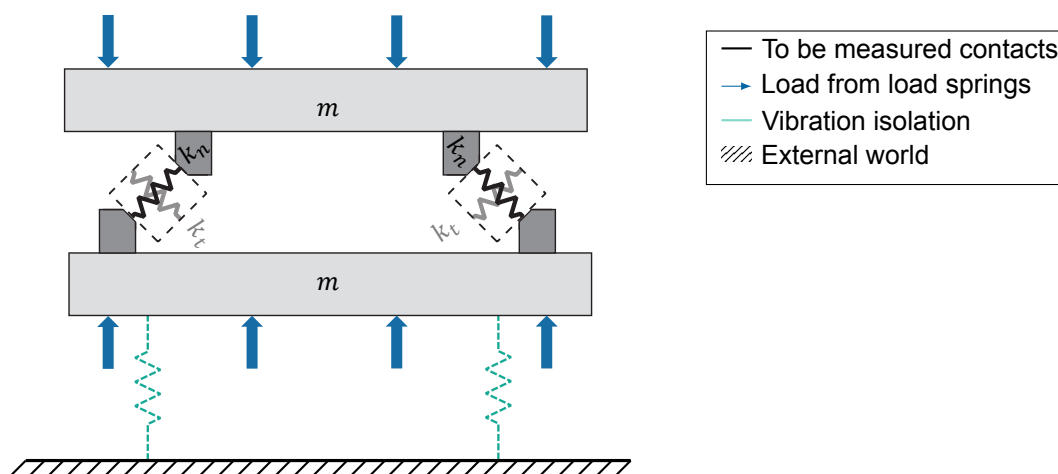


Figure 5.4: Schematic depiction of the normally loaded setup.

$$\begin{aligned}
\frac{1}{k_n} &= \frac{1}{k_{rail,n}} + \frac{1}{k_{roller,n}} + \frac{1}{k_{rail,n}} \\
\frac{1}{k_t} &= \frac{1}{k_{rail,t}} + \frac{1}{k_{roller,t}} + \frac{1}{k_{rail,t}} \\
k_z &= k_n \cos^2(45^\circ) + k_t \sin^2(45^\circ) = \frac{k_n}{2} + \frac{k_t}{2}
\end{aligned} \tag{5.1}$$

5.2.2. Multi body dynamics analysis of the setup

The goal of this model is to verify if the eigenmodes are distinguishable and to determine the stiffness of the setup itself.

The natural frequency of this idealized two mass spring system is $\omega_0 = \sqrt{\frac{4k_z}{m}} = \sqrt{\frac{2k_n+2k_t}{m}}$, with m the mass of one solid steel disk and attached rails and bolts. The stiffness of the setup is computed using a multi-body FEM model. This allows account for the finite rigidity of this setup. The contacts are modelled as proposed in section 3.6, with a stiffness only in the normal direction. This is not a problem since $\cos^2(45^\circ) = \sin^2(45^\circ)$. Spring elements are placed between the rigid inlays. The stiffness of these elements is swept over the range used during the experiments. The stiffness is found to be $2.22 \cdot 10^8$ N/m, and properly modelled to be in series with the three rail pairs. The found stiffness is significantly (roughly 5 times) lower than the stiffness of the setup used in Chapter 4. Yet, the stiffness sum of the to be measured contacts is roughly one third of the stiffness sum in the experiments of Chapter 4; $2 \cos^2(45^\circ) / 3 \cos^2(0^\circ)$. Although insignificant, the stiffness of the load springs is also deducted from the measurements for completeness.

5.2.3. Test procedure

The procedure is identical to the process described in Subsection 4.1.4. The load is increased to 30 % of C_0 in normal direction, i.e. the load when loading vertical, divided by $\cos(45^\circ)$. Gage blocks are used to align the two disks during assembly.

5.2.4. Test equipment

The same equipment is used as during the experiments in Chapter 4. See Subsection 4.1.5 for a description of the equipment.

5.3. Test results and discussion

This section presents and discusses the results of the experiments performed with a roller loaded at 45° . Table A.2 lists the surface roughness, roundness, and cylindricity of the rollers used. All the results in this section account for and deduct the stiffness of the rest of the geometry. All plots represent the stiffness of the rolling element and two times the highlighted region of Figure 3.22.

5.3.1. Precision of the setup

The goal of this experiment is to verify the test–retest reliability of this setup.

Figure 5.5 shows the stiffness per roller as a function of the normal load on a set rollers of type 1 that are tested 10 times. The spread of the data is expressed as a percentage of the mean stiffness for a certain load level.

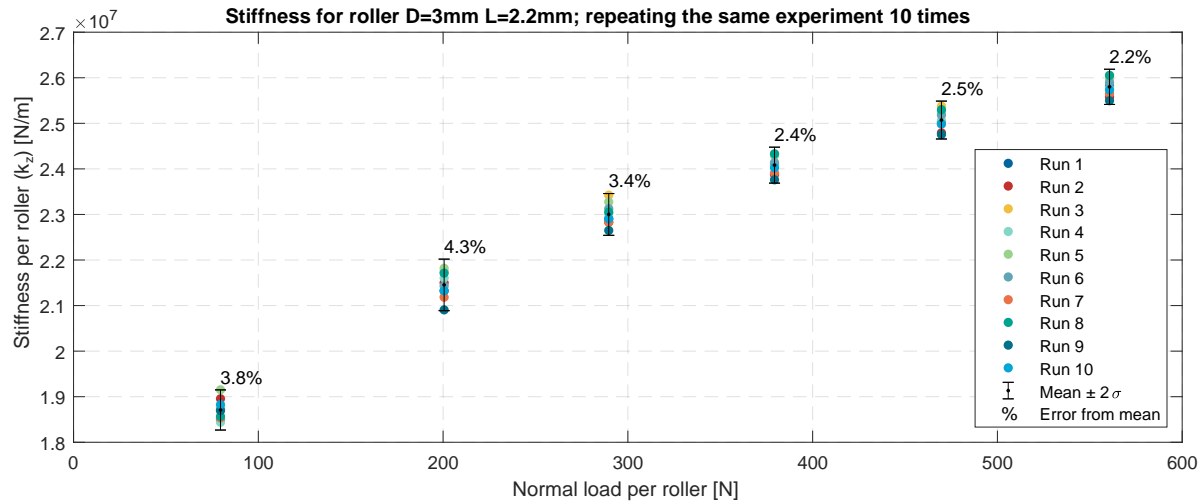


Figure 5.5: Hammer impact data: load-stiffness relation of roller type 1 under 45° conditions; 10 runs, estimating repeatability.

These results show a total spread of the measured stiffness less than 5%, this spread narrows for higher loads to less than 3% ($\sigma = 2.5 \cdot 10^5$ N/m). This repeatability is less precise compared to the experiments performed on the normal setup in Subsection 4.2.1. A few possible reasons for the observed decrease could include; the use of two instead of three rollers makes the setup under-constrained and could lead to misalignment. A small offset from the center of the impact location will result in a tilt of the disk and misalignment of the rollers.

Nevertheless, it may be concluded that the setup and the performed modal analysis experiments are precise, particularly at higher loads. The mean standard deviation is 1.03% of the mean stiffness measured. Other experiments show similar measurement precision, see Table H.2.

5.3.2. Product variations of rollers

All rollers are manufactured according to predefined tolerances, however, dimensions range within these tolerances. Surface profiles and grain structures are unique and vary from roller to roller. As a consequence, every roller will have a different mechanic behaviour. Studying this spread in load-stiffness relationships will provide an upper limit for the accuracy of meaningful roller modelling.

Figure 5.6 shows the stiffness per roller as a function of the normal load for different sets of type 1 rollers.

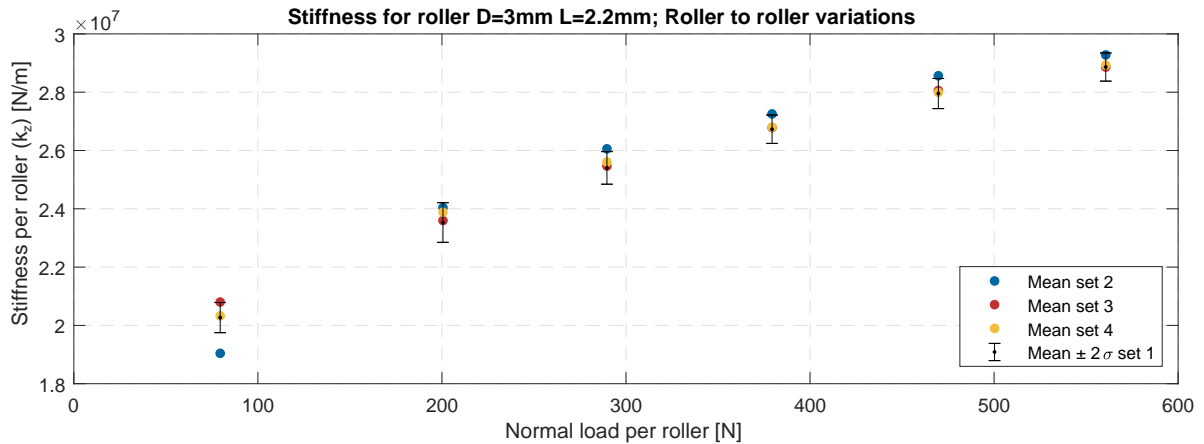


Figure 5.6: Hammer impact data: load-stiffness relation of roller type 1 under 45° conditions; Mean values roller to roller variation.

The means presented as roller set 1 is the mean of the data shown in Figure 5.5. The measured roller set to roller set variations among repetitions of the same set are similar to the variations between sets. Owing to the increased variance with this setup, the data did not pass a Levene's test. Hence, no statistical conclusions can be drawn from this experiment.

5.3.3. Influence of roller orientation

Subsection 5.1 covered how the system behaviour can be influenced by the roller orientation given there is friction. This experiment investigates the influence of the roller orientation. Two rollers of type 1 were oriented perpendicular to the rolling direction, likewise Figure 5.1b.

Figure 5.7 depicts this measurement against the results of the precision measurements where the roller is oriented parallel, as shown in Figure 5.1a.

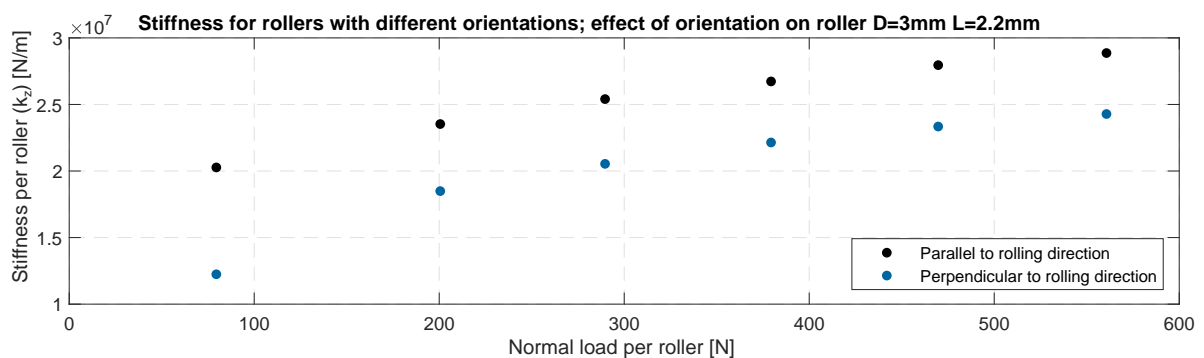


Figure 5.7: Hammer impact data: load-stiffness relation of roller type 1 under 45° conditions; roller orientation.

Roller orientation has a clear effect on the measured load-stiffness relation, the perpendicular orientation yields 18 % lower mean stiffness, see Appendix H. Consequently, this substantiates the hypothesis that tangential components influence the behaviour of the system at 45°. Additional normal experiments were performed with a rotated roller direction to assure this effect is not caused by the surface topology and grinding direction, this measurement is shown in Figure G.3.

5.3.4. Variation of contact length

Section 2.2.1 discussed the influence of roller profiling and end-effects.

Figure 5.8 shows the stiffness per contact length (L_{we}) as a function of the normal load for rollers of various contact length. This experiment uses rollers type 1, 5, 6, and 7 with length $L = 2.2, 2, 2.8,$ and 4mm , and contact length $L_{we} = 1.793, 1.947, 2.569,$ and 3.734mm respectively.

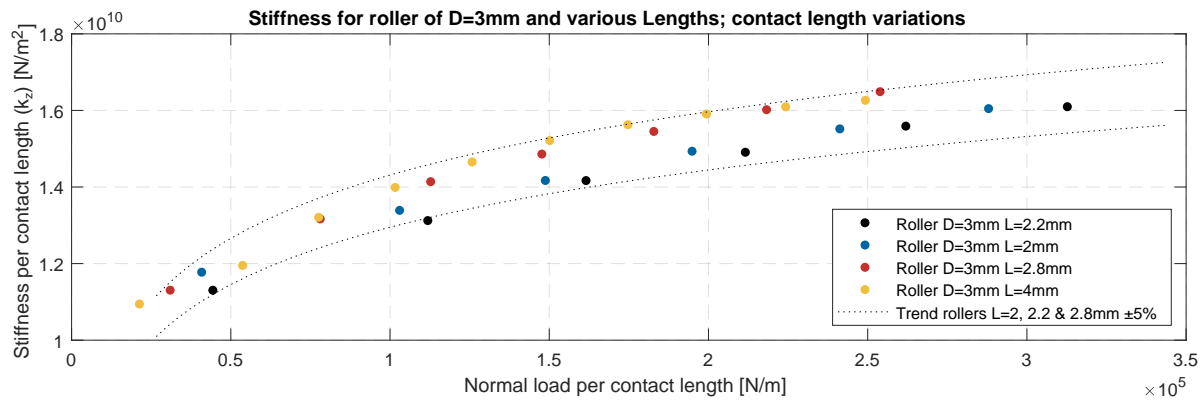


Figure 5.8: Hammer impact data: load-stiffness relation for roller types 1, 5, 6, and 7 under 45° conditions; Mean values for rollers of various contact length.

The results show a significantly lower stiffness per contact length for roller type 6. This roller is from a different manufacturer and has lower quality, see Subsection 4.2.5.

The contact length of the rollers with length $L_R = 2.2, 2,$ and 2.8mm is $L_{we} = 1.793, 1.947,$ and 2.569mm respectively. A logarithmic curve fit of the three other rollers has been plotted with a $\pm 2.5\%$ offset to quantify the spread in measured stiffness for these rollers. This data lacks a homogeneity of slopes, such that no statistical test could be performed. Curve fitting the data suggests that the stiffness per contact length increases with contact length. However, the perceived effect is very small and could be caused by a non-linearity of the corrected setup.

5.3.5. Variation of roller diameter

Experiments are performed with various roller diameter to investigate the influence of diameter on the load-stiffness relation for normal loading conditions.

Unfortunately, roller length is not held constant during this experiment as rollers of constant length with various diameters were not available. Diameters 1.5, 6, and 9 mm were tested and compared with the existing data for 3 mm rollers.

The static load rating $C0$ scales linear with roller diameter. Hence, for larger diameters measurements could be performed with greater loads. The springs limited the maximum applied per contact length for the 9 mm rollers.

Figure 5.9 shows the stiffness per contact length (L_{we}) as a function of the normal load for rollers of various diameter.

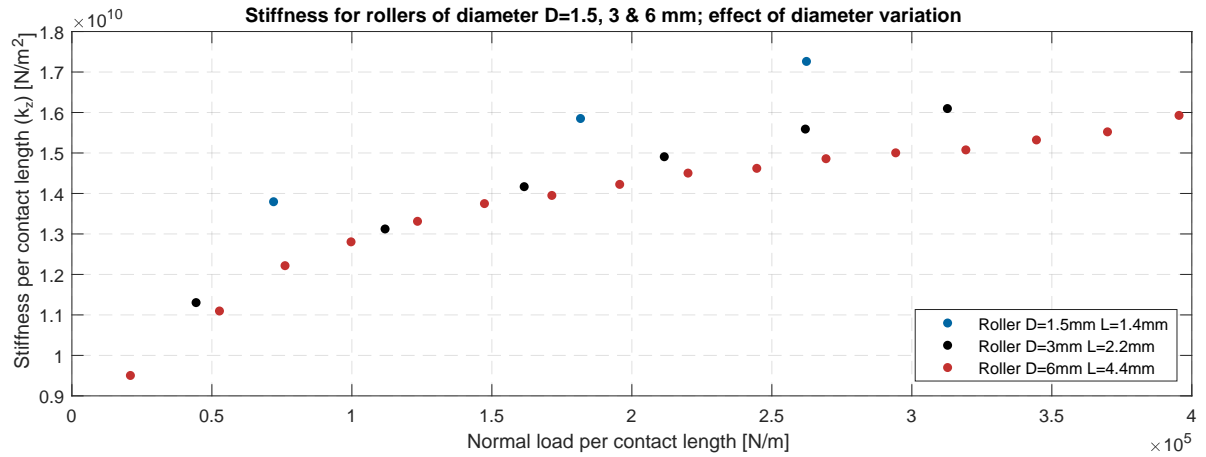


Figure 5.9: Hammer impact data: load-stiffness relation for roller types 1, 2, and 3 under 45° conditions; Mean values for rollers of various diameters.

The stiffness significantly decreases with roller diameter. Considering the small effect of roller length, as indicated in Figure 5.8, these results suggest that the observed effect is caused by the roller diameter. The stiffness per contact length scales roughly with D_w^{-2} .

Measurements on the 1.5 mm rollers were difficult as the FRF showed multiple peaks, this is shown in Figure 5.11. The data was not as clean as measurements on the other rollers as depicted in Figure 5.10.

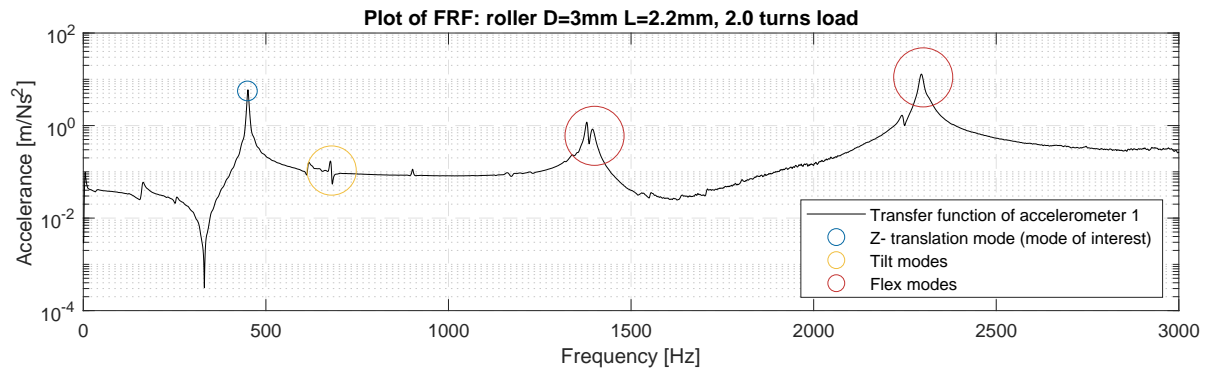


Figure 5.10: Hammer impact data: Transfer function for rollers type 1 at 45°, under 1.5 turns load; Example of a typical transfer function

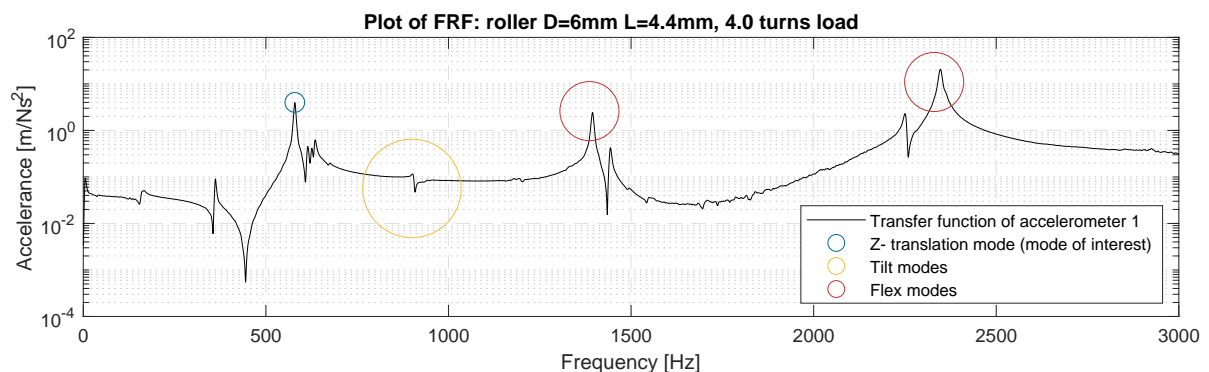


Figure 5.11: Hammer impact data: Transfer function for rollers type 3 at 45°, under 4.5 turns load; Example of a poor FRF

5.3.6. Influence of lubrication

The presence of lubrication might influence the damping of the hammer impact measurements. Experiments were performed using both grease and oil, *Lubcon Thermoplex ALN 1001/00* [67] and *Klüber Summit SH 32* [68] respectively. It is important to point out that these experiments were performed under non-rolling conditions so no EHL layer could be formed.

Figure 5.12 shows the stiffness per roller as a function of the normal load for rollers of various lubrication conditions.

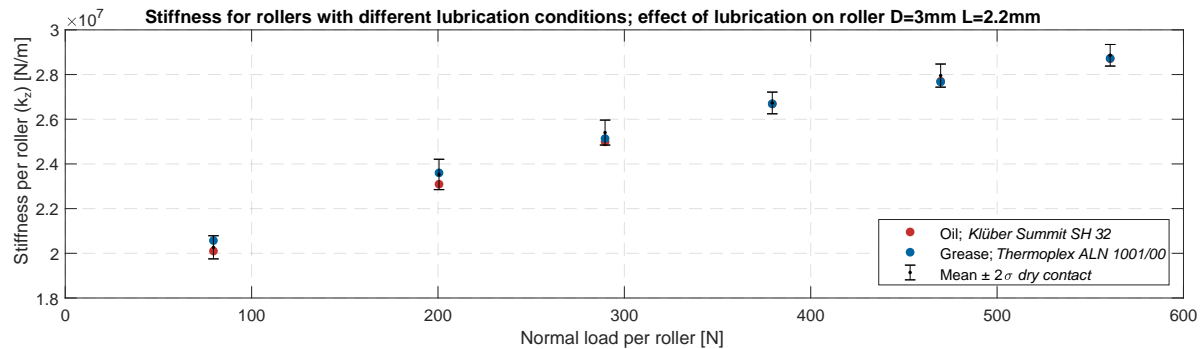


Figure 5.12: Hammer impact data: load-stiffness relation for roller type 1 under 45° conditions; Mean values for rollers with different lubrication conditions.

Figure 5.12 shows that there is no significant effect of neither lube nor oil on roller stiffness after controlling for the load (One-way ANCOVA, $F(2, 188) = 1.182$, $p = 0.309$). This analysis is reported in Appendix H.

5.3.7. Variation of the number of rollers

Experiments with an increased number of rollers allow for the investigation of the influence of misalignment and parallelism and the tolerance on roller diameter. Therefore experiments are performed with 2, 4, and 6 rollers in the setup. The rollers used are of type 1. The stiffness values for the setups with 2, 4, and 6 rollers are $2.220 \cdot 10^8$ N/m, $2.530 \cdot 10^8$ N/m and $3.480 \cdot 10^8$ N/m respectively.

Figure 5.13 shows the stiffness per roller as a function of load applied for 2, 4, and 6 type 1 rollers.

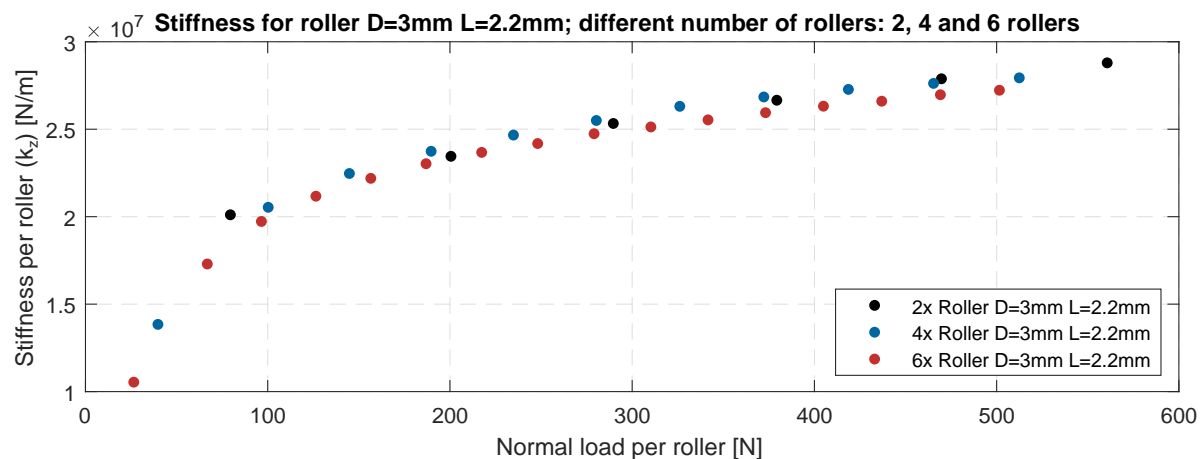


Figure 5.13: Hammer impact data: load-stiffness relation for roller type 1; Mean values for different number of rollers.

The effective stiffness per roller decreases with the number of rollers. This effect is comparable to the effect measured for the normal measurements in Subsection 4.2.7.

5.3.8. Influence of roller material

In order to test the influence of roller material, both stainless steel and Ceramic rollers were tested and compared with bearing steel. Not only the roller material was varied, also the contact length varies slightly due to differences in roller profiling. To compensate for this as much as possible, the stiffness and loads are plotted per contact length. The stainless steel (1.4034) rollers, are type 9 in the roller table. The ceramic, silicon nitride, rollers are type 8 in Table A.1.

Figure 5.14 shows the measured load-stiffness relation of ceramic (Si_3N_4), and bearing steel rollers, type 8 and 5 respectively.

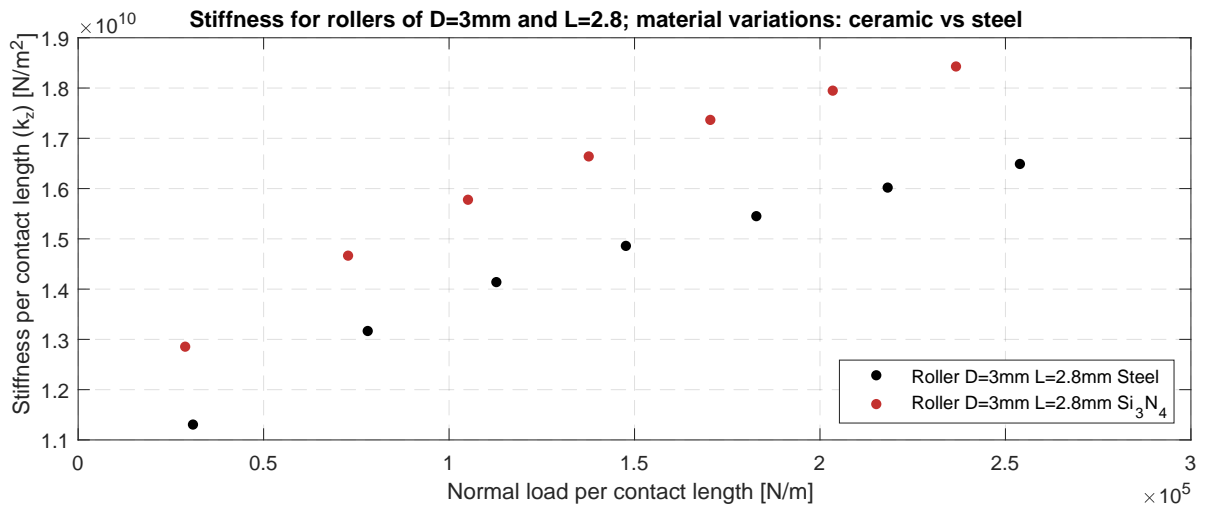


Figure 5.14: Hammer impact data: load-stiffness relation of rollers of different materials under 45° conditions; Mean values for Ceramic and steel rollers.

The ceramic roller is stiffer than a steel roller of the same length, which is expected as deflection is a function of the effective elasticity modulus. No accurate data is available on the material properties of the ceramic roller. This complicates quantification of a difference between the ceramic and steel rollers.

Figure 5.15 shows the measured load-stiffness relation of stainless and steel rollers, type 9 and 1 respectively.

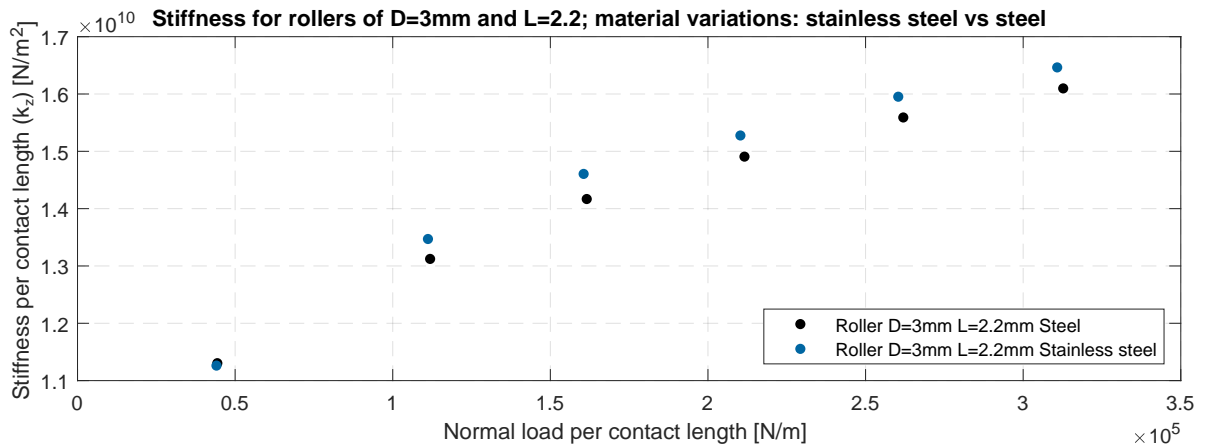


Figure 5.15: Hammer impact data: load-stiffness relation of rollers of different materials under 45° conditions; Mean values for stainless and steel rollers.

The stainless steel roller is stiffer than a steel roller of the same length. This result is expected from the normal measurements. While the Young's modulus of the stainless steel roller is 200 GPa, lower than the 210 GPa for the bearing steel roller. The hardness of the stainless steel roller is lower. The lower hardness of the stainless steel roller allows it (at higher loads) to deform plastically and conform to the roughness profile of the rail, and therefore increases the effective area.

5.3.9. Tangential stiffness

The results of the experiments with different roller orientation shown in Figure 5.7, suggests that the tangential components do play a role in the system behaviour. It is therefore relevant to measure the individual normal and tangential stiffness components and compare them to the measurements at 45°. To measure the individual components, an additional setup configuration was constructed. It consists of two rail pairs that are normally opposed, see Appendix G on this setup. The variance of the tangential stiffness components is comparable to that of the normal measurements, see Table H.2.

Figure 5.16 presents different normal load-tangential stiffness relationships for roller types 1, 2, 3, 4, 5, 6, and 7.

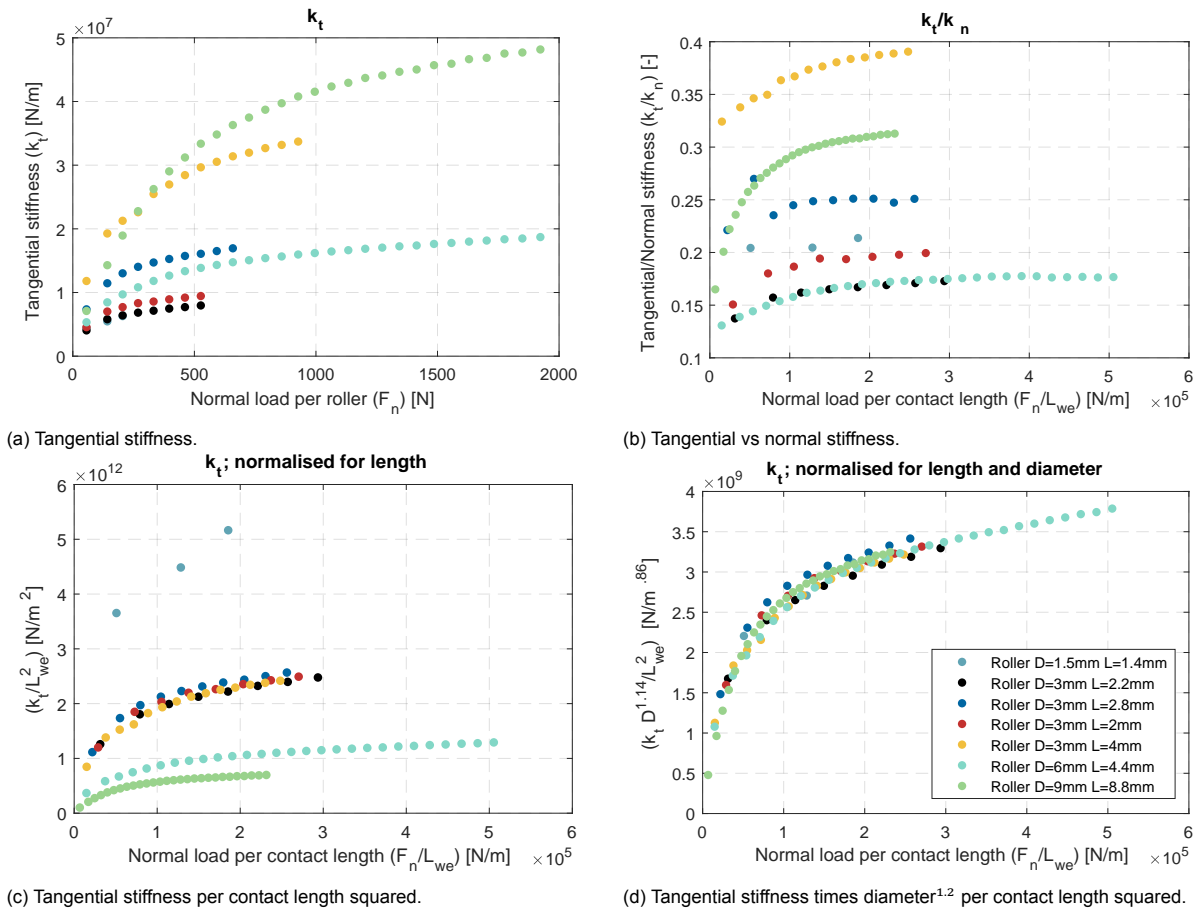


Figure 5.16: Hammer impact data: load-stiffness relation for roller types 1, 2, 3, 4, 5, 6, and 7; tangential stiffness.

Figure 5.16a shows that the tangential stiffness increases with contact length. In section 5.3 it was shown that the load-stiffness at 45° scales roughly linearly with contact length. The influence of the roller diameter appeared to be considerable.

However, Figure 5.16b indicates how the tangential stiffness components does not scale in a similar manner as the normal stiffness. The tangential stiffness is not a constant fraction of the normal stiffness.

Figure 5.16c shows that in relation to the contact length, the results indicate that the tangential stiffness scales approximately with the contact length squared, non-linear regression estimates its power 2.023. Furthermore, there is an inverse relationship between the roller diameter and the tangential stiffness. This is in line with the results from Subsection 5.3.5.

Figure 5.16d shows that the tangential stiffness scales roughly with the roller diameter^{-1.14}, a non-linear regression estimates its power 1.141. The tangential stiffness of the rail components is expected not be influenced by the roller diameter directly, again no conclusions can be made as in the rollers measured, the diameter is coupled with the roller length.

5.4. Relating the experimental data to theory

The main endeavour of this chapter is how to practically model individual rollers at a 45° orientation. No measurement data on roller-rail contacts at an angle is present in literature yet. To start, based on the experiments presented in Section 5.3.9, an empiric load- tangential stiffness relations is given in Subsection 5.4.1. This model is combined with the fits for the normal load-stiffness relation in Section 4.3 to create a model for a roller at 45° in Subsection 5.4.3.

5.4.1. Quantifying the tangential stiffness

In Subsection 5.3.9 the tangential stiffness measurements are presented and studied their scaling with respect to roller length and diameter. A least squares regression is conducted on the normalized data, the resulting fit is given in Equation 5.2.

$$k_t = 8.157 \cdot 10^8 \text{ N/m}^{1.86} \ln \frac{P/L_{we}}{4.235 \cdot 10^3 \text{ N/m}} L_{we}^2 D_w^{-1.14} \quad (5.2)$$

It is important to indicate that roller type 1 is over-represented in this data set as most measurements are performed with this roller type.

Figure 5.17 compares the load tangential stiffness relation for the rollers of type 1, 2, 3, 4, 5, 6, and 7, with the fit given in Equation 5.2.

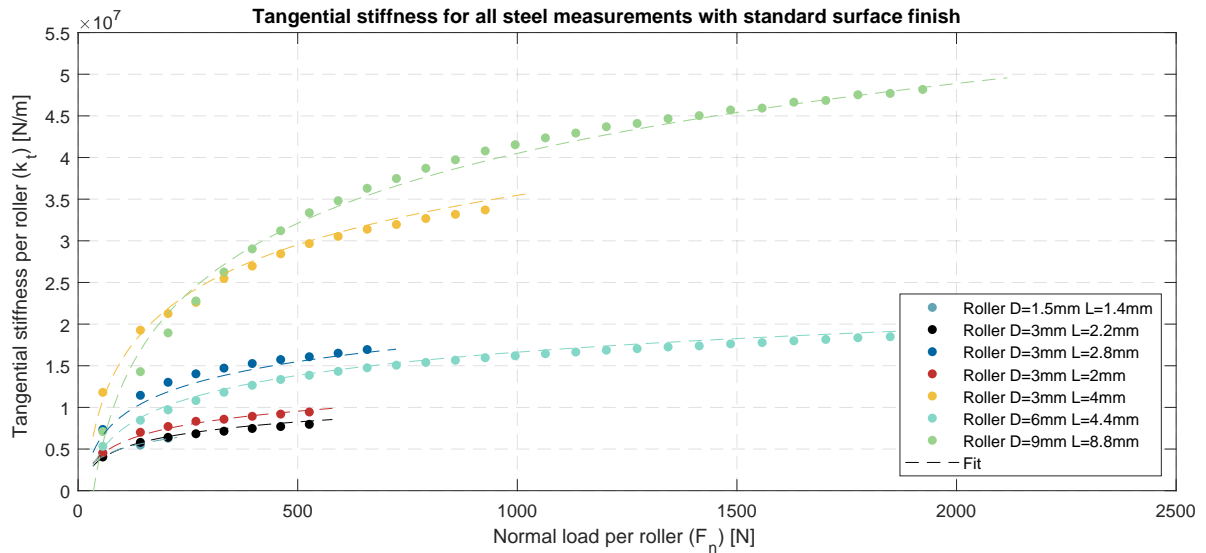


Figure 5.17: Hammer impact data: load-stiffness relation for roller types 1, 2, 3, 4, 5, 6, and 7; tangential stiffness with curve fit of Equation 5.2.

For nearly all data points, the fitted model approximates the experimental data within $\pm 3\%$. This indicates a good fit of the prediction of the tangential stiffness-load relation. This is a better prediction than the fit presented for the normal stiffness in Section 4.3, yet this is a higher order fit as it also incorporates the parameters L_{we} and D_w in a nonlinear manner. The variance of both measurements are comparable, as is shown in Appendix H.

5.4.2. Individual stiffness components compared to 45° measurements

The question emerges how the normal, tangential and the measurements at 45° relate.

Figure 5.18 compares the load - individual stiffness components relations for a rollers of type 1.

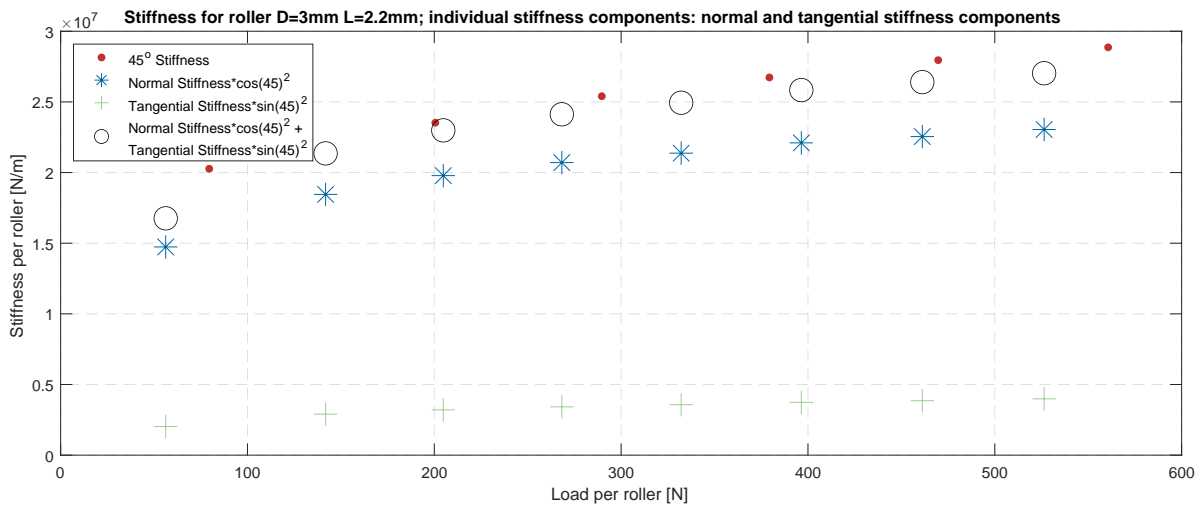


Figure 5.18: Hammer impact data: load-stiffness relation for roller type 1; individual stiffness components.

This comparison supports the hypothesis that the sum of the individual components add up to the measurements at 45°. Here its shown how a perpendicular roller orientation, the orientation where no tangential stiffness can be present, yields a stiffness equivalent to a vector rotation of the normal stiffness in a normal setup.

Figure 5.19 extends this hypothesis to all steel rollers tested at 45°, it compares the measurements at 45° with the sum of the individual components for rollers type 1, 2, 5, 6, and 7.

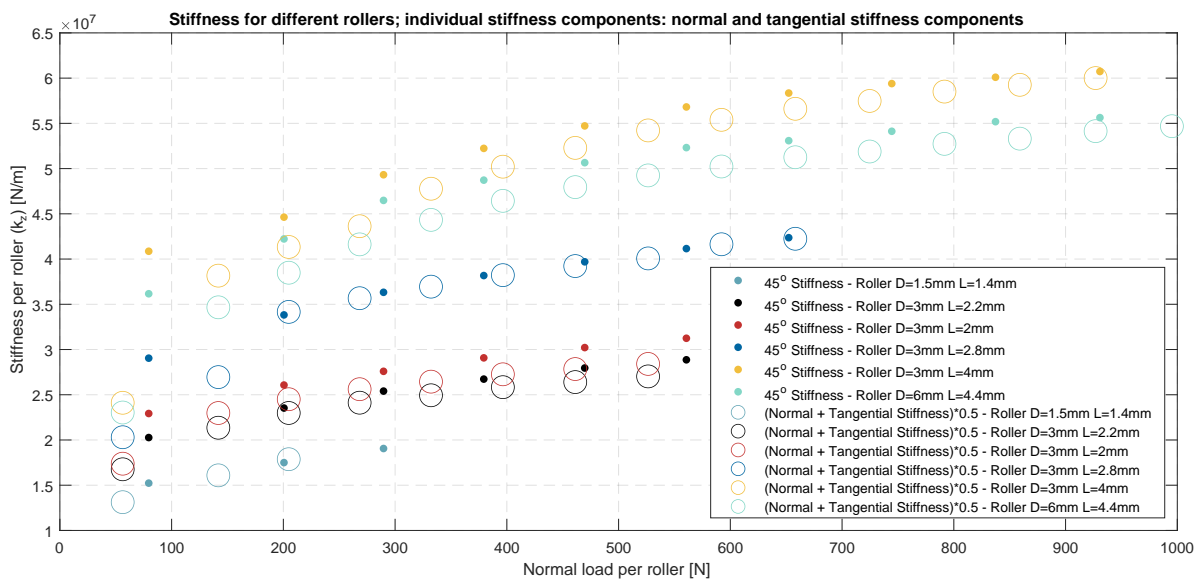


Figure 5.19: Hammer impact data: load-stiffness relation for roller types 1, 2, 5, 6, and 7; 45° measurements compared with vector sum.

Again it is apparent how the sum of the individual components add up to the measurements at 45°. It is important to indicate that these measurements are conducted in static condition, no EHL lubrication can occur in the contact. Additionally, during rolling motion, creep can take place, which is not the case in these experiments.

To further support this hypothesis, the measurements performed with a perpendicular roller orientation are compared to the normal measurements with the same number of rollers. As the perpendicular orientation can only transmit a normal force, no tangential stiffness is measured. For this orientation only normal forces can be transmitted. If the hypothesis holds up, the normal and 45° measurements should match after performing the relevant vector transformations.

Figure 5.20 shows on the horizontal axis the normal load on the roller, i.e. $F_z/\cos(\alpha)$ with α the angle of the rail.

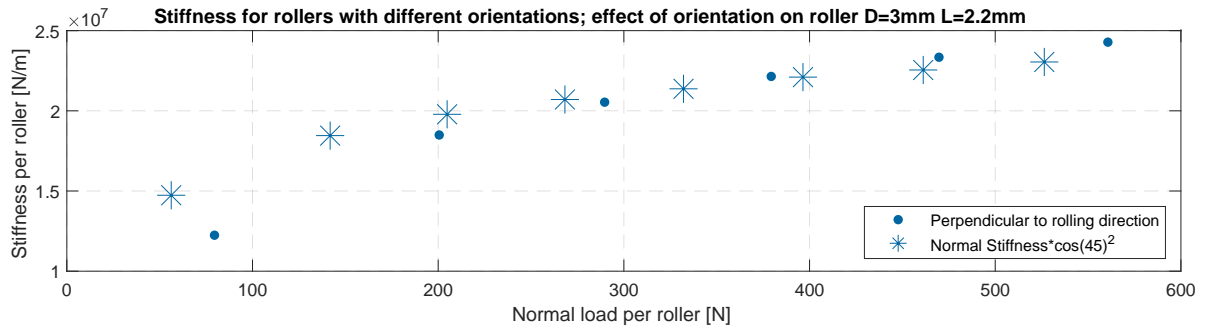


Figure 5.20: Hammer impact data: load-stiffness relation for roller type 1; 45° measurement with perpendicular orientation compared to normal measurement.

The vector sum of the normal and tangential stiffness components add up to the stiffness measured at 45°.

5.4.3. Modelling a roller at 45°

Figure 5.21 depicts the stiffness measured at 45° against the vector sum of normal and tangential load-stiffness relations, equations 4.2 and 5.2 respectively.

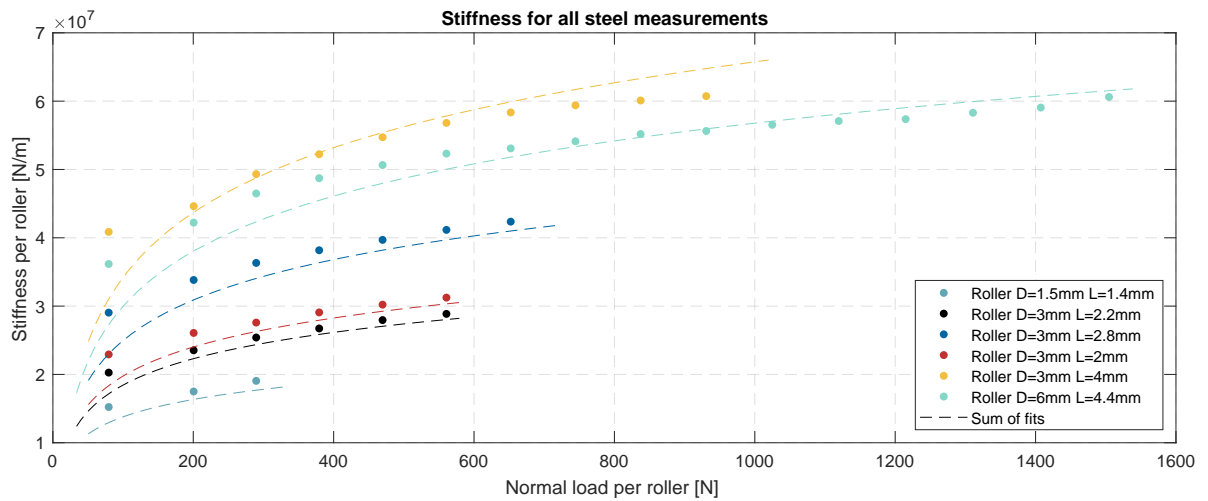


Figure 5.21: Hammer impact data: load-stiffness relation for roller types 1, 2, 5, 6, and 7; 45° measurement compared with sum of fits (Equation 5.3).

This Figure shows how a roller at 45° can practically be modelled as a rotation of a normally loaded roller where both the normal and tangential stiffness are considered. Such that the stiffness in the z -direction, the direction of the applied load is $k_z = k_n \cos^2(\alpha) + k_t \sin^2(\alpha)$. Given the curve fits for the load-stiffness relations for k_n and k_t , the total load-stiffness relation for the roller is:

$$k_z = \cos^2(\alpha) \left\{ 5.151 \cdot 10^9 \text{ N/m}^2 \ln \frac{P/L_{we}}{1.800 \cdot 10^3 \text{ N/m}} L_{we} \right\} + \sin^2(\alpha) \left\{ 8.157 \cdot 10^8 \text{ N/m}^{1.86} \ln \frac{P/L_{we}}{4.235 \cdot 10^3 \text{ N/m}} L_{we}^2 D_w^{-1.14} \right\} \quad (5.3)$$

5.5. Synopsis

The experiments presented in the chapter have shown to be an accurate and precise method for measuring the stiffness of roller-rail contacts at an angle of 45°.

- Experimental quality
 - Modal analysis experiments at 45° are less repeatable than experiments loaded normally. Nonetheless, the mean standard deviation of repeatability experiments is 1.028 % of the mean stiffness measured, as shown in Figure 5.3.1.
 - The repeatability of the setup is similar to the product variations within a roller batch, yet, no statistical significance is shown, see Subsection 5.3.2.
- Roller geometry
 - Roller orientation has a significant effect on the stiffness. A perpendicular orientation results in a 17 % lower mean stiffness, see Subsection 5.3.3.
 - A small influence on the roller length was observed.
 - The stiffness significantly decreases with roller diameter, the stiffness per contact length scales roughly with D_w^{-2} , see Subsection 5.3.5.
 - The effects of the number of rollers is comparable to the effect measured for the normal measurements, see subsection 5.3.7.
- Lubrication
 - In static conditions, there is no statistically significant change in stiffness by adding either oil or grease, see Table H.1.
- Roller material
 - Ceramic rollers are stiffer compared to steel rollers, as shown in Figure 5.14.
 - Stainless steel rollers show higher stiffness than steel rollers of the same length, which can be explained by the difference in material hardness. A lower hardness of the roller might result in better conformation in the contact, see Subsection 5.3.8.
- Tangential stiffness
 - Tangential components contribute to in the stiffness at 45°.
 - The variance of the tangential stiffness components is comparable to that of the normal measurements, see Table H.2.
 - The tangential stiffness scales with the contact length squared, see Figure 5.16c.
 - The tangential stiffness scales with roller diameter^{-1.14}, see Figure 5.16d.
- Modelling
 - A roller at 45° with parallel orientation may practically be modelled as a vector rotation of a normally loaded roller where both the normal and tangential stiffness are considered, see Figure 5.19.
 - Equation 5.2 predicts the tangential stiffness of a normally loaded and rough ($R_a=0.2\ \mu\text{m}$) roller-rail contact within 3 % for nearly all rollers measured, see Figure 5.17.
 - Equation 5.3 predicts the stiffness of a rough ($R_a=0.2\ \mu\text{m}$) roller-rail contact at 45° within 20 % for all rollers measured. This is simply the vector sum of the normal and tangential load-stiffness relations, see Figure 5.21.

6

Stiffness of a linear crossed roller bearing

Chapters 4 and 5 provided comprehensive insights into the load-stiffness relation of individual roller-rail contacts. Section 3.6 proposed an effective methodology in which individual contacts modelled as spring elements can be used to model complex assemblies. The method was effectively applied to the three foregoing test setups with a limited number of rollers. This Chapter applies the methodology developed to crossed roller slides, a common linear roller bearing assembly.

First, the crossed roller slide is described. Next, in Section 6.2 the setup for measuring slides is presented. Section 6.3 describes the development of a numerical and parametric MBD model to predict the stiffness of linear cross roller bearings. Finally, Section 6.4 verifies these MBD models by direct comparison with experimental results.

6.1. Description of the crossed roller slide

Figure 6.1 shows the geometry of the type of linear crossed roller bearing that is considered throughout this chapter. A crossed roller slide has a stiffness in 5-DOF; translation stiffness k_x and k_z along the x and z -axis respectively and rotational stiffness k_{θ_x} , k_{θ_y} , and k_{θ_z} around the x , y and z -axis respectively.

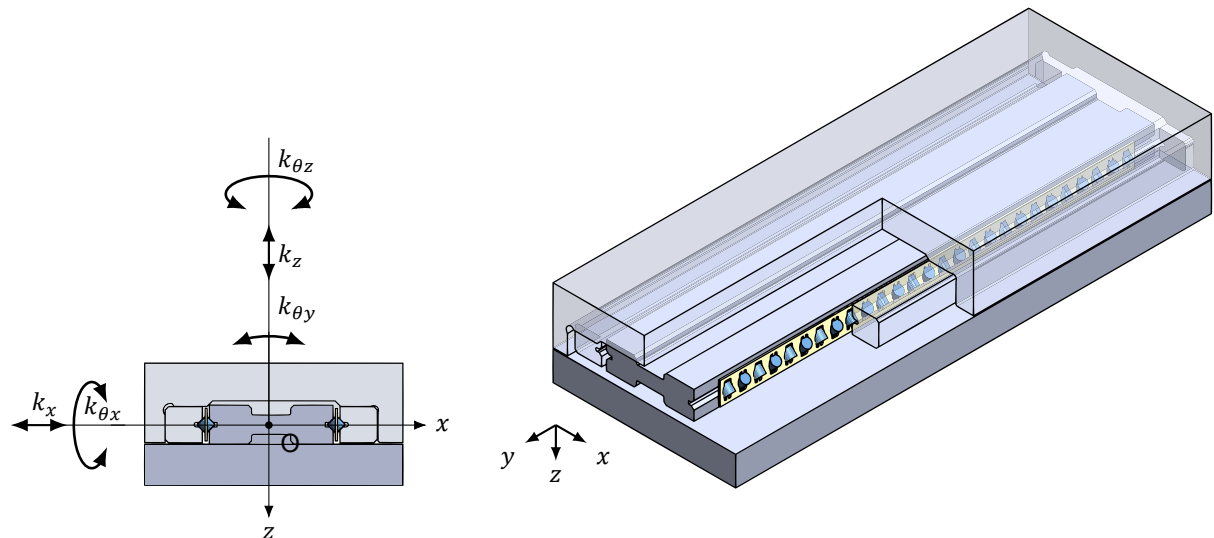


Figure 6.1: Schematic of a crossed roller slide.

One of the largest differences between individual rollers tested and crossed roller slides is the definition of contact length. For individual rollers the contact length is determined by the roller profile while for crossed roller slides the contact length is limited by the rail. It has to be verified whether the experimental results on individual rollers are suitable for the current situation as here the rail is smaller than the roller.

Another caveat of modelling this type of bearing is shown in Figure 6.2, the rails are not directly opposed to each other leading to a partial overlap of the projected rail lengths. This results in a non-uniform load distribution on the roller and misalignment.

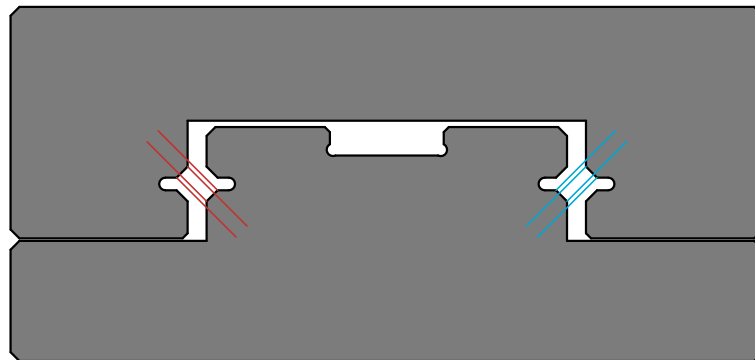


Figure 6.2: Depiction of projected rail length in crossed roller bearing.

In addition, crossed roller slides introduce the arbitrary presence of preload. As in described Section 2.6, crossed roller slides are usually preloaded with set screws. Earlier investigations into the exact relationship between set screw torque and resulting guide rail preload have been conducted. No accurate predictions of the relation between set screw torque and the resulting axial preload could be found.

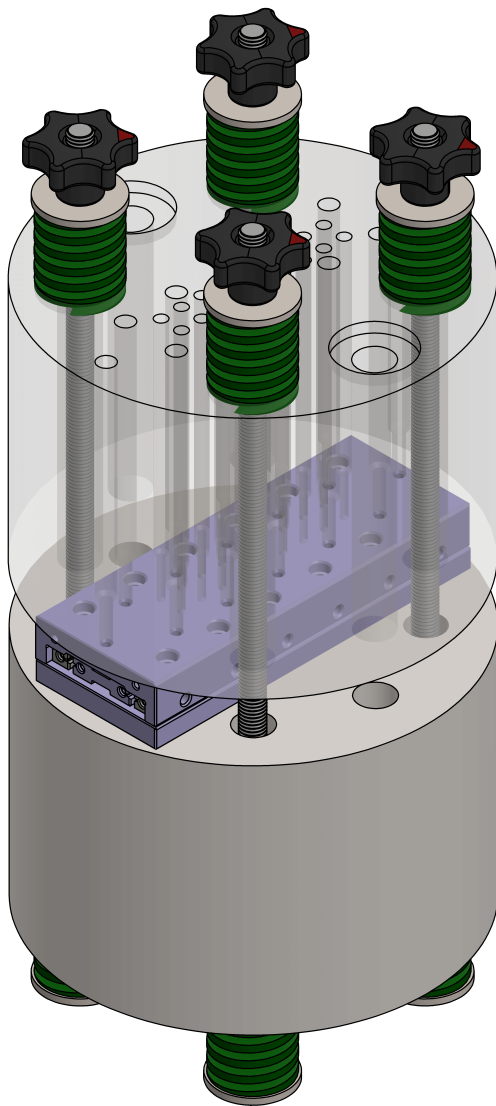


Video

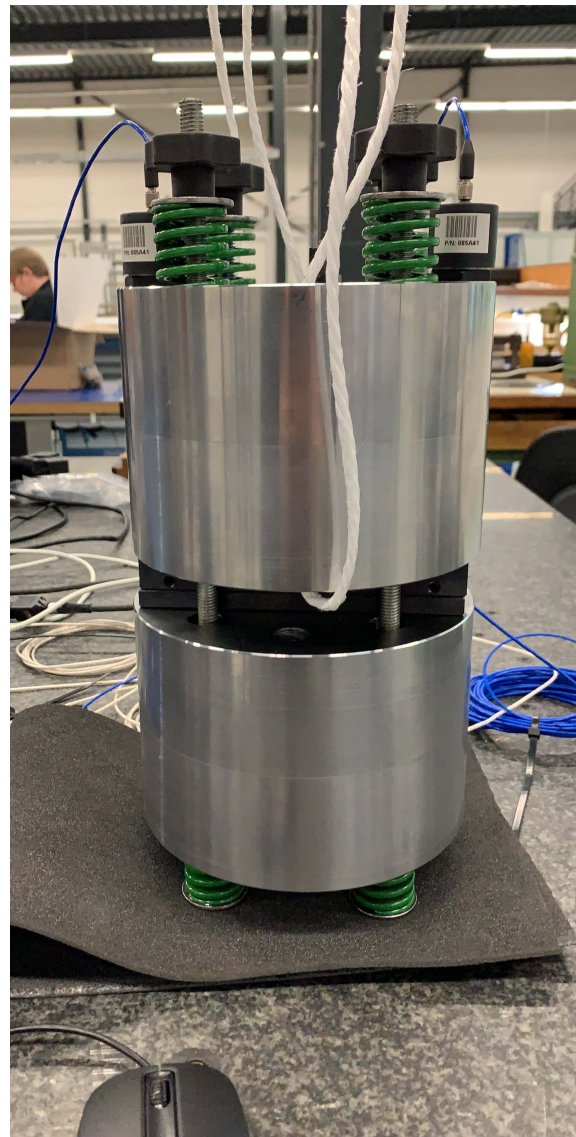
6.2. Test setup

Figure 6.3 shows the new test setup designed to perform the experiments on slides. The working principle of this setup is identical to that of the experiments in Chapters 4 and 5, except that a slide is bolted between the masses instead of rails.

Two crossed roller slides are used in these experiments, PM Bearings RT-3150 and RT-15100. A slide holds a large number of load-carrying rollers, making them considerably stiffer compared to the three or two rollers presented in Chapter 4 and 5 respectively. Larger masses are used to make sure the eigenfrequencies are in the correct range for the measurement equipment. To start with, simple calculations are performed to find a suitable geometry such that the inertia's ensure that the z -mode is well separated from the other modes. The dimensions and inertia's of the masses used in this Chapter, are given in appendix I. The stiffness measured is a combination of the stiffness of the table and the rolling contacts. The slides are mounted using 12 bolts to the top mass, 4 bolts connect the slide to the bottom mass.



(a) CAD model of test setup for measuring crossed roller slides



(b) Picture of test setup for measuring crossed roller slides

Figure 6.3: (a) CAD model and (b) picture of the test setup used for the experiments in this section. Crossed roller slides are bolted between the two masses. When compressed, the green springs exert load on the rollers and rails. The frequency response is measured with accelerometers. The setup is isolated from the external world by a foam block (not in CAD).

6.2.1. Description of the setup

A schematic of the setup is shown in Figure 6.4. The setup is modelled as a suspended 3D two mass spring system, with a spring element with a stiffness in 5-DOF. The slide has no significant stiffness in y -direction as this is the direction in which movement is facilitated.

The accelerometers are positioned according to Figure 6.5.

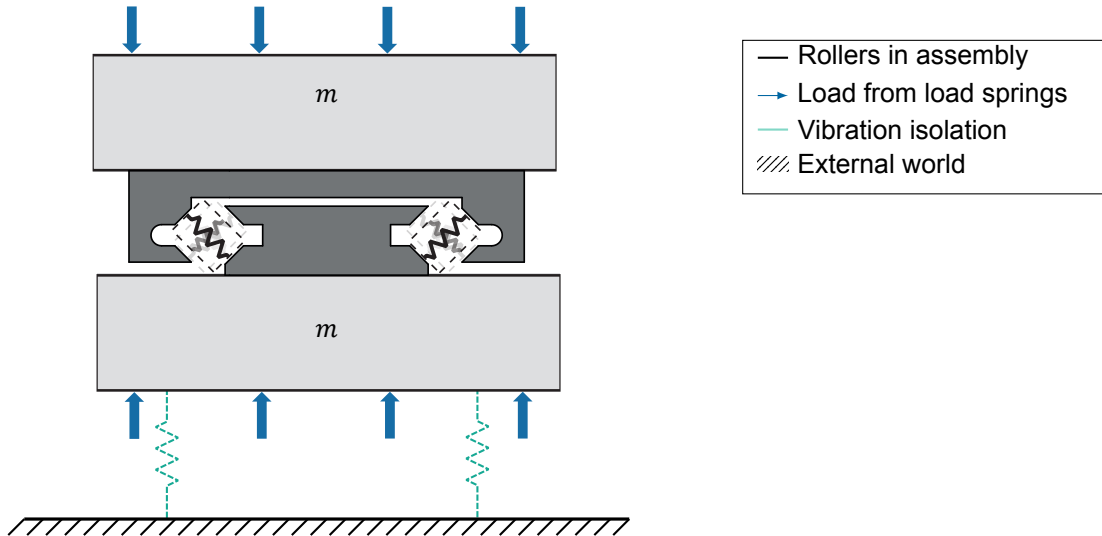


Figure 6.4: Schematic depiction of the setup including a slide.

6.2.2. Test procedure

The procedure is identical to the process described in Subsection 4.1.4. The load is increased up to 30% of the static load rating C_0 calculated for each configuration. The experiments are performed in an order of decreasing amount of rollers, such that the risk of severe plastic deformation during the assembly of the setup is minimized. All experiments are repeated three times.

6.2.3. Test equipment

The same equipment is used as for the experiments in Chapter 4. Two additional accelerometers are used, positions 5 and 6 in Figure 6.5; PCB Piezotronics model 393B05. An engine crane is used to mount the top mass on the slide in a safe and controlled manner.

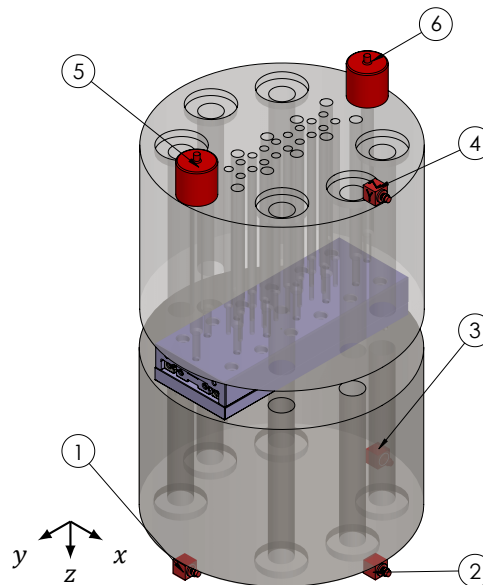


Figure 6.5: Accelerometer positions.



Video

6.3. Model

This Section describes the development of a multi body dynamics model. The goal of this model is to predict the eigenmodes and corresponding stiffness of the setup shown in Figure 6.3. Both a numeric and a parametric MBD model are developed.

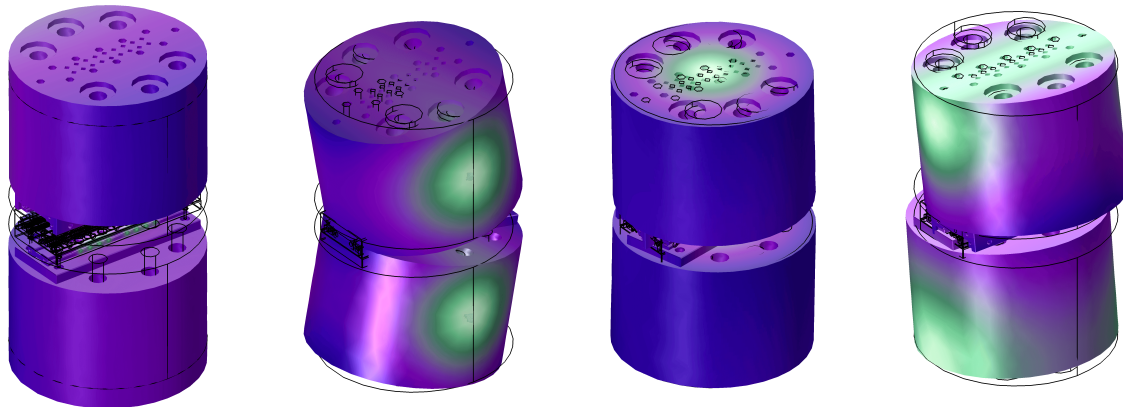
6.3.1. Numeric multi body dynamics model

A prestressed FEM eigenfrequency analysis has been performed using Comsol. The contacts are modelled as proposed in Section 3.6. Spring elements are placed between the rigid inlays. The stiffness of these elements is defined in Equation 5.3 with $\alpha = 0^\circ$ ¹. The load per roller is taken as specified in Equation D.1, divided by $\cos(45^\circ)$ and the number of load-carrying rollers Z_t .

All bolted connections are modelled as rigid connectors prescribed between the drill and threaded holes. A penalty contact is set between the mating assembly surfaces. A sweep is performed over all load and number of roller combinations investigated. For the RT-3150 slide this results in 74 sweep instances if the load is increased in steps of 360° . Even though hammer impact measurements are performed every 180° , it was only modelled for every full rotation to limit the computational load. For the RT-15100 slide a total of 33 unique load, number of roller combinations are evaluated. A spring foundation of 4000 N/m is added to the masses for stability, this is similar to the stiffness of the foam suspension of the setup and will confidently be neglected in further calculations.

Fillets of the slide bodies are removed to limit the number of small features and therefore lighten the computational load. The model is checked for mesh convergence. Additional analysis are performed with the non-simplified model to verify the validity of the simplifications. Table J.1 shows the results for the different models for slide RT-3150 with 16 rollers per cage, under 5 turns load. No serious deviation between the models is found.

Figure 6.6 shows the found relevant eigenmodes for the RT-3150 slide with 16 rollers per cage under 5 turns load. More flex modes of the masses exist at higher frequencies, they are not measured with the PAK system, hence these are not presented here. Eigenmode 1 (Figure 6.6a) is a pure translation in the z -direction. Eigenmode 2 (Figure 6.6b) corresponds with the pitch mode around the CoM of the two masses. Eigenmode 3 (Figure 6.6c) corresponds with the yaw mode round the origin of the slide. The stiffness-eigenfrequency relation is defined in Equation 6.1, all rotation axes go through the CoM.



(a) First eigenmode, z translation: 713 Hz (b) Second eigenmode, rotation around x -axis: 351 Hz (c) Third eigenmode, rotation around z -axis: 329 Hz (d) Fourth eigenmode, combination of rotation around y -axis and x translation: 1077 Hz

Figure 6.6: Four first eigenmode shapes for RT-3150 slide with 16 rollers per cage, under 5 turns load.

$$k_{\theta x} = (f_{\theta x} 2\pi)^2 \frac{I_x}{2}, \quad k_{\theta z} = (f_{\theta z} 2\pi)^2 \frac{I_z}{2}, \quad k_z = (f_z 2\pi)^2 \frac{m}{2} \quad (\text{with the inertia's from Table I.1}) \quad (6.1)$$

¹ α is set to 0° as it is orientated at 45° in the FEM model itself.

The stiffness of the slide body was found to almost linearly scale with the number of rollers. Consequently, the slide body can properly be modelled as an additional stiffness in series with the stiffness of the roller-rail contacts. This further substantiates the hypothesis that it is feasible to create a model for predicting the stiffness of a linear crossed roller bearing as a function of its design variables.

Incorporating $k_{b_{total}}$ as a stiffness in series with the roller-rail contacts, i.e. equation 6.3, creates a model that approaches the stiffness computed with the FEM model within a range of $\pm 3\%$ for all configurations, for both the RT-3150 and RT-15100 slide.

$$k_{b_{total}} = Z_t \cdot k_b \quad \text{where } k_b = 10^8 \text{ N/m} \quad (6.2)$$

$$k_{z_{slide}} = \frac{1}{1/(Z_t k_z) + 1/k_{b_{total}}} = Z_t (k_z + k_b) \quad \text{with } k_z \text{ from Equation 5.3 and } \alpha = 45^\circ \quad (6.3)$$

6.3.2. Parametric multi body dynamics model

This model extends the model of Liu et al. [58] by incorporating the compliance of the guide body and the dynamic effects of the rest of the bearing assembly. Symmetric eigenmodes in which the center of the system is stationary may be modelled as a mass spring system with only a single mass but twice the stiffness.

This allows the model to only consider the upper half of the setup, as shown in Figure 6.7. In this model the inertia of the rollers is neglected as it is insignificant compared to the rest of the setup. The load is assumed to exceed the preload such that only half the rollers are contributing to the system stiffness, the non contributing rollers are neglected. The bearing is dominantly loaded in z -direction.

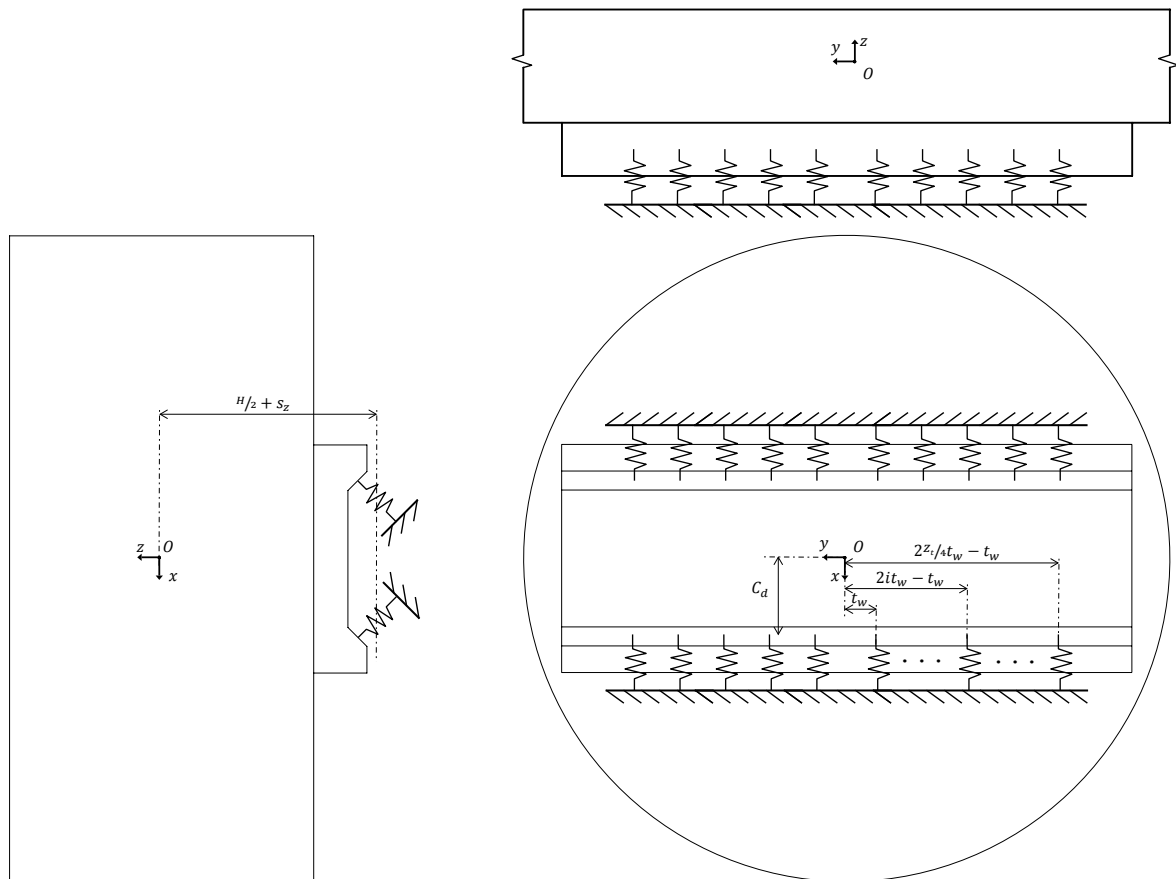


Figure 6.7: The simplified physical model of the upper half of the setup.

The system has Z_t load carrying rollers placed in the guide, the stiffness of each stiffness elements representing these individual roller is denoted with K_z and is assumed to have a stiffness as specified in Equation 5.3.

Because the stiffness of the slide body ($k_{b_{total}}$) is properly modelled as an additional stiffness in series and it scales almost linear with the number of rollers, it can also be modelled as Z_t individual spring elements in series with a spring element of stiffness k_s as in Equation 6.2. This allows for the introduction of an equivalent stiffness k' :

$$k' = \frac{1}{1/k_z + 1/k_b} \quad (6.4)$$

The simplified physical model with k' is shown in Figure 6.7, the origin of the Cartesian coordinate system (O_{xyz}) is placed in the CoM.

The equations of motion for the multi-DOF problem are obtained through the Lagrange method. The generalized coordinates are:

$$\vec{q} = [x \quad y \quad z \quad \theta_x \quad \theta_y \quad \theta_z]^T \quad (6.5)$$

The Lagrange Equation 6.6 includes kinetic energy T , potential energy V and non-conservative forces $Q_{noncons}$. The non-conservative forces are zero as damping is neglected.

$$\frac{d}{dt} \left(\frac{\partial T}{\partial \dot{q}_i} \right) - \frac{\partial T}{\partial q_i} + \frac{\partial V}{\partial q_i} = Q_{noncons} \quad (i = 1, 2, \dots, 6) \quad (6.6)$$

With kinetic energy T :

$$T = \frac{1}{2} (m\dot{x}^2 + m\dot{y}^2 + m\dot{z}^2 + I_x \dot{\theta}_x^2 + I_y \dot{\theta}_y^2 + I_z \dot{\theta}_z^2) \quad (6.7)$$

And potential energy V :

$$V = \frac{1}{2} k' \left(\sum_{i=1}^{Z_t} \Delta x_i^2 + \sum_{i=1}^{Z_t} \Delta z_i^2 \right) \quad (6.8)$$

Where x_i and z_i represent the spring deformation in the x -direction and in z -direction respectively.

The inertia forces are derived from Equation 6.7:

$$\begin{cases} \frac{d}{dt} \left(\frac{\partial T}{\partial \dot{x}} \right) = m\ddot{x} \\ \frac{d}{dt} \left(\frac{\partial T}{\partial \dot{y}} \right) = m\ddot{y} \\ \frac{d}{dt} \left(\frac{\partial T}{\partial \dot{z}} \right) = m\ddot{z} \\ \frac{d}{dt} \left(\frac{\partial T}{\partial \dot{\theta}_x} \right) = I_x \ddot{\theta}_x \\ \frac{d}{dt} \left(\frac{\partial T}{\partial \dot{\theta}_y} \right) = I_y \ddot{\theta}_y \\ \frac{d}{dt} \left(\frac{\partial T}{\partial \dot{\theta}_z} \right) = I_z \ddot{\theta}_z \end{cases} \quad (6.9)$$

The elastic forces are derived from Equation 6.8:

$$\left\{ \begin{array}{l} \frac{\partial V}{\partial x} = Z_t k' x + Z_t k' d \theta_y \\ \frac{\partial V}{\partial y} = 0 \\ \frac{\partial V}{\partial z} = Z_t k' z \\ \frac{\partial V}{\partial \theta_x} = \begin{cases} 4 \left(\sum_{i=1}^{z_t/4} (2it_w - t_w)^2 \right) k' \theta_x, & \text{if } \text{mod}(Z_t, 4) = 0 \\ 4 \left(\sum_{i=1}^{(z_t-2)/4} (2it_w)^2 \right) k' \theta_x, & \text{otherwise} \end{cases} \\ \frac{\partial V}{\partial \theta_y} = Z_t k' dx + Z_t k' (a^2 + d^2) \theta_y \\ \frac{\partial V}{\partial \theta_z} = \begin{cases} 4 \left(\sum_{i=1}^{z_t/4} (2it_w - t_w)^2 \right) k' \theta_z, & \text{if } \text{mod}(Z_t, 4) = 0 \\ 4 \left(\sum_{i=1}^{(z_t-2)/4} (2it_w)^2 \right) k' \theta_z, & \text{otherwise} \end{cases} \end{array} \right\} = \begin{array}{l} \\ \\ \\ \frac{t_w^2}{12} Z_t (Z_t^2 - 4) k' \theta_x \\ \\ \frac{t_w^2}{12} Z_t (Z_t^2 - 4) k' \theta_z \end{array} \quad (6.10)$$

Substituting Equation 6.9 and 6.10 in Equation 6.6 gives the equations of motion:

$$\left\{ \begin{array}{l} m\ddot{x} + Z_t k' x + Z_t k' d \theta_y \\ m\ddot{y} \\ m\ddot{z} + Z_t k' z \\ I_x \ddot{\theta}_x + \frac{t_w^2}{12} Z_t (Z_t^2 - 4) k' \theta_x \\ I_y \ddot{\theta}_y + Z_t k' dx + Z_t k' (a^2 + d^2) \theta_y \\ I_z \ddot{\theta}_z + \frac{t_w^2}{12} Z_t (Z_t^2 - 4) k' \theta_z \end{array} \right\} = \begin{array}{l} 0 \\ 0 \\ 0 \\ 0 \\ 0 \\ 0 \end{array} \quad (6.11)$$

The stiffness matrix \mathbf{K} can be obtained from Equation 6.11:

$$\mathbf{K} = k' Z_t \begin{bmatrix} 1 & 0 & 0 & 0 & d & 0 \\ 0 & 0 & 0 & 0 & 0 & 0 \\ 0 & 0 & 1 & 0 & 0 & 0 \\ 0 & 0 & 0 & \frac{t_w^2}{12} (Z_t^2 - 4) & 0 & 0 \\ d & 0 & 0 & 0 & (a^2 + d^2) & 0 \\ 0 & 0 & 0 & 0 & 0 & \frac{t_w^2}{12} (Z_t^2 - 4) \end{bmatrix} \quad (6.12)$$

The stiffness matrix \mathbf{K} , shows how the modes of translation along the y -axis and rotation around the x -axis cannot be expressed by independent differential equations, this is also the case for the setup used by Liu et al. [58].

6.4. Test results and discussion

This section presents the results of a load sweep experiment on a RT-3150 slide with a variable number of rollers in non-rolling conditions. These experimental results are compared to the parametric MBD model. Subsequently, the versatility of this modelling method is evaluated by applying this model to a RT-15100 slide. Lastly the influence of the roller orientation is tested by replacing half of the rollers with plastic balls.

All experiments are repeated three times, figures present the mean values of the repeated experiments. Table K.1 presents the descriptive statistics of the measurements. The graphs present a wide stiffness range, for clarity the error between the FEM model and measurements is presented in Appendix J.

6.4.1. RT-3150, stiffness in z-direction

Figure 6.8 presents the measured load-stiffness relationship in z-direction for a RT-3150 slide. The stiffness measurements are performed for $Z_t = 4, 6, 8, 10, 12, 14, 16, 20,$ and 26 .

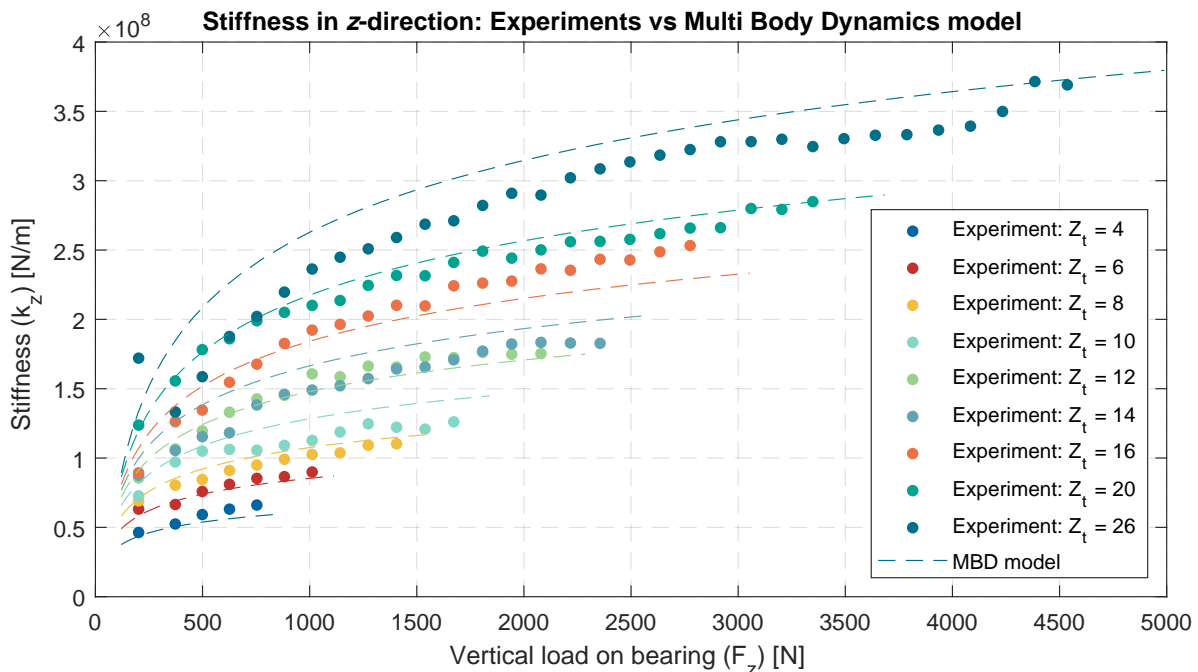


Figure 6.8: Hammer impact data: Experiments vs parametric MBD model of RT-3150 crossed-roller slide, stiffness in z-direction.

First of all, the method demonstrates to be greatly repeatable, the mean standard deviation k_z is 3.1 % of the mean stiffness measured. Comparing the measurements to the MBD model, it was found that the mean absolute difference between model and measurements is 8.1 %.

The max discrepancy is measured at the lowest loads, with $Z_t = 26$. It is likely that due to the high number of rollers, not all rollers in the other orientation will be fully out of contact for these low loads. This results in a stiffness increase of 30 % and this effect disappears when the load is increased. For higher loads, the model predicts the measured stiffness well within 20 %. The mean absolute difference between model and measurements is 8.1 %. Figure K.3 shows no noteworthy relation between the error and the number of rollers. The influence of geometric errors, such as the variance in roller diameter and limited straightness of the guide rails, does not appear to influence the stiffness of the guide noticeably.

6.4.2. RT-3150, stiffness in other directions

Figure 6.9 depicts the transfer function of accelerometer 2 for RT-3150 slide with 16 rollers per cage, under 5 turns load. This corresponds with the eigenmodes depicted in Figure 6.6.

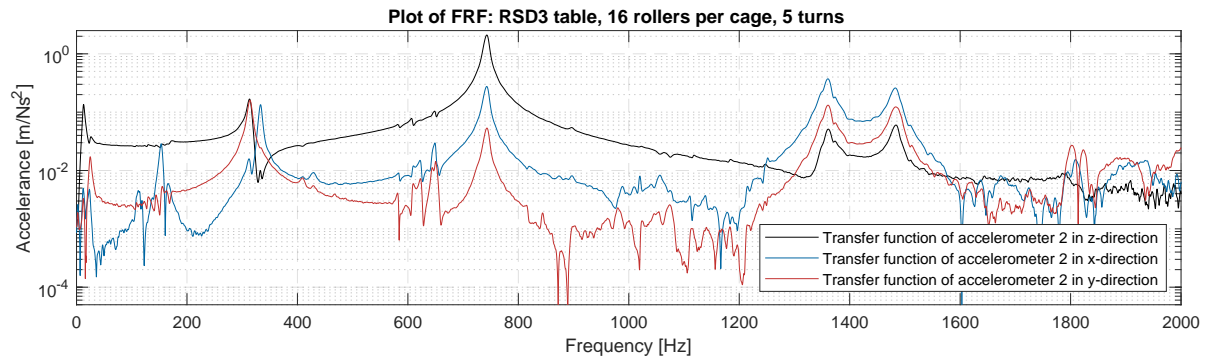
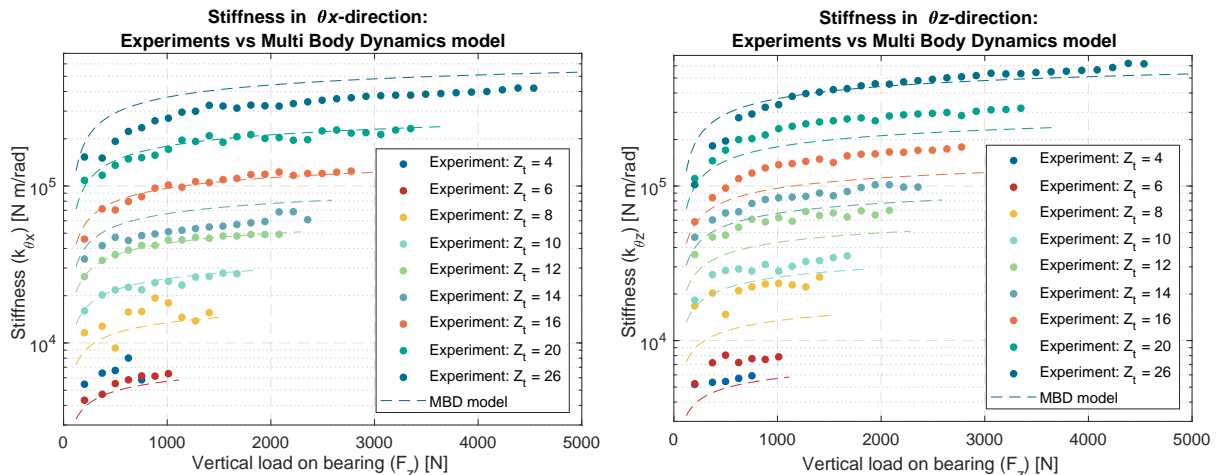


Figure 6.9: Hammer impact data: Transfer function for the RT-3150 slide with 16 rollers per cage, under 5 turns load; Transfer function of accelerometer 2.

The peak of the first eigenmode of z translation is measured at 743 Hz. The second eigenmode, rotation around x -axis, at 314 Hz. At 333 Hz, the third eigenmode is measured, rotation around y -axis. The measurement of the fourth eigenmode, measured at 1361 Hz, is less distinctive.

Extending the comparison between model and measurement to the stiffness in both θ_x and θ_z -direction results in load-stiffness relation shown in Figure 6.10a and 6.10b respectively.



(a) θ_x -direction.

(b) θ_z -direction.

Figure 6.10: Hammer impact data: Experiments vs parametric MBD model of RT-3150 crossed-roller slide, stiffness in θ_x and θ_z -direction.

Again, the MBD model falls within a 20 % range for predicting the load-stiffness relation. See Appendix J for plots explicitly presenting the errors. All hammer impacts are applied to the center of the top mass in negative z -direction. As a result the other modes are not directly excited, which makes the corresponding peaks for some measurements less distinctive in the FRF. This results in outliers due to selecting the wrong peak. Even when including these outliers, the average absolute difference between model and measurements is 17.3 % and 19.900 % for the θ_x and θ_z -direction respectively.

The combined angular stiffness of the loading springs is roughly $6.500 \cdot 10^3$ N m/rad. This is stiffer than the table stiffness expected by the MBD for $Z_t = 4$ and 6. The loading springs thus influence the measured eigenmode in θ_x -direction. For $Z_t = 4$, the load rating in the moment directions is low, to prevent overloading the bearing during assembly, the rollers are placed further apart (additional cage pocket left empty). This is, as expected, also observed in the stiffness measured in the θ_x and θ_z -direction.

6.4.3. RT-15100, stiffness in z-direction

Experiments are performed with the RT-15100 slide to test the versatility of this MBD model to variations of geometry and dimensions.

Figure 6.11 shows the measured load-stiffness relationship compared to the model for $Z_t = 8, 10, 12, 14, 16, 20,$ and 28 .

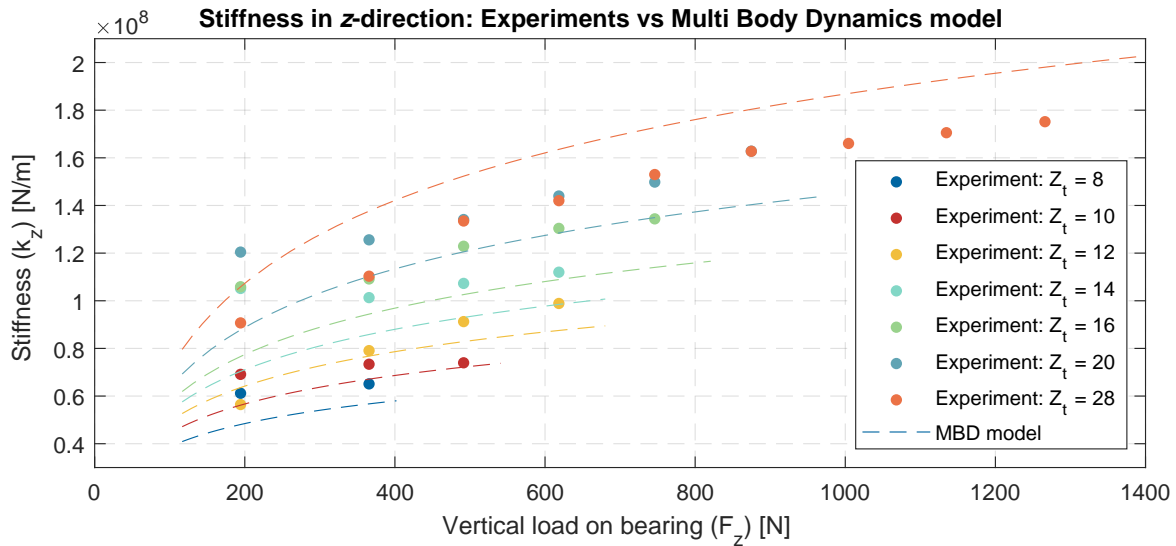


Figure 6.11: Hammer impact data: Experiments vs parametric MBD model of RT-15100 crossed-roller slide, stiffness in z-direction.

The model is correct within a 20% range for all measurements with an applied load. For low loads the measured stiffness is stiffer than what is predicted by the MBD model. This is in line with the measurements on individual rollers as shown in Subsection 5.4.3. Here, for roller type 2, also a stiffness above the fit was measured at low loads.

6.4.4. RT-3150, rollers in tension

Additional experiments are conducted to investigate if rollers in tension in any form affect the stiffness of the slide. In these experiments only in the compression loaded direction are placed in the setup, the rollers in the other direction are replaced by POM balls.

Figure 6.12 shows the load-stiffness relationship compared to measurements from Figure 6.8.

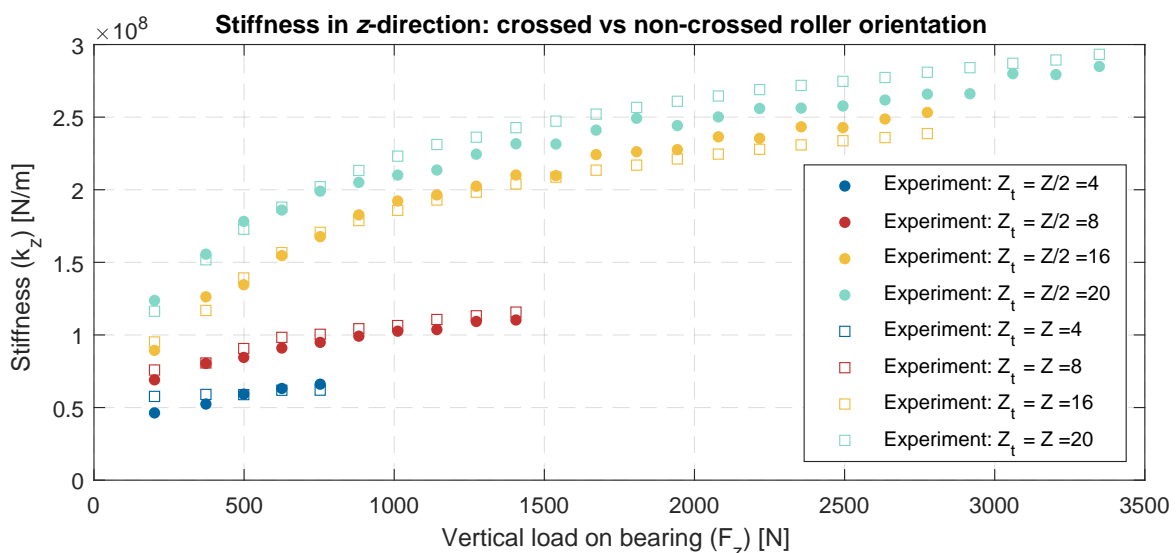


Figure 6.12: Hammer impact data: Experiments with RT-3150 crossed-roller slide, roller orientation, stiffness in z-direction.

There is no constant difference between the two configurations. Thus, solely the number of load-carrying rollers per guide contributes to the calculation of the stiffness. Rollers loaded in tension do not contribute to the stiffness of the guide.

6.5. Synopsis

The setup demonstrates to be greatly repeatable, the mean standard deviation of k_z is 3.1 % of the mean stiffness measured.

- The parametric MBD predicts k_z well within 20 % for the RT-3150 slide. The mean absolute difference between the MBD FEM model and the measurements is 8.1 % for $Z_t = 4, 6, 8, 10, 12, 14, 16, 20, \text{ and } 26$
- The parametric MBD gives an accurate prediction of k_{θ_x} for the RT-3150 slide. The mean absolute difference between the MBD FEM model and the measurements is 17.3 % without removing outliers.
- The parametric MBD gives an accurate prediction of k_{θ_z} for the RT-3150 slide. The mean absolute difference between the MBD FEM model and the measurements is 19.9 % without removing outliers.
- All hammer impacts are applied at the center of the top mass in negative z -direction, yielding less distinctive modes in other directions. As a consequence some of the peak frequencies are falsely identified during the data analysis. This results in outliers in the measured stiffness, especially for a low number of rollers.
- The parametric MBD has shown to be versatile. Applying the model to a slide with different dimensions, a RT-15100 slide, shows correct prediction of k_z within a 20 % range for all measurements with an applied load.
- Rollers loaded in tension do not contribute to the stiffness of the guide.
- The influence of geometric errors, such as the variance in roller diameter and limited straightness of the guide rails, appear not to influence the stiffness of the guide noticeably.

Conclusions and recommendations

7.1. Conclusions

The goal of this research was stated in Section 1.3 as:

To create and validate a model for predicting the static stiffness of a linear crossed roller bearing as a function of its key design variables within a range of 20 %.

A six degree-of-freedom parametric MBD model of the cross roller guide is presented. In this model, the stiffness of the crossed roller guide is specified by the stiffness matrix \mathbf{K} . The stiffness matrix \mathbf{K} is constructed based on a fitted load-stiffness relation obtained through measurements on individual rollers and a FEM model considering the compliance of the slide body. Experimental results verify the parametric MBD model. The model predicts the stiffness within 20 % for all slides, number of rollers, applied loads, and directions measured.

The stiffness of a linear crossed roller bearing depends on many factors of which some cannot be measured directly when measuring an entire assembly. Therefore, a step-by-step approach was taken to build a model, as shown in Figure 7.1.

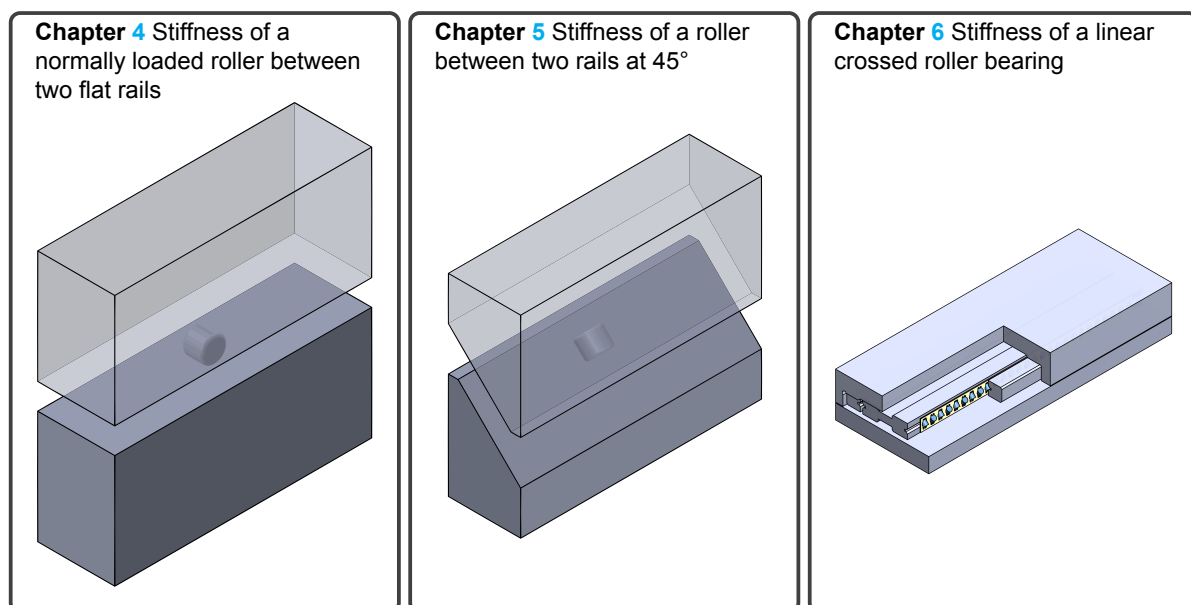


Figure 7.1: Step-by-step model development process to describe the stiffness of a crossed roller bearing.

In the process of working towards the goal of answering this question, multiple other conclusions are drawn with respect to:

Stiffness of a normally loaded roller between two flat rails

- Modal analysis experiments are an accurate and repeatable method for measuring the stiffness of roller-rail contacts, especially at higher loads; variations smaller than 1 % were measured.
- Stiffness calculated using the capacitive probe shows the same load-stiffness relation as modal analysis experiments but with a lower precision.
- The Tripp model is an upper limit for measurements on real rollers with tolerances.
- Equation 4.2 predicts the stiffness of a rough ($R_a=0.2\ \mu\text{m}$) roller-rail contact within 10 % for all rollers measured¹.
- Roller-to-roller variations have a small but statistically significant effect on the stiffness, about 1 %.
- In static conditions, the influence of adding either oil or grease is not statistically significant at all.
- Experiments performed suggested an influence of the material hardness on the stiffness in rough roller-rail contacts, a lower hardness of the roller might result in better conformation in the contact.
- The stiffness increases with a smoother surface, the magnitude of the influence of the surface finish change on the stiffness is in line with what is expected from the theory of Greenwood. At a load of 10 % of C_0 , a typical preload in linear bearing assemblies, a decrease in surface roughness from $R_a=0.2\ \mu\text{m}$ to $R_a=0.0\ \mu\text{m}$, results in a stiffness increase between 6–8 % 6% and 8%.
- A smoother surface results in a lower stiffness variance, especially for low loading conditions.
- Equation 4.3 predicts the stiffness of a smooth ($R_a=0.03\ \mu\text{m}$) roller-rail contact within 10 % for all rollers measured.²
- The roller-rail stiffness appears not to be dependent on the roller diameter, however no concrete conclusions can be drawn as the roller diameter was not varied independent of roller length.
- Longer rollers of the same diameter might have a lower stiffness per contact length, this could be caused by end-effects or the limited straightness of rollers and rails. This view might be distorted due to the low roller quality of the longest roller, or this could be a non-linearity in the setup.

Stiffness of a roller between two rails at 45°

- A roller at 45° with parallel orientation may practically be modelled as a vector rotation of a normally loaded roller where both the normal and tangential stiffness are considered.
- Equation 5.3 predicts the stiffness of a rough ($R_a=0.2\ \mu\text{m}$) roller-rail contact within 20 % for all rollers measured. This is simply the vector sum of the normal and tangential load-stiffness relations.
- Roller orientation has a significant effect on the stiffness at 45°, a perpendicular orientation resulted in a 17 % lower mean stiffness.
- The tangential stiffness scales approximately with the contact length squared.
- The tangential stiffness scales roughly with the roller diameter^{-1.14}.

¹one outlier, the largest rollers of type 12

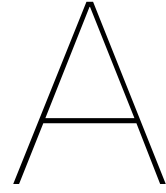
²one outlier, the lower quality rollers of type 6

Stiffness of a linear crossed roller bearing

- The added compliance of the slide body scales nearly linear with the number of rollers.
- The slide is adequately modelled as the stiffness of the rolling elements and the body in series.
- Rollers loaded in tension do not contribute to the stiffness of the guide and may be neglected in the analysis, as long as the load exceeds the preload applied.
- The influence of geometric errors, such as the variance in roller diameter and limited straightness of the guide rails, does not appear to influence the stiffness of the guide noticeably.

7.2. Recommendations

- The scope of this study is limited to static conditions. The work of Soleimanian et al. [46] showed only a marginal effect of EHL on the load-stiffness relation. Based on the findings in this Thesis a decrease in stiffness equivalent to tangential stiffness component would be expected. Therefore, the dynamics of crossed roller bearings at a velocity should be investigated in future studies such that the effects of EHL and spin creepage can be investigated.
- Currently, one of the biggest uncertainties is the preload applied using preload screws. An accurate preloading method should be developed to accurately preload a crossed roller bearing. This would allow the experiments to be performed with all rollers in contact and with small external loads. This could be done by adding a plastic tip, for which the yield limit is known, to the set screws. Another approach would be a spring loaded preload mechanism such as developed by Julian Dekker [70].
- There is a high demand for well documented empiric load-stiffness relations for rolling element contacts under various conditions. With the methodology presented in this Thesis, the presented data-set can be expended with relatively little effort. It would be very relevant to test different roller profiles, sizes, materials and especially qualities.
- This Thesis does not make an effort at analytically solving the problem of a tangentially loaded roller. Johnson [13] describes traction loading of a half-space. If this would be combined with the shear deformation in the bulk of the roller, as covered by Harris et al., an analytic solution for the tangential stiffness could be derived. This solution could then be verified with the empiric relation presented in this Thesis.
- Experiments suggested an influence of the material hardness on the stiffness. Current models do not incorporate material hardness. It would be relevant to further investigate this finding by performing experiments on rollers which went through different tempering processes, such that different hardness levels can be tested. This could be suitable for a bachelor research project.



Specification of rolling elements

This Appendix presents the parameters of the rollers used throughout this Thesis.

Table A.1 list all parameter specified by the manufacturers. L_{we} is measured, see Table A.2

Table A.1: Parameters of the rolling elements used in the experiments.

Type	D	L_{we}	L_r (mm)	E (GPa)	ν (-)	Material	Hardness min (HRC)
1	3.00	1.793	2.20	210	0.29	Bearing steel (1.3505)	60
2	1.50	1.104	1.40	210	0.29	Bearing steel (1.3505)	60
3	6.00	3.805	4.40	210	0.29	Bearing steel (1.3505)	60
4	9.00	8.309	8.80	210	0.29	Bearing steel (1.3505)	60
5	3.00	2.569	2.80	210	0.29	Bearing steel (1.3505)	60
6	3.00	3.734	4.00	210	0.29	Bearing steel (1.3505)	60
7	3.00	1.947	2.00	210	0.29	Bearing steel (1.3505)	60
8	3.00	2.756	2.80	300	0.26	Silicon nitride (Si_3N_4)	90
9	3.00	1.804	2.20	200	0.28	Stainless steel (1.4034)	54
10	3.00		Ball	210	0.29	Bearing steel (1.3505)	60
11	6.00		Ball	210	0.29	Bearing steel (1.3505)	60
12	9.00		Ball	210	0.29	Bearing steel (1.3505)	60
13	3.00	1.232	2.20	210	0.29	Bearing steel (1.3505)	60
14	1.50	0.682	1.40	210	0.29	Bearing steel (1.3505)	60

Table A.2 list all measured geometric parameter. The measurement equipment is described in D.

Table A.2: Measurements on the rolling elements used in the experiments. Means and standard deviation based on measurements on three rollers

Type	Contact length		Surface roughness, Ra		Cylindricity		Circularity		Profile end
	μ (mm)	SD (μm)	μ (μm)	SD (μm)	μ (μm)	SD (μm)	μ (μm)	SD (μm)	
1 ^a	1.793	12	0.028	0.006	0.727	0.006	0.383	0.136	Fillet
2	1.104	8	-	-	-	-	-	-	Chamfer
3	3.805	60	0.031	0.007	0.423	0.163	0.222	0.068	Fillet
4	8.309	59	0.034	0.008	0.463	0.156	0.227	0.104	Fillet
5	2.569	7	-	-	-	-	-	-	Chamfer
6	3.738	21	0.080 ^b	-	3.467	0.917	2.212	0.667	Chamfer
7	1.947	7	-	-	-	-	-	-	Faced
8	2.756	22	-	-	-	-	-	-	Fillet
9	1.804	16	-	-	-	-	-	-	Fillet

^a Based on measurements on 6 rollers

^b Based on measurement on a single roller

B

Setup components

This Appendix contains a table with the components of the test setup described in Section 4.1.

Table B.1: Setup components.

Component	Description	Type	Standard	Material
1	Blind flange	DN150-PN16	DIN 2527	Stainless steel (1.4307)
2	Guideway rail, see Figure B.1	PM O-92025 x 100	-	Bearing steel (1.3505)
3	Threaded rod	M10 - 8.8	DIN 976	Steel, galvanized
4	Washer	11X34 (M10) 100 HV	ISO 7094	Steel, galvanized
5	Star knob nut	BK38.0048.04010	-	Polyamide, brass insert
6	Hexagon head screw	M8x40 - 12.9	ISO 4762	Steel, black oxide
7	Compression spring	FIBRO 241.14.32.038	ISO 10243	Steel 50CrV4

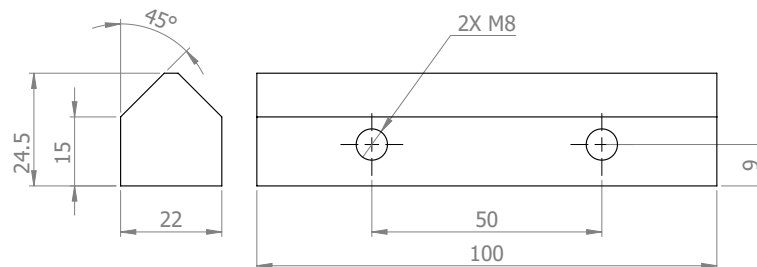
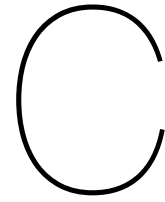


Figure B.1: Dimensions of the rails used in the experiments. PM Bearings O-92025 x 100. The rails are made out of bearing steel (1.3505).

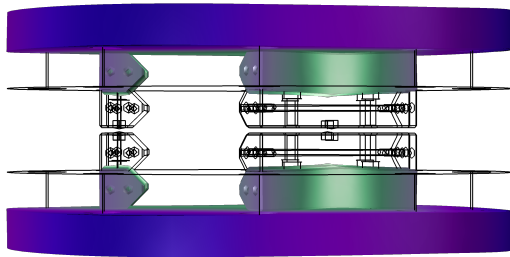


Multi body dynamics analysis of the normal test setup

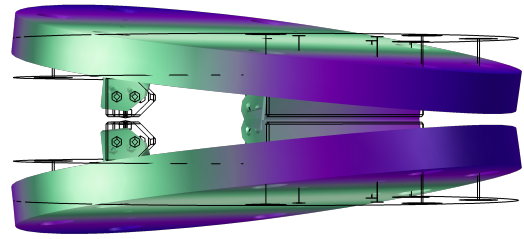
This Appendix describes the Multi body dynamics analysis, as used in Chapter 4. The goal of this model is to verify if the eigenmodes are distinguishable and to determine the stiffness of the setup itself.

A FEM multi body dynamics analysis has been performed using Comsol. The setup stiffness can be modelled as stiffness in series with the to be measured stiffness. Once the setup stiffness is determined, it can be compensated for when taking measurements. The contacts are modelled such as proposed in Section 3.6. Spring elements are placed between the rigid inlays. The stiffness of these elements is swept over range used during the experiments. All but the first eigenmode have identical but symmetric eigenmodes, these are not plotted. More flex modes of the disks do exist at higher frequencies, they are not measured with the PAK system, therefore they are not plotted.

The aspect of the model where assumptions have to be made is the connection between the disk and the rails. The rails are bolted onto the rails, this seems to be not significantly influenced by the torque applied, tests were performed to verify this, see Appendix D on verification. The bolt connections are of little interest in the analysis and may be assumed to have a negligible deformation. The bolts are replaced with virtual rigid bodies with appropriate boundary conditions, i.e. the drill and threaded hole are assumed to be perfectly rigid and are modelled using rigid connectors. A contact is set between the rail and flange, a situation with and without friction was modelled, no difference was found. Stress stiffening increases the setup stiffness by roughly 25 %.



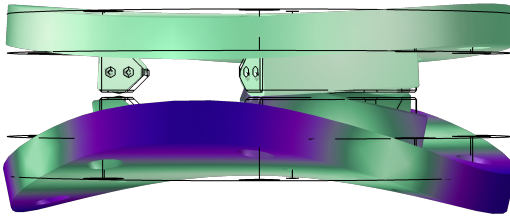
(a) First eigenmode, normal translation: 745 Hz



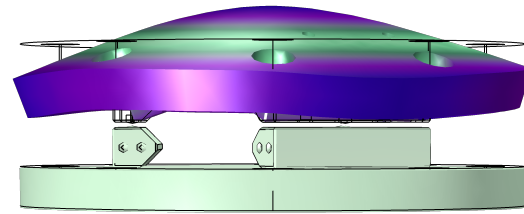
(b) Second eigenmode type, tilt: 581 Hz



Animation



(c) Third eigenmode type, flex mode: 1873 Hz



(d) Fourth eigenmode type, flex mode: 2728 Hz

Figure C.1: Plots for the different mode shapes. The stiffness per spring element is $4.65 \cdot 10^7$ N/m.

Figure C.1 shows the found mode shapes of the relevant eigenmodes for a stiffness set equal to what was measured for 4.5 turns load for roller type 1, the stiffness is shown in Figure 4.3, the corresponding transfer function is shown in Figure C.2.

It can be seen that the eigenfrequencies of model and measurement greatly correspond. The mode of with normal translation in the z -direction, shown in Subfigure C.1b, has a frequency of 745 Hz, in the shown transfer function the corresponding mode is measured at 748 Hz. The tilt mode has a frequency of 581 Hz in the FEM analysis, in the measured response these modes are centered around 584 Hz. The point symmetry of the setup warrants that the three tilt modes have the same eigenfrequency. The PAK software provides visualization of the excited eigenmodes, the modes have the mode shape as what is seen in the FEM model. The flexmodes could not be visualized fully as the number of sensors were limited.

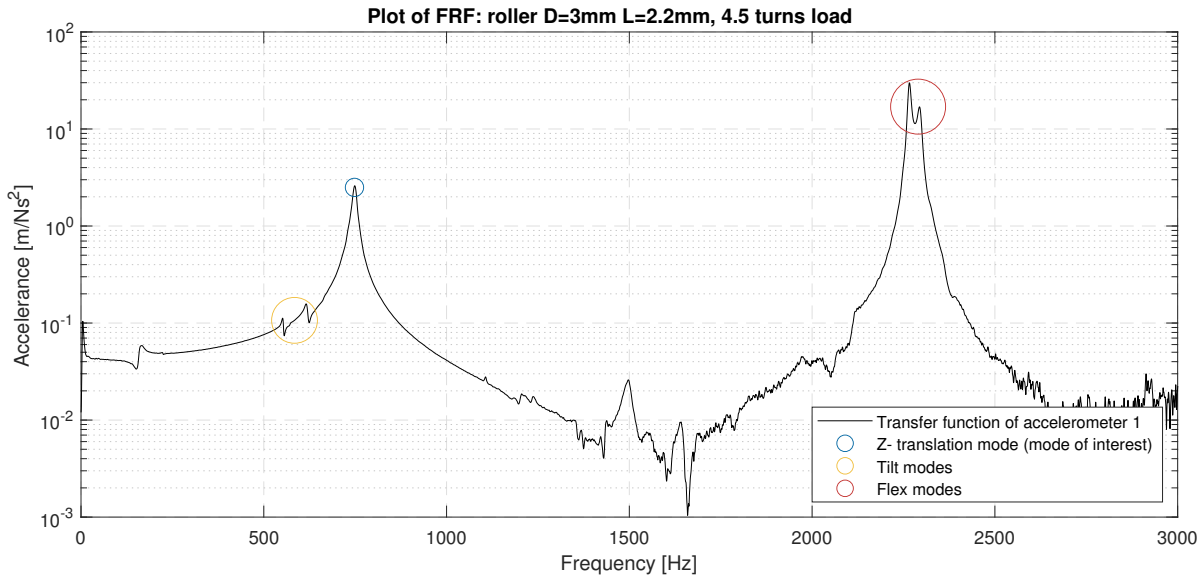


Figure C.2: Hammer impact data: Transfer function for rollers type 1, under 4.5 turns normal load; Example of a typical transfer function.

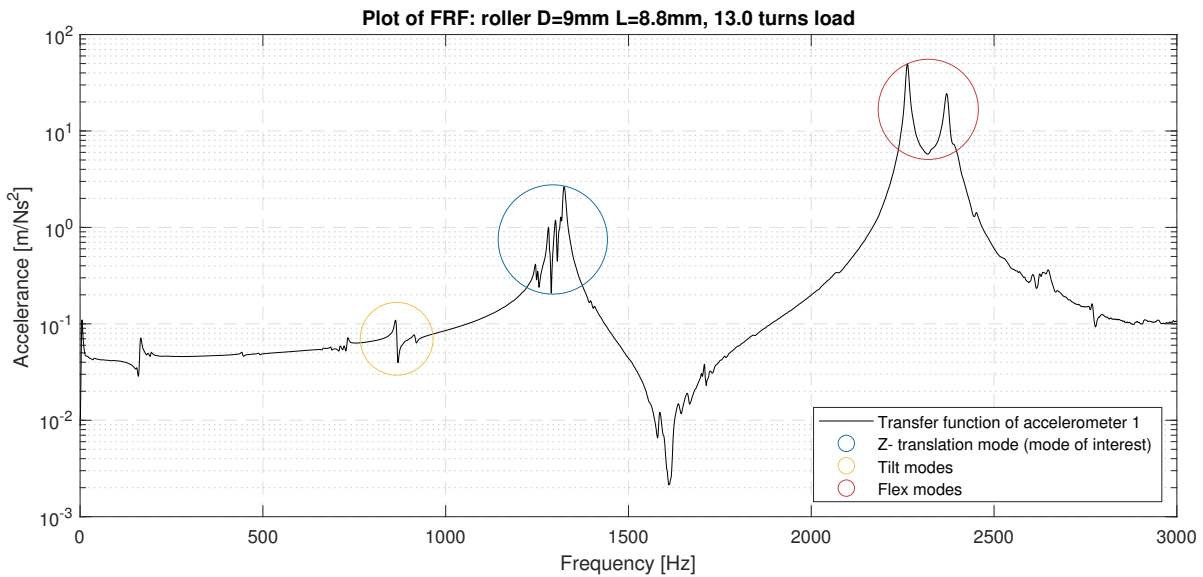
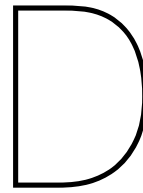


Figure C.3: Hammer impact data: Transfer function for rollers type 4, under 13.0 turns normal load; Example of a poor FRF.

In this FEM model the stiffness k is set and swept. When the final eigenfrequency of the eigenmodes is calculated, the deviation from a perfect mass spring system can be quantified, the stiffness of the setup can be extracted. When all the setup components are set to rigid, the system behaves as an ideal mass spring system, this is an obvious result but has been calculated as a test to make sure the model parameters are set correctly. The FEM model found that the setup is properly modelled as a compliance in series with the three rail sets, i.e. Equation C.1. The stiffness of the setup (K_{setup}) was found to be $1.450 \cdot 10^9$ N/m. With ω_0 found in the analysis and $3k$ actively set, k_{setup} can be determined. The damping is insignificant: $\omega_d = \omega_0$.

$$\omega_0 = \sqrt{\frac{2k_{total}}{m}} \quad (C.1)$$

$$\frac{1}{K_{total}} = \frac{1}{3k} + \frac{1}{K_{setup}}$$



Uncertainty and error analysis of the normal test setup

This Appendix contains an analysis of the uncertainty and error of the normal setup.

Uncertainty defines an interval about the measured values within which the true value is suspected to fall. Many actions are taken to minimize the uncertainty. Both systematic and random error are minimized. The random error is minimized by strictly following the same procedure for all measurements and by repetition, all measurements are repeated three times to spot outliers and quantify the variance.

Three approaches have been taken to estimate systematic error of the setup.

- Reference measurements were performed by loading the setup with steel balls, they form a reference stiffness as there is scientific consensus on their behaviour. See Subsection [4.2.2](#)
- Two independent measurement techniques and instruments are used to identify the stiffness, hammer impact measurements and displacement measurements.
- Each setup parameter is measured with more than one instrument, no single parameter was blindly taken from the data-sheet or modelling.

A considerable pitfall in this experiment is in incorrect setting in one of the many equipment configurations, this type of mistake will often remain undetected. A healthy dose of common sense and critical evaluation of (the order of magnitude) all interim results helped in tackling possible errors. Simple tests as playing a sound on a tone generator app with a smartphone and measuring the frequency response were one of simple ways to make sure all settings were correct.

It is important to point out that all measurements have been performed with, the same, new rails and rollers. Though no shift over time was measured, it is likely that some plastic flow did occur during the measurements.

Drift

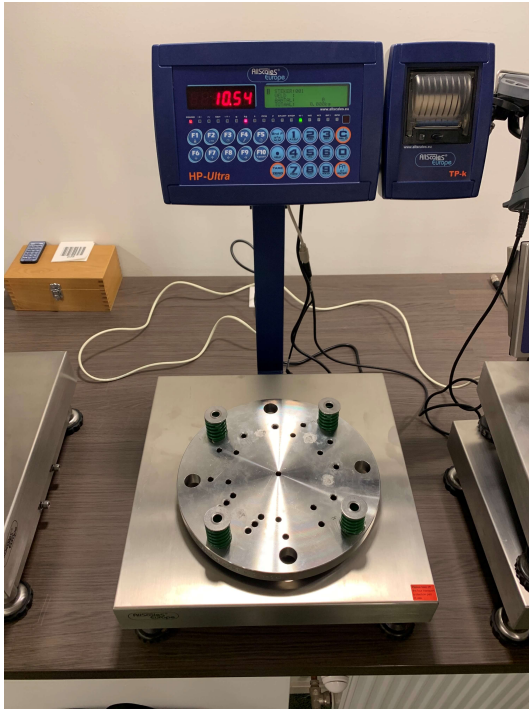
To identify whether the setup is subjected to drift, an additional measurement has been performed. The setup was loaded and halfway through a run the setup was left untouched for both 15 minutes and overnight. No drift in eigenfrequency was measured at the two time intervals.

Rail disk connection

All connections Ideally the setup is constructed out of two solid masses without any internal connections. At first it was attempted to place the rollers directly between the two masses, hardening the masses resulted in unsatisfactory hardness levels and could not be used for the experiments. The surface of both the rail and the mass are ground to ensure a conforming contact. The rails are bolted on to the mass with two M8-10.9 hex bolts and are tightened with 20 N m each. Measurements were performed with only half the tightening torque to assess its sensitivity to it, this did not influence the eigenmodes of the setup. Additional measurements were performed with only one bolt per rail, this did significantly influence the FRF.

Mass and weight of the setup

The mass of the setup has to be determined in order to calculate the stiffness of the contact. The weight of the setup has to be determined to specify the initial loading. The weight of all the components was specified in the design process, additional measurements were done to verify. The mass of the capacitive probe (12 g) and the four accelerometers (7 g each) is neglected. The load springs are only included for determining the weight, for the mass they are assumed to be of no influence because of their low stiffness. Initial measurements were performed on an Inventum WS308 kitchen scale. Finally all components were weighed with a calibrated, CE-063, approved scale at Henk Maas Weegschalen B.V..



(a) Upper disk.



(b) Die springs.

Figure D.1: Weighing the setup at Henk Maas Weegschalen B.V.

Stiffness of the load springs

The stiffness of the load springs is needed to determine the load on the rollers given the compression of the springs. The ISO 10243 die springs have an analytically specified stiffness. An Alluris FMI-250C2 high precision force gauge is used to measure the stiffness of the individual springs, however these do not allow for a measurement of the full range in which the springs are used. At Henk Maas Weegschalen B.V. a calibrated, CE-220, loadcell was placed between the two masses, the force number of turns compression relation was logged for 3 runs, the resulting mean values are used as the input for a definite relation second order polynomial relation. This also accounts for any sensitivity error (non linear error) of the load springs when a single stiffness parameter would be used. The rotation load relation is given in equation D.1, here n_{turns} are the number of turns the knob is compressed and F_{weight} the load caused by the weight of the upper mass in Newton. The maximum disparity between this fit and the measurements is 12 N, this is measured at a load of 900 N.



Figure D.2: Measurement of the spring force at Henk Maas Weegschalen B.V.

$$F = 1.763n_{turns}^2 + 249.35n_{turns} + 46.05 + F_{weight} \quad (D.1)$$

The stiffness of the load springs are parallel with the to be measured contact stiffness. Their stiffness is sufficiently low that it does not influence the eigenfrequency of the setup. To check this measurements with only two spring pairs instead of four were carried out, the same stiffness was measured. The stiffness of the load springs is accounted for in the final results for neatness.

Geometric measurements on the rollers

Though all the roller dimensions are specified in the drawings, they were also verified using measurements. The roundness and cylindricity are measured with a Mahr MarForm MMQ. The surface roughness in length direction, is also measured, see Table A.2.

Using a Nikon profile projector, the contact lengths of the rollers used have been measured at ART Tooling. From each roller type, two rollers were measured four times, twice diascopic and twice reflected.

Thermal drift

The measurements are performed in a room that is not temperature controlled. The temperature fluctuated throughout the measurements between 18 °C and 30 °C.

Zero order uncertainty

All instruments used have a resolution that us an order of magnitude smaller than needed for the experiments; the zero order uncertainty at no point dominantly limits the overall uncertainty.

Hysteresis error

All experiments were performed with an increasing load, such that any plastic deformation in the contact does not influence measurements at lower loads. This also keeps any hysteresis errors constant. An example of an other hysteresis error that is prevented is the torque produced in the load springs due to the tightening torque applied with the star knobs.

Zero shift error

The die springs are secured to the lower mass with epoxy glue, the threaded rods are glued to the springs such that the rods cannot spin while turning the star knobs. All knobs are labeled and have an arrow such that no mistakes are made in the measurement procedure. The point where the springs start to compress is very unequivocal, such that the zero shift error is limited.

When measuring the distance with the capacitive probe, absolute distance of little interest as only the displacement, change in distance, is used for calculating the stiffness.

Repeatability error

The absolute differences in stiffness between the three impacts of each load position in a single run are also studied. In case a difference is measured, one could assume that the measurement itself influences the stiffness, this was not measured. The impacts could lead to a plastic deformation in the contact, they could also cause slip in the contact such that the roughness profiles would make a new fit. The distance between the masses is measured after each impact, the average bandwidth between the impacts is 4.800 nm without removing any outliers, the maximum difference between two impacts was 37 nm, this was an initial impact.

The non-linearity of the measurement with regards to the impulse amplitude was also studied, two consecutive impacts with an amplitude of about 50 N and 200 N were studied, identical eigenfrequencies were measured. The damping ratio of the FRF is circa 0.01, this plays part in the linearity of the mass spring system and lets it act as a harmonic oscillator.

The continuously controllable variable of the load is discretized in steps of 180°, this is not exact, as it is set by hand. With the assumption that the 180° is met every time with an uncertainty of 20°, this is 11 % uncertainty for the load increase, while roughly $\frac{11}{\#turns+0.5}$ % for the absolute load itself. For the modal analysis, only the load is needed, while for the capacitive measurement, the load increase also is needed to perform a numerical differentiation. The uncertainty of the modal measurement is lower as a result, it also decreases with an increasing number of load turns.

The Lion Precision C8 capacitive sensor has a resolution of 10 nm at 100 Hz, in the experiments a RMS value from a 2.500 s sample is used.

The stiffness is calculated with the capacitive measurement using the following equation:

$$k = \frac{d_F}{d_u} = \frac{\Delta_F}{\Delta_s} = \frac{k_{springs} \quad lead \quad \frac{rotation}{360}}{s_{i+1} - s_i} \quad (D.2)$$

When only considering random errors, the overall uncertainty of the Load increase is:

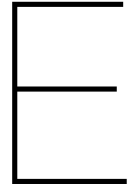
$$k_{springs} \quad lead \quad \frac{20^\circ}{180^\circ} = 15 \text{ N} \quad (D.3)$$

While the overall uncertainty of the distance is 10 nm.

Combining the root-sum-squares of the errors expanded around the first half turn with rollers of type 1 gives:

$$\begin{aligned} \Delta_s &\approx 4 \mu\text{m}, \quad \Delta F \approx 135 \text{ N} \\ u_{\Delta_s} &= \sqrt{u_{s_i}^2 + u_{s_{i+1}}^2} \approx 14.140 \text{ nm} \\ u_{\Delta F} &= 15 \text{ N} \\ u_{k,\Delta_s} &= \left(\frac{\partial k}{\partial \Delta_s}\right)_{\Delta_s=4 \mu\text{m}} \quad u_{\Delta_s} = \left|\frac{\Delta F}{\Delta_s^2}\right| \quad u_{\Delta_s} = 1.190 \cdot 10^5 \text{ N/m} \\ u_{k,\Delta F} &= \left(\frac{\partial k}{\partial \Delta F}\right)_{\Delta F=135 \text{ N}} \quad u_{\Delta F} = \frac{1}{\Delta_s} \quad u_{\Delta F} = 3.750 \cdot 10^6 \text{ N/m} \\ u_k &= \sqrt{u_{k,\Delta_s}^2 + u_{k,\Delta F}^2} = 3.750 \cdot 10^6 \text{ N/m} \end{aligned} \quad (D.4)$$

The uncertainty caused by the probe is insignificant compared to that caused by the manual setting of the load. With the typical order for k at these conditions of 10^8 N/m, the uncertainty would be about 5 % of the measured value, the measured spread in data was significantly larger, approximately 15 %. The modal analysis is on the other hand, is not dependent on the increase of the load, but only on its absolute value.



Results with capacitive sensor for normal test setup

This Appendix presents the results obtained with the capacitive probe. It presents both a load-deflection and a load-stiffness relation.

Figure E.1 shows the distance measured by the capacitive probe as a function of the normal load on a set rollers of type 1 that are tested 10 times.

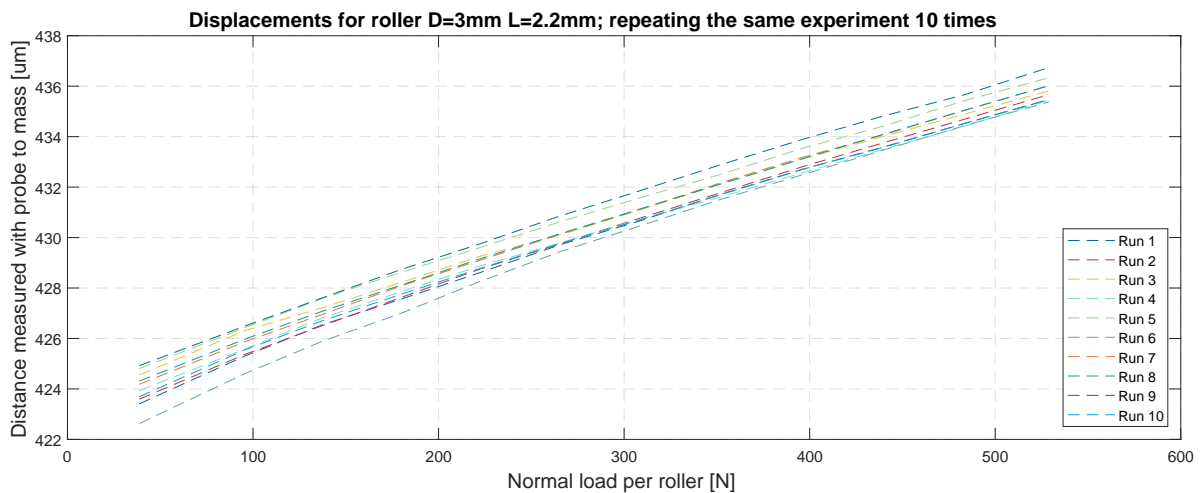


Figure E.1: Capacitive probe data: Load-deflection relation of roller type 1 under normal conditions; 10 runs, estimating repeatability.

The absolute value, and thus the zero shift error, of this measurement is not of any relevance as it represents at what distance from the mass the probe is mounted. The deflection relative to the initial distance, the displacements represent the compression of the roller-rail contacts.

Taking the derivatives of the displacements with respect of the load per roller yields the stiffness per roller, this allows for a comparison of the data obtained with the hammer impact measurements and the capacitive sensor data.

Figure E.2 shows the stiffness per roller as a function of the normal load on a set rollers of type 1 that are tested 10 times. Both the hammer impact data (dynamic) and capacitive probe data (static) are depicted.

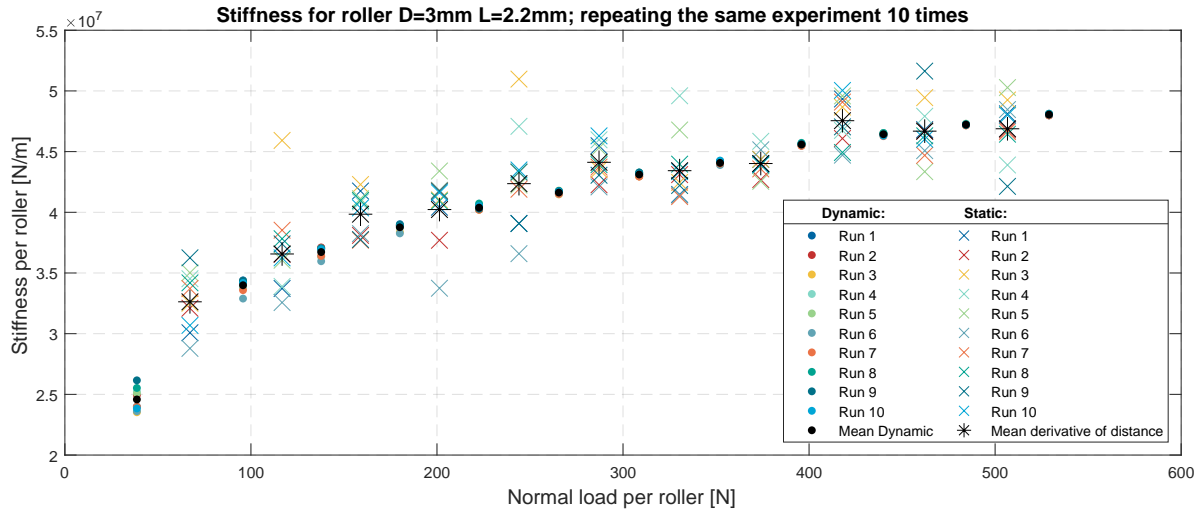


Figure E.2: Hammer impact data (dynamic) and capacitive probe data (static): Load-stiffness relation of roller type 1 under normal conditions; 10 runs, estimating repeatability.

The precision of the stiffness calculated by taking the derivative of the absolute distance is an order of magnitude lower than the hammer impact measurements. However, the mean values of both measurements highly agree. A lower accuracy for stiffness calculated through taking the derivative of a distance is expected as a consequence of the error propagation. See the uncertainty analysis in Appendix D for an estimation of this error.

The high sampling rate of the capacitive measurement allow studying the frequency spectrum of the time data.

Figure E.3 shows the stiffness per roller as a function of the normal load on a set rollers of type 1 that are tested 10 times. Both the accelerometer data (FFT) and capacitive probe data (FFT) are depicted.

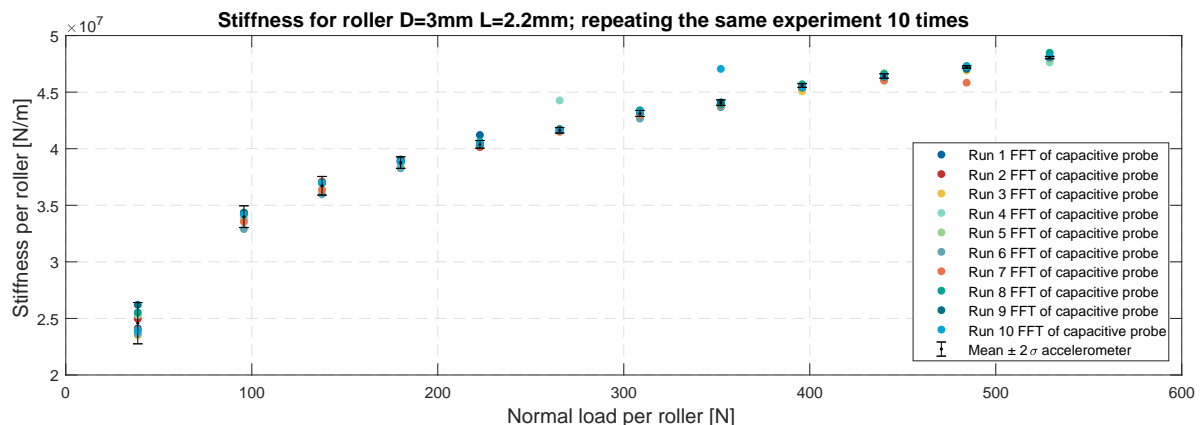
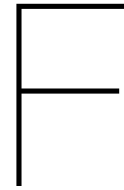


Figure E.3: Hammer impact data (dynamic) and capacitive probe data (dynamic): Load-stiffness relation of roller type 1 under normal conditions; 10 runs, comparing the Stiffness found with the accelerometers with a FFT of the capacitive probe data.

The found peak frequencies match the eigenfrequencies obtained with accelerometers.



Post hoc analysis on normal measurements

This appendix presents the statistical tests performed on the measurements on normally loaded rollers, as presented in Chapter 4. In addition, the descriptive statistics for all normal measurements are given in Section F.2.

F.1. Univariate Analysis of covariance

The goal of the experiments conducted is to compare the different experiment conditions in terms of their stiffness, e.g. answer a question like: *'Is a ceramic roller stiffer than a steel roller?'*

There is random error involved in the measurements, repeating an experiment with the same conditions does not result in the exact same data. Thus, it is important for conclusions to be based on a difference in the underlying true values and not merely a result of coincidence. It is impossible to entirely eliminate the probability that a conclusion is based on coincidence, merely claims on the statistical significance of a result can be made. E.g.: *'Given the measured difference between the dry and lubricated experiments, the probability of obtaining a result with at least this extreme difference between the experiment data, given that a dry and lubricated contact have the same stiffness is x .'* When x is sufficiently low the hypothesis may be rejected.

The stiffness also influenced by the load, a positive covariance between the load and the stiffness is found. Hence there is a need to control for the effects of the load on the stiffness. An (Univariate) Analysis of covariance (ANCOVA) procedure provides regression and analysis of covariance for a dependent variable (stiffness) by a categorical independent variable (experiment conditions) while statistically controlling for the effects of an other continuous predictor (load).

F.1.1. Statistical assumptions

A number of assumptions form the basis of an ANCOVA:

Linearity of regression The ANCOVA model assumes a linear relationship between the dependent variable (*stiffness*) and a covariate (*load*). Based on Section 4.2 it is clear that the relationship between the load and stiffness is not linear. A transformation has to be applied to correct for the problem of non-linearity. Section 4.3 showed that the load-stiffness relation has the form of a natural logarithm. Choosing $\ln(\text{load})$ as the covariate instead of the *load* directly, yields a linear regression relationship between the dependent variable and the covariate. To show the linearity, a simple linear regression is performed on the on the data of repeatability experiments with roller type 1, as plotted in Figure 4.3. With the stiffness as the dependent variable and $\ln(\text{load})$ as the predictor, an Adjusted R Square of 0.994 with $N = 120$.

Homogeneity of error variances I.e. assuming that variance of the residuals (difference between predicted and measured values) is constant across groups (homoscedasticity). Levene's Test of Equality of Error Variances is performed to test the null hypothesis that the error variance of the dependent variable, $\ln(\text{load})$, is equal across groups.

Independence of error terms The errors are uncorrelated. That is, the error covariance matrix is diagonal.

Normality of error terms I.e. having the residuals distributed normally around the predicted value. Performing a normality test, Shapiro Will, or checking the skewdwsity and kurtosis will allow for testing this. For larger sample sizes, normality of error terms is of less importance. The ANCOVA is in certain conditions robust to violations of the normality condition [71].

Homogeneity of regression slopes When there is homogeneity of regression slopes, the linear regression relationships in are all parallel and do not cross. The slopes of the different groups can be compared by means Interaction terms. The p-value for the interaction between the experiment conditions and $\ln(\text{load})$ is tested for significance. If interaction is significant, it is very unlikely that the slopes are parallel and the ANCOVA should not be used.

F.1.2. Results

The data of the three repetitions of the specific configurations are compared to the stiffness data of the ten repetitions of the standard configuration as plotted in Figure 4.3, this could be seen as the control group.

Product variations of rollers

The null hypothesis is that all experiment means are equal when controlling for the load.

The covariate by condition interaction is not statistically significant at all: $F(3, 196) = 0.520$, $p = 0.669$, thus homogeneity of regression slopes may be assumed. The effect size for the condition is small, $\eta^2 = 0.009$.

A Levene's test is included to test the homogeneity of variance assumption. The null hypothesis of equal error variances is not rejected, $F(3, 200) = 1.926$, $p = 0.127$. The data meets the homogeneity of variances assumption. This means that an ANCOVA can be performed confidently.

Table F.1: Analysis of Covariance for stiffness by roller variation at normal conditions with the load as covariate.

Source	Type III Sum of Squares	df	Mean Square	F	Sig.	η^2
Corrected Model	$7.584 \cdot 10^{16a}$	4	$1.896 \cdot 10^{16}$	$8.466 \cdot 10^3$	0.000	0.994
Intercept	$2.681 \cdot 10^{16}$	1	$2.681 \cdot 10^{16}$	$1.197 \cdot 10^4$	0.000	0.984
condition	$3.320 \cdot 10^{13}$	3	$1.107 \cdot 10^{13}$	4.941	0.000	0.274
$\ln(\text{load})$	$7.581 \cdot 10^{16}$	1	$7.581 \cdot 10^{16}$	$3.385 \cdot 10^4$	0.002	0.069
Error	$4.457 \cdot 10^{14}$	199	$2.240 \cdot 10^{12}$			
Total	$3.214 \cdot 10^{18}$	204				
Corrected Total	$7.642 \cdot 10^{16}$	203				

^aR Squared = 0.994 (Adjusted R Squared = 0.994)

The analysis has a significant p-value and thus rejects the null hypothesis that the conditions result in equal stiffness, $F(3, 199) = 4.941$, $p = 0.002$.

An ANOVA was also performed and the mean differences are statistically significant only when the covariate is included, the covariate greatly reduces the standard errors for these means. Pairwise comparison only showed significant difference between set 1 and the other sets, no pairwise significance between the other sets was measured.

Influence of lubrication, grease and oil compared with dry contact

The null hypothesis is that all experiment means are equal when controlling for the load.

The covariate by condition interaction is not statistically significant at all: $F(2, 186) = 0.059$, $p = 0.943$, thus homogeneity of regression slopes assumption seems to hold almost perfectly. The effect size for the condition is small, $\eta^2 = 0.001$.

A Levene's test is performed to test the homogeneity of variance assumption. The null hypothesis of equal error variances is not rejected, $F(2, 189) = 1.096$, $p = 0.336$. The data meets the homogeneity of variances assumption. This means that an ANCOVA can be performed confidently.

Table F.2: Analysis of Covariance for stiffness by lubrication variation at normal conditions with the load as covariate.

Source	Type III Sum of Squares	df	Mean Square	F	Sig.	η^2
Corrected Model	$7.092 \cdot 10^{16a}$	3	$2.364 \cdot 10^{16}$	$1.173 \cdot 10^4$	0.000	0.995
Intercept	$2.551 \cdot 10^{16}$	1	$2.551 \cdot 10^{16}$	$1.265 \cdot 10^4$	0.000	0.985
condition	$4.766 \cdot 10^{12}$	2	$2.383 \cdot 10^{12}$	1.182	0.309	0.012
$\ln(\text{load})$	$7.092 \cdot 10^{16}$	1	$7.092 \cdot 10^{16}$	$3.518 \cdot 10^4$	0.000	0.995
Error	$3.790 \cdot 10^{14}$	188	$2.016 \cdot 10^{12}$			
Total	$2.954 \cdot 10^{18}$	192				
Corrected Total	$7.130 \cdot 10^{16}$	191				

^aR Squared = 0.995 (Adjusted R Squared = 0.995)

The analysis does not reject the null hypothesis that the conditions result in an equal stiffness, $F(2, 188) = 1.182$, $p = 0.309$.

F.2. Descriptives table for all normal measurements

Table F.3: Statistical data on normal measurements, standard deviation and mean of the stiffness per contact length. The load condition where the springs are not compressed is disregarded in this calculations. Mean values of stiffness per contact length for loaded measurements.

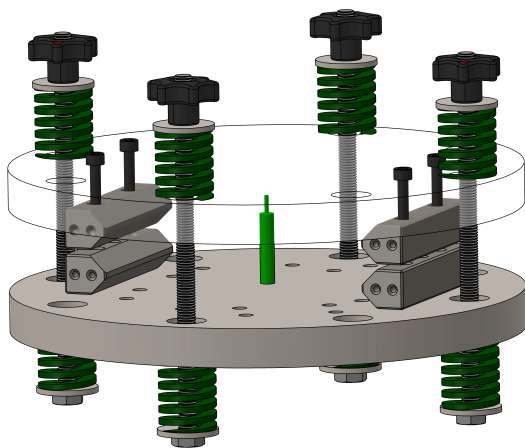
Figure	Legend entry	SD (N/m ²)	μ (N/m ²)	%
4.3	Run X	$10.00 \cdot 10^7$	$2.36 \cdot 10^{10}$	0.42 %
4.5	Mean set 2	$3.31 \cdot 10^8$	$2.40 \cdot 10^{10}$	1.38 %
	Mean set 3	$1.32 \cdot 10^8$	$2.40 \cdot 10^{10}$	0.55 %
	Mean set 4	$8.86 \cdot 10^7$	$2.39 \cdot 10^{10}$	0.37 %
	Mean $\pm 2\sigma$ set 1	See descriptives for Figure 4.3		
4.7	Roller L=2.2mm	See descriptives for Figure 4.3		
	Roller L=2.8mm	$1.89 \cdot 10^8$	$2.18 \cdot 10^{10}$	0.87 %
	Roller L=2mm	$1.38 \cdot 10^8$	$2.31 \cdot 10^{10}$	0.60 %
	Roller L=4mm	$1.74 \cdot 10^8$	$1.98 \cdot 10^{10}$	0.87 %
4.8	Roller D=1.5mm L=1.4mm	$8.49 \cdot 10^7$	$2.31 \cdot 10^{10}$	0.37 %
	Roller D=3mm L=2.2mm	See descriptives for Figure 4.3		
	Roller D=6mm L=4.4mm	$1.91 \cdot 10^8$	$2.25 \cdot 10^{10}$	0.85 %
	Roller D=9mm L=8.8mm	$2.48 \cdot 10^8$	$1.72 \cdot 10^{10}$	1.44 %
4.6	Oil; <i>Klüber Summit SH 32</i>	$2.44 \cdot 10^8$	$2.36 \cdot 10^{10}$	1.04 %
	Grease; <i>Thermoplex ALN 1001/00</i>	$8.48 \cdot 10^7$	$2.35 \cdot 10^{10}$	0.36 %
	Mean $\pm 2\sigma$ dry contact	See descriptives for Figure 4.3		
4.10	Roller D=3mm L=2.8mm Steel	See <i>Roller L=2.8mm</i> in Figure 4.7		
	Roller D=3mm L=2.8mm Si ₃ N ₄	$1.88 \cdot 10^8$	$2.31 \cdot 10^{10}$	0.81 %
4.11	Roller D=3mm L=2.2mm Steel	See descriptives for Figure 4.3		
	Roller D=3mm L=2.2mm Stainless steel	$1.81 \cdot 10^8$	$2.41 \cdot 10^{10}$	0.75 %
4.9	3x Roller D=3mm L=2.2mm	See descriptives for Figure 4.3		
	6x Roller D=3mm L=2.2mm	$1.95 \cdot 10^8$	$2.17 \cdot 10^{10}$	0.90 %
	9x Roller D=3mm L=2.2mm	$8.12 \cdot 10^8$	$2.05 \cdot 10^{10}$	3.95 %
4.13	Standard finish	See descriptives for Figure 4.3		
	Mirror finish	$1.02 \cdot 10^8$	$2.49 \cdot 10^{10}$	0.41 %
4.14	Roller X standard finish	See descriptives for Figure 4.7		
	Roller D=3mm L=2.2mm mirror finish	See <i>Mirror finish</i> in Figure 4.13		
	Roller D=3mm L=2.8mm mirror finish	$6.30 \cdot 10^7$	$2.30 \cdot 10^{10}$	0.27 %
	Roller D=3mm L=2mm mirror finish	$8.39 \cdot 10^7$	$2.41 \cdot 10^{10}$	0.35 %
	Roller D=3mm L=4mm mirror finish	$1.03 \cdot 10^8$	$2.13 \cdot 10^{10}$	0.48 %
4.15	Roller X standard finish	See descriptives for Figure 4.10		
	Roller D=3mm L=2.8mm Si ₃ N ₄ mirror finish	$5.36 \cdot 10^7$	$2.46 \cdot 10^{10}$	0.22 %
	Roller D=3mm L=2.8mm Steel mirror finish	See descriptives for Figure 4.14		
4.16	Roller X standard finish	See descriptives for Figure 4.11		
	Roller D=3mm L=2.2mm Stainless mirror finish	$1.33 \cdot 10^8$	$2.49 \cdot 10^{10}$	0.53 %
	Roller D=3mm L=2.2mm Steel mirror finish	See <i>Mirror finish</i> in Figure 4.13		

G

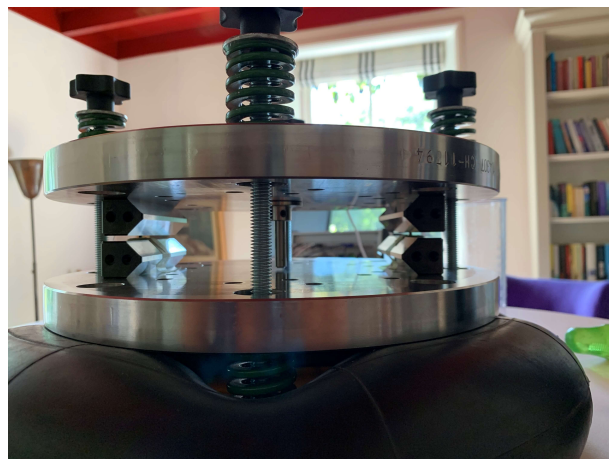
Test setup for measuring individual stiffness components

This Appendix presents a new test setup, this setup is used to perform the experiments such that the individual normal and tangential stiffness components.

The setup, as shown in Figure G.1, is nearly identical to the setup used in Chapter 4, except that here two instead of three rails sets are mounted. These rails are mounted such that the axes of the rollers are co-linear.



(a) CAD model of setup with two rail pairs



(b) Picture of 45° loaded setup

Figure G.1: The test setup used for the experiments in this section. Two pairs of rails are bolted to the two solid disks. The rollers are placed between the rails in the rolling direction. When compressed, the green springs exert load on the rollers and rails. The distance between the masses is measured with a capacitive probe (bright green). The frequency response is measured with accelerometers. The setup is isolated from the external world by a suspension with an inner tube (both not in CAD).

Figure G.2 shows a schematic of the test setup.

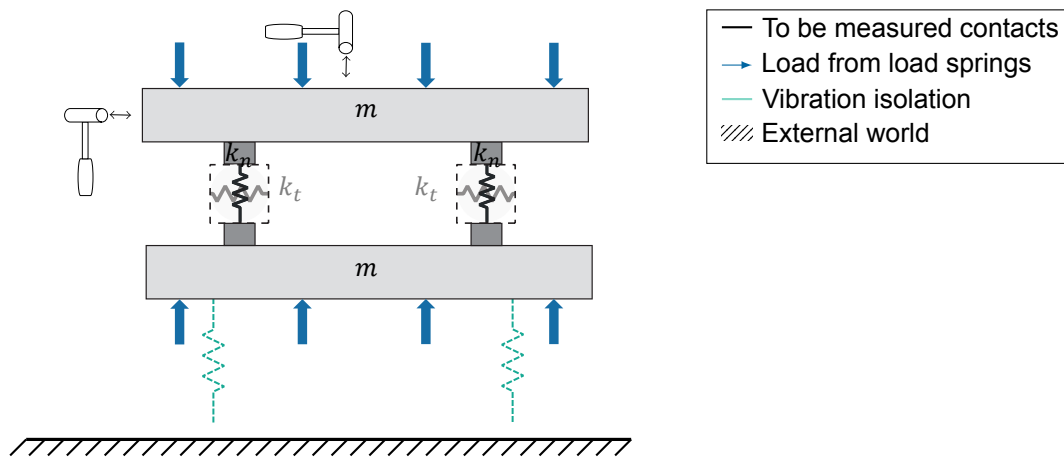


Figure G.2: Schematic depiction of the normally loaded setup.

The setup is modelled as a suspended two mass spring system. The two hammers depicted in Figure G.2 represent the two directions in which eigenmodes are excited. Again a multi body dynamics FEM analysis is performed to determine the stiffness of the setup. The stiffness was found to be $2.73 \cdot 10^8$ N/m, and again properly modelled as being in series with the two rail sets.

G.1. Results

This section presents and discusses the results of the additional experiments performed with this setup.

G.1.1. Influence of roller orientation

Additional normal experiments were performed to assure the effect of roller orientation is not caused by the surface topology and grinding direction. Two rollers of type 1 were oriented perpendicular to the rolling direction.

Figure G.3 depicts this measurement against the results of the repeatability measurements where the roller is oriented parallel.

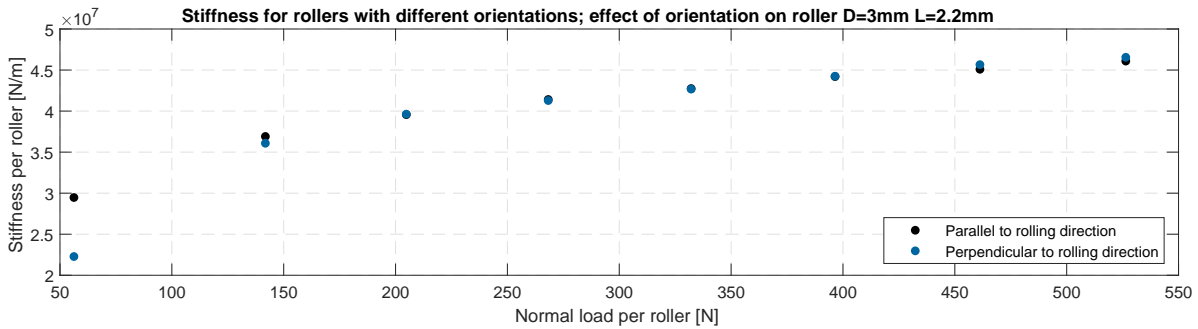


Figure G.3: Hammer impact data: Load-stiffness relation of roller type 1 under normal conditions; roller orientation.

G.1.2. Variation of the number of rails

To find the accuracy of the setup, experiments are compared with the measurements of Chapter 4.

Figure G.4 compares the stiffness measured with the setup from Figure 4.1 with that of Figure G.1.

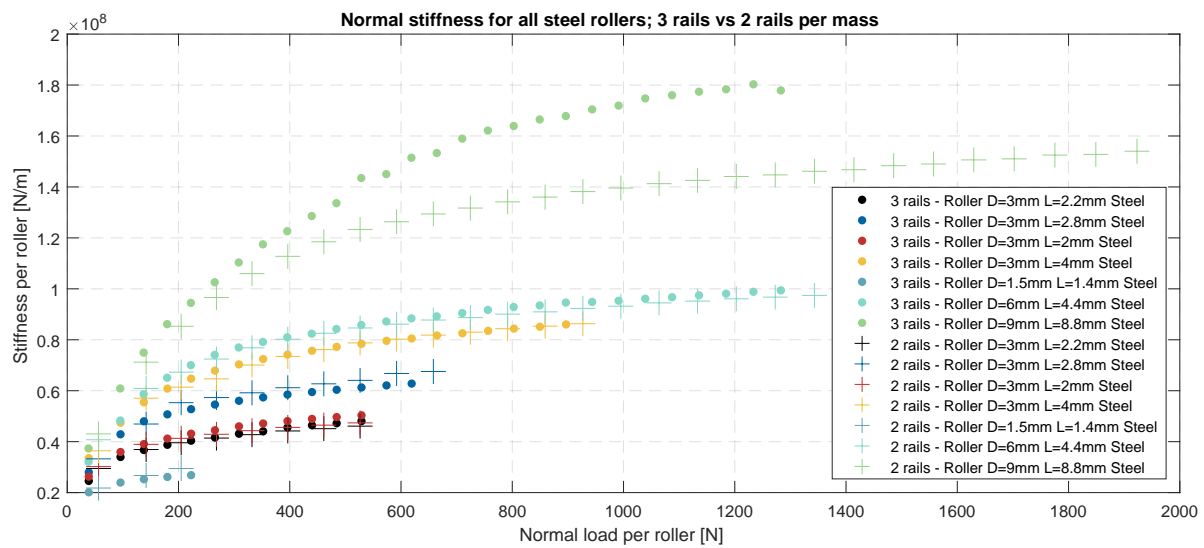


Figure G.4: Hammer impact data: Load-stiffness relation for roller types 1, 2, 3, 4, 5, 6 & 7; 2 rails vs 3 rails.



Post hoc analysis on 45° measurements

This appendix presents the statistical test performed on the measurements on rollers loaded at 45°, as presented in Chapter 5. In addition, the descriptive statistics for all 45° loaded measurements are given in Section H.2.

H.1. Univariate Analysis of covariance

Influence of lubrication

The null hypothesis is that all experiment means are equal when controlling for the load.

The covariate by condition interaction is not statistically significant: $F(2, 90) = 1.478$, $p = 0.234$, thus homogeneity of regression slopes assumption holds. The effect size for the condition is small to medium, $\eta^2 = 0.032$.

A Levene's test is included to test the homogeneity of variance assumption. The null hypothesis of equal error variances is not rejected, $F(2, 93) = 0.513$, $p = 0.600$. The data meets the homogeneity of variances assumption. This means that an ANCOVA can be performed confidently.

Table H.1: Analysis of Covariance for stiffness by lubrication variation at 45° with the load as covariate.

Source	Type III Sum of Squares	df	Mean Square	F	Sig.	η^2
Corrected Model	$1.652 \cdot 10^{20a}$	3	$5.506 \cdot 10^{19}$	$1.614 \cdot 10^3$	0.000	0.981
Intercept	$3.614 \cdot 10^{19}$	1	$3.614 \cdot 10^{19}$	$1.060 \cdot 10^3$	0.000	0.920
condition	$1.728 \cdot 10^{17}$	2	$8.639 \cdot 10^{16}$	2.533	0.085	0.052
$\ln(\text{load})$	$1.650 \cdot 10^{20}$	1	$1.650 \cdot 10^{20}$	$4.838 \cdot 10^3$	0.000	0.981
Error	$3.138 \cdot 10^{18}$	92	$3.410 \cdot 10^{16}$			
Total	$1.593 \cdot 10^{22}$	96				
Corrected Total	$1.683 \cdot 10^{20}$	95				

^aR Squared = 0.981 (Adjusted R Squared = 0.981)

The analysis does not have a significant p-value and thus does not reject the null hypothesis that the conditions result in equal stiffness, $F(3, 92) = 2.533$, $p = 0.085$.

H.2. Descriptives table for all 45° measurements

Table H.2: Statistical data on 45° measurements, standard deviation and mean of the stiffness per contact length. The load condition where the springs are not compressed is disregarded in this calculations. Mean values of stiffness per contact length for loaded measurements. First the standard deviations over the repetitions per load level are calculated, then the mean of the standard deviations is taken. The mean stiffness is the mean value of all measurements per legend entry.

Figure	Legend entry	SD (N/m ²)	μ (N/m ²)	%
5.5	Run X	$1.52 \cdot 10^8$	$1.48 \cdot 10^{10}$	1.03 %
5.6	Mean set 2	$6.04 \cdot 10^7$	$1.51 \cdot 10^{10}$	0.40 %
	Mean set 3	$1.53 \cdot 10^8$	$1.48 \cdot 10^{10}$	1.03 %
	Mean $\pm 2\sigma$ set 1	See descriptives for Figure 5.5		
5.7	Parallel to rolling direction	See descriptives for Figure 5.5		
	Perpendicular to rolling direction	$8.12 \cdot 10^8$	$1.22 \cdot 10^{10}$	6.68 %
5.8	Roller L=2.2mm	See descriptives for Figure 5.5		
	Roller L=2.8mm	$6.85 \cdot 10^7$	$1.50 \cdot 10^{10}$	0.46 %
	Roller L=2mm	$6.17 \cdot 10^7$	$1.48 \cdot 10^{10}$	0.42 %
	Roller L=4mm	$3.04 \cdot 10^8$	$1.48 \cdot 10^{10}$	2.06 %
5.9	Roller D=1.5mm L=1.4mm	$1.80 \cdot 10^8$	$1.66 \cdot 10^{10}$	1.09 %
	Roller D=3mm L=2.2mm	See descriptives for Figure 5.5		
	Roller D=6mm L=4.4mm	$1.38 \cdot 10^8$	$1.41 \cdot 10^{10}$	0.98 %
5.12	Oil; <i>Klüber Summit SH 32</i>	$7.76 \cdot 10^7$	$1.46 \cdot 10^{10}$	0.53 %
	Grease; <i>Thermoplex ALN 1001/00</i>	$1.63 \cdot 10^8$	$1.47 \cdot 10^{10}$	1.11 %
	Mean $\pm 2\sigma$ dry contact	See descriptives for Figure 5.5		
5.14	Roller D=3mm L=2.8mm Steel	See <i>Roller L=2.8mm</i> in Figure 5.8		
	Roller D=3mm L=2.8mm Si ₃ N ₄	$1.05 \cdot 10^8$	$1.68 \cdot 10^{10}$	0.63 %
5.15	Roller D=3mm L=2.2mm Steel	See descriptives for Figure 5.5		
	Roller D=3mm L=2.2mm Stainless steel	$2.09 \cdot 10^8$	$1.52 \cdot 10^{10}$	1.38 %
5.13	2x Roller D=3mm L=2.2mm	See descriptives for Figure 5.5		
	4x Roller D=3mm L=2.2mm	$1.81 \cdot 10^8$	$1.41 \cdot 10^{10}$	1.15 %
	6x Roller D=3mm L=2.2mm	$1.32 \cdot 10^8$	$1.34 \cdot 10^{10}$	0.98 %
5.16	Roller D=1.5mm L=1.4mm	$1.47 \cdot 10^{5a}$	$5.88 \cdot 10^{6a}$	2.50 %
	Roller D=3mm L=2.2mm	$9.95 \cdot 10^{4a}$	$7.05 \cdot 10^{6a}$	1.41 %
	Roller D=3mm L=2.8mm	$3.04 \cdot 10^{5a}$	$1.49 \cdot 10^{7a}$	2.05 %
	Roller D=3mm L=2mm	$1.67 \cdot 10^{5a}$	$8.46 \cdot 10^{6a}$	1.98 %
	Roller D=3mm L=4mm	$1.81 \cdot 10^{6a}$	$2.83 \cdot 10^{7a}$	6.41 %
	Roller D=6mm L=4.4mm	$1.93 \cdot 10^{5a}$	$1.54 \cdot 10^{7a}$	1.25 %
5.18	Roller D=9mm L=8.8mm	$5.51 \cdot 10^{5a}$	$3.84 \cdot 10^{7a}$	1.44 %
	45° Stiffness	See descriptives for Figure 5.5		
	Normal Stiffness* $\cos(45)^\circ$ ²	$1.01 \cdot 10^8$	$1.18 \cdot 10^{10}$	0.86 %
	Tangential Stiffness* $\sin(45)^\circ$ ²	$2.77 \cdot 10^7$	$1.97 \cdot 10^9$	1.41 %
5.20	Normal * $\cos(45)^\circ$ ² + Tangential* $\sin(45)^\circ$ ²	$1.20 \cdot 10^8$	$1.38 \cdot 10^{10}$	0.87 %
	Perpendicular to rolling direction	See <i>Perpendicular</i> in Figure 5.7		
5.19	Normal Stiffness* $\cos(45)^\circ$ ²	See <i>Normal * $\cos(45)^\circ$</i> in Figure 5.18		
	45° Stiffness - Roller D=3mm L=2.2mm	See descriptives for Figure 5.5		
	45° Stiffness - Roller D=3mm L=2.8mm	See <i>Roller D=3mm L=2.8mm</i> in Figure 5.8		
	45° Stiffness - Roller D=3mm L=2mm	See <i>Roller D=3mm L=2mm</i> in Figure 5.8		
	45° Stiffness - Roller D=3mm L=4mm	See <i>Roller D=3mm L=4mm</i> in Figure 5.8		
	45° Stiffness - Roller D=1.5mm L=1.4mm	See <i>Roller D=1.5mm L=1.4mm</i> in Figure 5.9		
	(Normal + Tangential)*0.5 - Roller D=3mm L=2.2mm	$2.15 \cdot 10^{5a}$	$2.47 \cdot 10^{7a}$	0.87 %
	(Normal + Tangential)*0.5 - Roller D=3mm L=2.8mm	$4.33 \cdot 10^{5a}$	$3.72 \cdot 10^{7a}$	1.16 %
	(Normal + Tangential)*0.5 - Roller D=3mm L=2mm	$9.57 \cdot 10^{4a}$	$2.62 \cdot 10^{7a}$	0.37 %
	(Normal + Tangential)*0.5 - Roller D=3mm L=4mm	$1.91 \cdot 10^{6a}$	$5.20 \cdot 10^{7a}$	3.68 %
(Normal + Tangential)*0.5 - Roller D=1.5mm L=1.4mm	$1.25 \cdot 10^{5a}$	$1.70 \cdot 10^{7a}$	0.74 %	

^a Stiffness per roller (N/m)

Test setup for measuring crossed roller slides

This Appendix contains the parameters and dimensions of the masses used for the experiments in Chapter 6.

I.1. Parameters

Table I.1: Parameters for crossed roller slide setup.

Part	Name	Value	Unit	Description
Top mass	m	19.284	kg	Mass
	I_x	$5.846 \cdot 10^{-2}$	kg m ²	Moment of inertia around x -axis
	I_z	$5.890 \cdot 10^{-2}$	kg m ²	Moment of inertia around y -axis
	I_y	$7.143 \cdot 10^{-2}$	kg m ²	Moment of inertia around z -axis
	s_z	59.315	mm	Distance along z -axis between CoM and mounting face
	s_z	0.200	μm	Surface roughness of rail surfaces
Bottom mass	m	19.280	kg	Mass
	I_x	$5.503 \cdot 10^{-2}$	kg m ²	Moment of inertia around x -axis
	I_y	$5.650 \cdot 10^{-2}$	kg m ²	Moment of inertia around y -axis
	I_z	$6.960 \cdot 10^{-2}$	kg m ²	Moment of inertia around z -axis
	s_z	57.105	mm	Distance along z -axis between CoM and mounting face
	s_z	0.200	μm	Surface roughness of rail surfaces

Table I.2: Parameters for crossed roller slide PM Bearings RT-3150 and RT-15100.

Parameter	RT-3150	RT-1510	Unit	Description
m	1.860	0.370	kg	Mass
t_w	5	3	mm	Cage pocket pitch
C_d	30	13.5	mm	Cage distance
H	28	17	mm	Height
Roller	13	14		See element Table A.1

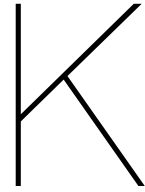


Multi body dynamics analysis of test setup for measuring crossed roller slides

This Appendix presents a table with the results of different numerical models to show the model convergence.

Table J.1: Result of modal analysis, 16 rollers per cage 5 turns load: different meshes and models.

Variable	Unit	Standard mesh	Refined mesh	Refined model
Number of elements	-	130 466	251 266	436 431
Volume	cm ³	5192	5155	5153
Eigenfrequency z mode	Hz	718.99	718.59	713.57
Eigenfrequency θ_x mode	Hz	354.58	353.45	351.14
Eigenfrequency θ_z mode	Hz	333.70	331.93	328.82



Post hoc analysis on crossed roller guide measurements

This appendix presents the error plots of the measurements on crossed roller slides, as presented in Chapter 6. In addition, the descriptive statistics for measurements on tables are given in Section K.1.

Figure K.1 presents the error between the measured and predicted load-stiffness relationship in z -direction for a RT-3150 slide. The stiffness measurements are performed for $Z_t = 4, 6, 8, 10, 12, 14, 16, 20,$ and 26 .

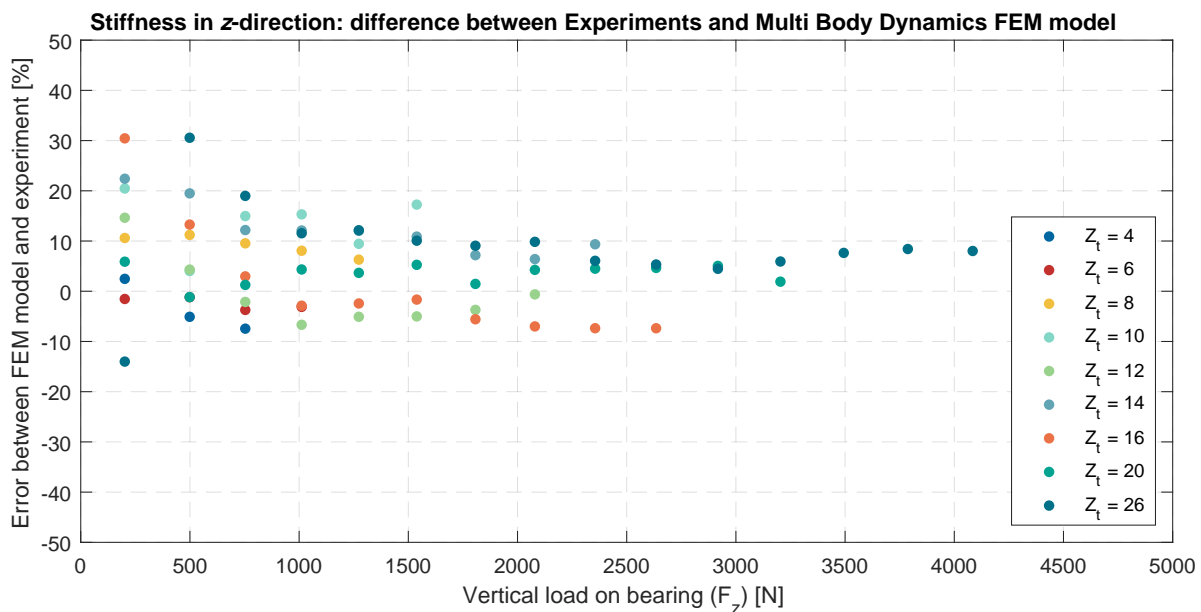


Figure K.1: Hammer impact data: Error between Experiments and FEM model of RT-3150 crossed-roller slide, stiffness in z -direction.

Figure K.2 presents the error between the measured and predicted load-stiffness relationship in θ_x -direction for a RT-3150 slide. The stiffness measurements are performed for $Z_t = 4, 6, 8, 10, 12, 14, 16, 20,$ and 26 .

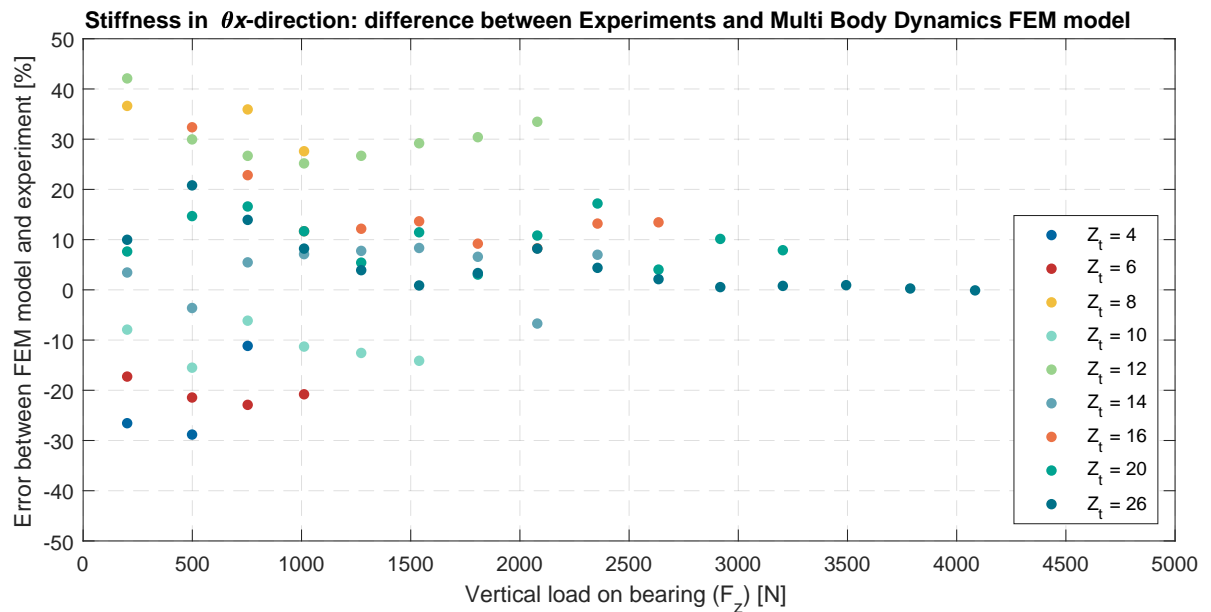


Figure K.2: Hammer impact data: Error between Experiments and FEM model of RT-3150 crossed-roller slide, stiffness in θ_x -direction.

Figure K.3 presents the error between the measured and predicted load-stiffness relationship in θ_z -direction for a RT-3150 slide. The stiffness measurements are performed for $Z_t = 4, 6, 8, 10, 12, 14, 16, 20,$ and 26 .

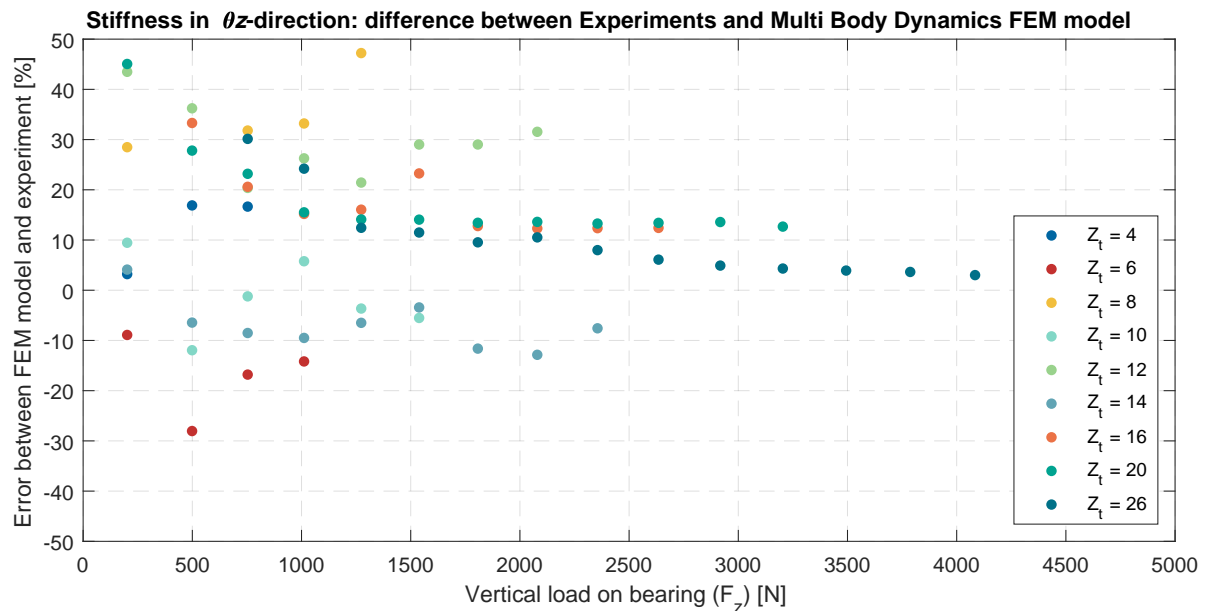


Figure K.3: Hammer impact data: Error between Experiments and FEM model of RT-3150 crossed-roller slide, stiffness in θ_z -direction.

Figure K.2 presents the error between the measured and predicted load-stiffness relationship in z -direction for a RT-15100 slide. The stiffness measurements are performed for $Z_t = 8, 10, 12, 14, 16, 20,$ and 28 .

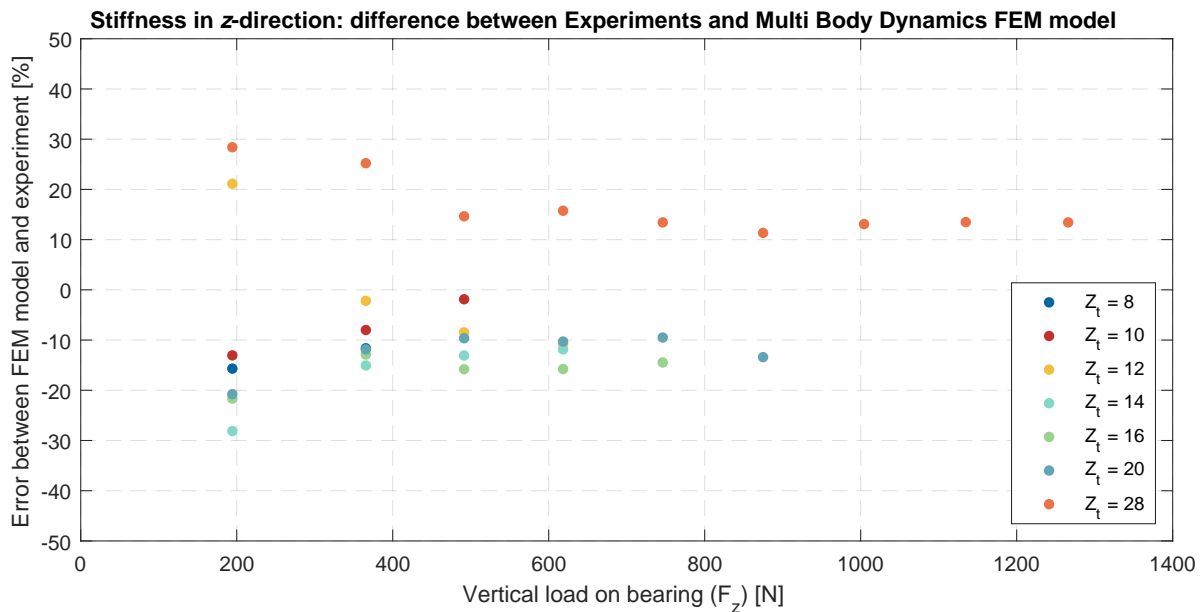


Figure K.4: Hammer impact data: Error between Experiments and FEM model of RT-15100 crossed-roller slide, stiffness in z -direction.

Figure K.5 shows the difference in load-stiffness relationship compared with measurements from Figure 6.8.

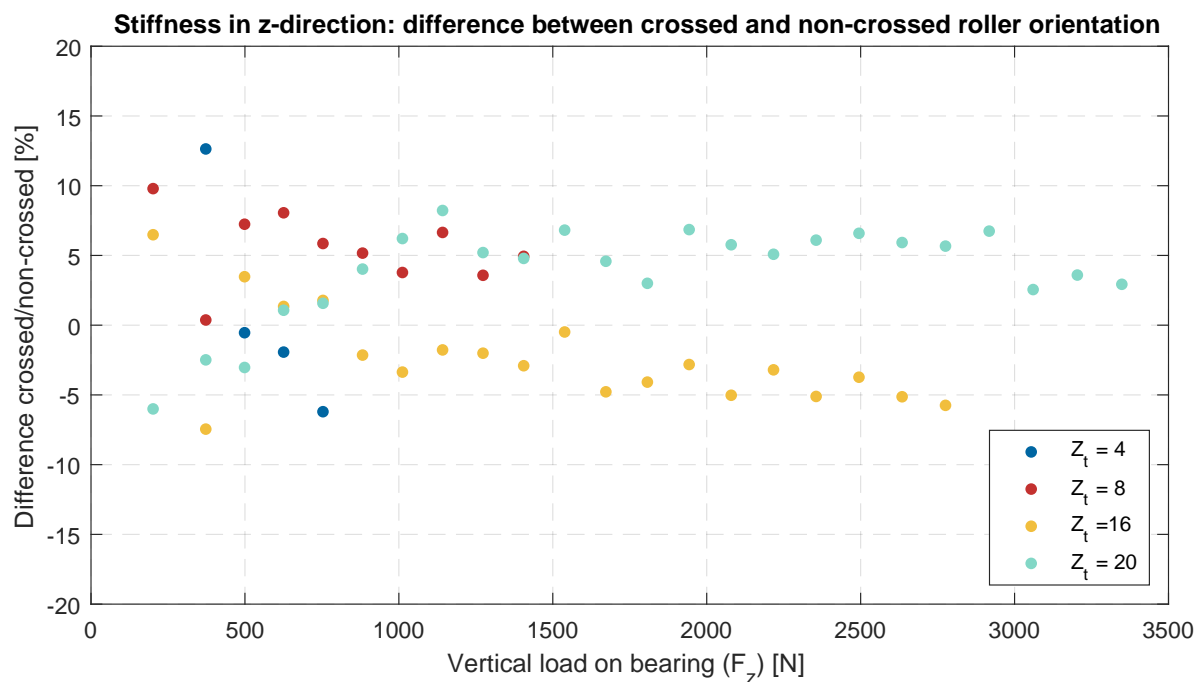


Figure K.5: Hammer impact data: Difference between roller orientation RT-3150 crossed-roller slide, stiffness in θz -direction.

K.1. Descriptives table of all measurements with the crossed roller guides

Table K.1: Statistical data on measurements with crossed roller guides, standard deviation and mean of the stiffness in z direction. The mean stiffness is the mean value of all measurements per legend entry.

Figure	Legend entry	SD (N/m)	μ (N/m)	%
6.8	Experiment: $Z_t = 4$	$1.15 \cdot 10^6$	$5.88 \cdot 10^7$	1.96
	Experiment: $Z_t = 6$	$1.42 \cdot 10^6$	$7.89 \cdot 10^7$	1.80
	Experiment: $Z_t = 8$	$2.42 \cdot 10^6$	$9.50 \cdot 10^7$	2.55
	Experiment: $Z_t = 10$	$6.66 \cdot 10^6$	$1.11 \cdot 10^8$	6.01
	Experiment: $Z_t = 12$	$7.00 \cdot 10^6$	$1.51 \cdot 10^8$	4.63
	Experiment: $Z_t = 14$	$5.70 \cdot 10^6$	$1.52 \cdot 10^8$	3.75
	Experiment: $Z_t = 16$	$5.92 \cdot 10^6$	$2.01 \cdot 10^8$	2.94
	Experiment: $Z_t = 20$	$6.26 \cdot 10^6$	$2.30 \cdot 10^8$	2.72
	Experiment: $Z_t = 26$	$6.57 \cdot 10^6$	$2.81 \cdot 10^8$	2.33
6.10a	Experiment: $Z_t = 4$	$1.26 \cdot 10^{3a}$	$6.80 \cdot 10^{3a}$	18.59
	Experiment: $Z_t = 6$	$1.95 \cdot 10^{2a}$	$5.79 \cdot 10^{3a}$	3.37
	Experiment: $Z_t = 8$	$3.48 \cdot 10^{3a}$	$1.52 \cdot 10^{4a}$	22.96
	Experiment: $Z_t = 10$	$1.26 \cdot 10^{3a}$	$2.43 \cdot 10^{4a}$	5.19
	Experiment: $Z_t = 12$	$1.29 \cdot 10^{3a}$	$4.43 \cdot 10^{4a}$	2.92
	Experiment: $Z_t = 14$	$3.37 \cdot 10^{3a}$	$5.45 \cdot 10^{4a}$	6.18
	Experiment: $Z_t = 16$	$6.09 \cdot 10^{3a}$	$1.05 \cdot 10^{5a}$	5.78
	Experiment: $Z_t = 20$	$1.31 \cdot 10^{4a}$	$1.93 \cdot 10^{5a}$	6.79
	Experiment: $Z_t = 26$	$1.15 \cdot 10^{4a}$	$3.34 \cdot 10^{5a}$	3.45
6.10b	Experiment: $Z_t = 4$	$4.23 \cdot 10^{2a}$	$5.62 \cdot 10^{3a}$	7.52
	Experiment: $Z_t = 6$	$1.02 \cdot 10^{3a}$	$7.63 \cdot 10^{3a}$	13.39
	Experiment: $Z_t = 8$	$2.38 \cdot 10^{3a}$	$2.19 \cdot 10^{4a}$	10.90
	Experiment: $Z_t = 10$	$2.35 \cdot 10^{3a}$	$3.07 \cdot 10^{4a}$	7.65
	Experiment: $Z_t = 12$	$6.16 \cdot 10^{3a}$	$6.13 \cdot 10^{4a}$	10.05
	Experiment: $Z_t = 14$	$6.21 \cdot 10^{3a}$	$8.61 \cdot 10^{4a}$	7.21
	Experiment: $Z_t = 16$	$5.22 \cdot 10^{3a}$	$1.45 \cdot 10^{5a}$	3.59
	Experiment: $Z_t = 20$	$5.86 \cdot 10^{3a}$	$2.61 \cdot 10^{5a}$	2.25
	Experiment: $Z_t = 26$	$1.29 \cdot 10^{4a}$	$4.57 \cdot 10^{5a}$	2.82
6.11	Experiment: $Z_t = 8$	$7.83 \cdot 10^5$	$6.42 \cdot 10^7$	1.22
	Experiment: $Z_t = 10$	$2.60 \cdot 10^6$	$7.27 \cdot 10^7$	3.58
	Experiment: $Z_t = 12$	$1.48 \cdot 10^6$	$8.85 \cdot 10^7$	1.67
	Experiment: $Z_t = 14$	$7.66 \cdot 10^5$	$1.05 \cdot 10^8$	0.73
	Experiment: $Z_t = 16$	$3.17 \cdot 10^6$	$1.23 \cdot 10^8$	2.58
	Experiment: $Z_t = 20$	$1.20 \cdot 10^6$	$1.41 \cdot 10^8$	0.85
	Experiment: $Z_t = 28$	$7.32 \cdot 10^5$	$1.50 \cdot 10^8$	0.49
6.12	Experiment: $Z_t = z/2 = 4$	$1.81 \cdot 10^6$	$5.35 \cdot 10^7$	3.38
	Experiment: $Z_t = z/2 = 8$	$3.56 \cdot 10^6$	$9.82 \cdot 10^7$	3.62
	Experiment: $Z_t = z/2 = 16$	$5.92 \cdot 10^6$	$2.01 \cdot 10^8$	2.94
	Experiment: $Z_t = z/2 = 20$	$6.26 \cdot 10^6$	$2.30 \cdot 10^8$	2.72
	Experiment: $Z_t = Z = 4$	$1.88 \cdot 10^6$	$5.90 \cdot 10^7$	3.18
	Experiment: $Z_t = Z = 8$	$1.22 \cdot 10^6$	$9.98 \cdot 10^7$	1.22
	Experiment: $Z_t = Z = 16$	$1.33 \cdot 10^6$	$1.95 \cdot 10^8$	0.68
	Experiment: $Z_t = Z = 20$	$1.51 \cdot 10^6$	$2.41 \cdot 10^8$	0.63

^a Radial stiffness(N m/rad)

Bibliography

- [1] R. M. Schmidt, G. Schitter, and J. van Eijk. *The design of high performance mechatronics*. IOS Press, 2011. ISBN 9781607508250. doi: 10.3233/978-1-61499-368-1-i. URL <https://doi.org/10.3233/978-1-61499-368-1-i>.
- [2] R. P. T. Eling. *Towards robust design optimization of automotive turbocharger rotor-bearing systems*. PhD thesis, Delft University of Technology, 2018. URL <https://doi.org/10.4233/uuid:fdb0da19-0ef2-4bb6-92a7-8a7acbb05dd2>.
- [3] A. van Beek. *Advanced engineering design : lifetime performance and reliability*. TU Delft, Delft, sixth edit edition, 2015. ISBN 9789081040617. URL <http://www.worldcat.org/oclc/928725664>.
- [4] C. Rossi and F. Russo. *Ancient Engineers' Inventions*, volume 33 of *History of Mechanism and Machine Science*. Springer International Publishing, Cham, 2017. ISBN 978-3-319-44475-8. doi: 10.1007/978-3-319-44476-5. URL <https://doi.org/10.1007/978-3-319-44476-5>.
- [5] L. Reti. Leonardo on Bearings and Gears. *Scientific American*, 224(2):100–110, 2 1971. ISSN 0036-8733. doi: 10.1038/scientificamerican0271-100. URL <https://doi.org/10.1038/scientificamerican0271-100>.
- [6] J. Harrison. H3, 1757. URL <https://collections.rmg.co.uk/collections/objects/79141.html>.
- [7] P. Vaughan. Iron ball bearings for carriage wheel-axles, 1794.
- [8] T. A. Harris and W. J. Anderson. Rolling Bearing Analysis. *Journal of Lubrication Technology*, 89(4):521–521, 10 2006. ISSN 0022-2305. doi: 10.1115/1.3617048. URL <https://doi.org/10.1115/1.3617048>.
- [9] S. Wingqvist. A multi-row self-aligning radial ball bearing, 1907. URL https://tc.prv.se/spd/pdf/WKDSs1L65A_SfAo8BkBrHw/SE25406.C1.pdf.
- [10] K. Zwick. Slide guide for machine tools, 1941. URL <https://patents.google.com/patent/US2242498A>.
- [11] Schneeberger. History - Schneeberger Group, 2020. URL <https://www.schneeberger.com/en/about-us/history/>.
- [12] S. W. Hong and V. C. Tong. Rolling-element bearing modeling: A review. *International Journal of Precision Engineering and Manufacturing*, 17(12):1729–1749, 2016. ISSN 20054602. doi: 10.1007/s12541-016-0200-z. URL <https://doi.org/10.1007/s12541-016-0200-z>.
- [13] K. L. Johnson. *Contact Mechanics*. Cambridge University Press, 1985. ISBN 9780521347969. doi: 10.1201/b17110-2. URL <https://doi.org/10.1017/CBO9781139171731>.
- [14] H. Hertz. Ueber die Berührung fester elastischer Körper. *Journal für die Reine und Angewandte Mathematik*, 1882(92):156–171, 1882. ISSN 14355345. doi: 10.1515/crll.1882.92.156. URL <https://doi.org/10.1515/crll.1882.92.156>.
- [15] H. Hertz. *Miscellaneous Papers*. Macmillan, London, translated edition, 1896. URL <http://www.worldcat.org/oclc/741127489>.
- [16] J. Tripp. Hertzian Contact in Two and Three Dimensions. Technical report, NASA, 1985. URL <https://ntrs.nasa.gov/citations/19850024018>.

- [17] F. G. Nakhatakyan. Precise solution of Hertz contact problem for circular cylinders with parallel axes. *Russian Engineering Research*, 31(3):193–196, 3 2011. ISSN 1068-798X. doi: 10.3103/S1068798X11030208. URL <https://doi.org/10.3103/S1068798X11030208>.
- [18] L. Tudose and C. Tudose. Roller profiling to increase rolling bearing performances. *IOP Conference Series: Materials Science and Engineering*, 393(1):012002, 8 2018. ISSN 1757-899X. doi: 10.1088/1757-899X/393/1/012002. URL <https://doi.org/10.1088/1757-899X/393/1/012002>.
- [19] G. Lundberg. Elastische Berührung zweier Halbräume. *Forschung auf dem Gebiete des Ingenieurwesens*, 10(5):201–211, 9 1939. ISSN 0015-7899. doi: 10.1007/BF02584950. URL <https://doi.org/10.1007/BF02584950>.
- [20] K. Kunert. Spannungsverteilung im Halbraum bei elliptischer Flächenpressungsverteilung über einer rechteckigen Druckfläche. *Forschung auf dem Gebiete des Ingenieurwesens*, 27(6):165–174, 11 1961. ISSN 0015-7899. doi: 10.1007/BF02561354. URL <https://doi.org/10.1007/BF02561354>.
- [21] R. Teutsch and B. Sauer. An Alternative Slicing Technique to Consider Pressure Concentrations in Non-Hertzian Line Contacts. *Journal of Tribology*, 126(3):436–442, 7 2004. ISSN 0742-4787. doi: 10.1115/1.1739244. URL <https://doi.org/10.1115/1.1739244>.
- [22] H. A. Rothbart. *Mechanical design and systems handbook*. McGraw-Hill, New York SE - .. cm., 2nd ed. edition, 1985. ISBN 9780070540200. URL <https://tudelft.on.worldcat.org/v2/oclc/839660793>.
- [23] C. H. Venner and W. E. ten Napel. Surface Roughness Effects in an EHL Line Contact. *Journal of Tribology*, 114(3):616–622, 7 1992. ISSN 0742-4787. doi: 10.1115/1.2920926. URL <https://doi.org/10.1115/1.2920926>.
- [24] J. J. Kalker, F. M. Dekking, and E. A. Vollebregt. Simulation of rough, elastic contacts. *Journal of Applied Mechanics, Transactions ASME*, 64(2):361–368, 1997. ISSN 15289036. doi: 10.1115/1.2787315. URL <https://doi.org/10.1115/1.2787315>.
- [25] J. W. Kannel and M. J. Hartnett. Theoretical and Experimental Evaluation of Edge Stresses Under Severe Edge Loads. *A S L E Transactions*, 26(1):25–30, 1 1983. doi: 10.1080/05698198308981473. URL <https://doi.org/10.1080/05698198308981473>.
- [26] J. J. Kalker. On Elastic Line Contact. *Journal of Applied Mechanics*, 39(4):1125–1132, 12 1972. ISSN 0021-8936. doi: 10.1115/1.3422841. URL <https://doi.org/10.1115/1.3422841>.
- [27] J. J. KALKER. *On the rolling contact of two elastic bodies in the presence of dry friction*. PhD thesis, Delft University of technology, 1967. URL <http://resolver.tudelft.nl/uuid:aa44829b-c75c-4abd-9a03-fec17e121132>.
- [28] E. Vollebregt. CONTACT, 2020. URL cmcc.nl.
- [29] J. J. Kalker. *Three-Dimensional Elastic Bodies in Rolling Contact*, volume 2 of *Solid Mechanics and Its Applications*. Springer Netherlands, Dordrecht, 1990. ISBN 978-90-481-4066-4. doi: 10.1007/978-94-015-7889-9. URL <https://doi.org/10.1007/978-94-015-7889-9>.
- [30] K. Nikpur and R. Gohar. Deflexion of a roller compressed between platens. *Tribology International*, 8(1):2–8, 1975. ISSN 0301679X. doi: 10.1016/0301-679X(75)90037-7. URL [https://doi.org/10.1016/0301-679X\(75\)90037-7](https://doi.org/10.1016/0301-679X(75)90037-7).
- [31] M. R. Hoepflich and H. Zantopulos. Line contact deformation: A cylinder between two flat plates. *Journal of Tribology*, 103(1):21–25, 1 1981. ISSN 15288897. doi: 10.1115/1.3251609. URL <https://doi.org/10.1115/1.3251609>.
- [32] A. Sherif. Determination of Ball and Roller Compliances Using a Vibration Measuring Technique. *Journal of Tribology*, 117(3):553–557, 7 1995. ISSN 0742-4787. doi: 10.1115/1.2831290. URL <https://doi.org/10.1115/1.2831290>.

- [33] A. Palmgren. *Ball and roller bearing engineering*. SKF industries, Philadelphia, 1959. URL <http://www.worldcat.org/oclc/19827891>.
- [34] A. Palmgren. The Dictionary of Swedish National Biography: N Arvid Palmgren, 2021. URL <http://sok.riksarkivet.se/sbl/Presentation.aspx?id=7995>.
- [35] F. G. Nakhatakyan. Mechanics of contact approach of elastic bodies in Hertz problem. *Journal of Machinery Manufacture and Reliability*, 39(5):444–451, 2010. ISSN 10526188. doi: 10.3103/S1052618810050079. URL <https://doi.org/10.3103/S1052618810050079>.
- [36] J. A. Greenwood and J. H. Tripp. The elastic contact of rough spheres. *Journal of Applied Mechanics, Transactions ASME*, 34(1):153–159, 1964. ISSN 15289036. doi: 10.1115/1.3607616. URL <https://doi.org/10.1115/1.3607616>.
- [37] J. A. Greenwood and J. B. P. Williamson. Contact of nominally flat surfaces. *Proceedings of the Royal Society of London. Series A. Mathematical and Physical Sciences*, 295(1442):300–319, 1966. ISSN 0080-4630. doi: 10.1098/rspa.1966.0242. URL <https://doi.org/10.1098/rspa.1966.0242>.
- [38] J. Kagami, K. Yamada, and T. Hatazawa. Contact between a sphere and rough plates. *Wear*, 87(1):93–105, 1983. ISSN 00431648. doi: 10.1016/0043-1648(83)90025-X. URL [https://doi.org/10.1016/0043-1648\(83\)90025-X](https://doi.org/10.1016/0043-1648(83)90025-X).
- [39] H. McCallion and N. Truong. The deformation of rough cylinders compressed between smooth flat surfaces of hard blocks. *Wear*, 79(3):347–361, 7 1982. ISSN 00431648. doi: 10.1016/0043-1648(82)90324-6. URL [https://doi.org/10.1016/0043-1648\(82\)90324-6](https://doi.org/10.1016/0043-1648(82)90324-6).
- [40] G. G. Gray and K. L. Johnson. The dynamic response of elastic bodies in rolling contact to random roughness of their surfaces. *Journal of Sound and Vibration*, 22(3):323–342, 1972. ISSN 10958568. doi: 10.1016/0022-460X(72)90169-1. URL [https://doi.org/10.1016/0022-460X\(72\)90169-1](https://doi.org/10.1016/0022-460X(72)90169-1).
- [41] A. Kapoor, F. J. Franklin, S. K. Wong, and M. Ishida. Surface roughness and plastic flow in rail wheel contact. *Wear*, 253(1-2):257–264, 2002. ISSN 00431648. doi: 10.1016/S0043-1648(02)00111-4. URL [https://doi.org/10.1016/S0043-1648\(02\)00111-4](https://doi.org/10.1016/S0043-1648(02)00111-4).
- [42] H. Spikes. Basics of EHL for practical application. *Lubrication Science*, 27(1):45–67, 2015. ISSN 15576833. doi: 10.1002/lis.1271. URL <https://doi.org/10.1002/lis.1271>.
- [43] M. Marian, M. Bartz, S. Wartzack, and A. Rosenkranz. Non-Dimensional Groups, Film Thickness Equations and Correction Factors for Elastohydrodynamic Lubrication: A Review. *Lubricants*, 8(10):95, 10 2020. ISSN 2075-4442. doi: 10.3390/lubricants8100095. URL <https://doi.org/10.3390/lubricants8100095>.
- [44] D. Dowson and S. Toyoda. A Central Film Thickness Formula for Elastohydrodynamic Line Contacts, Elastohydrodynamics and Related Topics. In *Proc. 5th Leeds-Lyon Symp., 1978*, volume 60. Elsevier, 1978.
- [45] N. A. H. Tsuha and K. L. Cavalca. Finite line contact stiffness under elastohydrodynamic lubrication considering linear and nonlinear force models. *Tribology International*, 146(December 2019):106219, 6 2020. ISSN 0301679X. doi: 10.1016/j.triboint.2020.106219. URL <https://doi.org/10.1016/j.triboint.2020.106219>.
- [46] P. Soleimanian, M. Mohammadpour, and H. Ahmadian. Coupled tribo-dynamic modelling of linear guideways for high precision machining application. *Proceedings of the Institution of Mechanical Engineers, Part J: Journal of Engineering Tribology*, 235(4):711–737, 4 2021. ISSN 1350-6501. doi: 10.1177/1350650120919885. URL <https://doi.org/10.1177/1350650120919885>.
- [47] H. Nguyen-Schäfer. *Computational design of rolling bearings*. Springer International Publishing, 2016. ISBN 978-3-319-27130-9. doi: 10.1007/978-3-319-27131-6. URL <https://doi.org/10.1007/978-3-319-27131-6>.

- [48] J. P. Hung. Load effect on the vibration characteristics of a stage with rolling guides. *Journal of Mechanical Science and Technology*, 23(1):89–99, 1 2009. ISSN 1738-494X. doi: 10.1007/s12206-008-0925-4. URL <https://doi.org/10.1007/s12206-008-0925-4>.
- [49] H. Ohta and E. Hayashi. Vibration of linear guideway type recirculating linear ball bearings. *Journal of Sound and Vibration*, 235(5):847–861, 2000. ISSN 0022460X. doi: 10.1006/jsvi.2000.2950. URL <https://doi.org/10.1006/jsvi.2000.2950>.
- [50] H. Ohta and K. Tanaka. Vertical stiffnesses of preloaded linear guideway type ball bearings incorporating the flexibility of the carriage and rail. *Journal of Tribology*, 132(1):1–9, 2010. ISSN 07424787. doi: 10.1115/1.4000277. URL <https://doi.org/10.1115/1.4000277>.
- [51] P. Majda. Modeling of geometric errors of linear guideway and their influence on joint kinematic error in machine tools. *Precision Engineering*, 36(3):369–378, 7 2012. ISSN 01416359. doi: 10.1016/j.precisioneng.2012.02.001. URL <https://doi.org/10.1016/j.precisioneng.2012.02.001>.
- [52] J. S. S. Wu, J. C. Chang, and J. P. Hung. The effect of contact interface on dynamic characteristics of composite structures. *Mathematics and Computers in Simulation*, 74(6):454–467, 2007. ISSN 03784754. doi: 10.1016/j.matcom.2006.07.003. URL <https://doi.org/10.1016/j.matcom.2006.07.003>.
- [53] L. Li and J. R. Zhang. Parameters Identification and Dynamic Analysis of Linear Rolling Guide. *Advanced Materials Research*, 199-200:7–12, 2 2011. ISSN 1662-8985. doi: 10.4028/www.scientific.net/AMR.199-200.7.
- [54] W. Tao, Y. Zhong, H. Feng, and Y. Wang. Model for wear prediction of roller linear guides. *Wear*, 305(1-2):260–266, 7 2013. ISSN 00431648. doi: 10.1016/j.wear.2013.01.047. URL <http://doi.org/10.1016/j.wear.2013.01.047>.
- [55] S.-W. Kwon, V.-C. Tong, and S.-W. Hong. Five-degrees-of-freedom model for static analysis of linear roller bearing subjected to external loading. *Proceedings of the Institution of Mechanical Engineers, Part C: Journal of Mechanical Engineering Science*, 233(8):2920–2938, 4 2019. ISSN 0954-4062. doi: 10.1177/0954406218792573. URL <https://doi.org/10.1177/0954406218792573>.
- [56] Schaeffler Technologies AG. BEARINX®, 2020. URL <https://www.schaeffler.com/content.schaeffler.ae/en/products-and-solutions/industrial/calculation-and-advice/calculation/index.jsp>.
- [57] S. Jiang, Y. Wang, and Y. Wang. Modeling of Static Stiffness for Linear Motion Roller Guide. *Journal of Tribology*, 141(11):1–11, 11 2019. ISSN 0742-4787. doi: 10.1115/1.4044292. URL <https://doi.org/10.1115/1.4044292>.
- [58] Y. Liu, L. Song, and N. Liu. Modeling and parameters identification of the cross roller guide way. *2012 IEEE International Conference on Mechatronics and Automation, ICMA 2012*, 1(May):692–696, 8 2012. doi: 10.1109/ICMA.2012.6283226. URL <https://doi.org/10.1109/ICMA.2012.6283226>.
- [59] K. L. Johnson. Surface interaction between elastically loaded bodies under tangential forces. *Proceedings of the Royal Society of London. Series A. Mathematical and Physical Sciences*, 230 (1183):531–548, 1955. ISSN 0080-4630. doi: 10.1098/rspa.1955.0149. URL <https://doi.org/10.1098/rspa.1955.0149>.
- [60] W. Zeng and D. Resnik. Research integrity in China: Problems and prospects. *Developing World Bioethics*, 10(3):164–171, 2010. ISSN 14718731. doi: 10.1111/j.1471-8847.2009.00263.x. URL <https://doi.org/10.1111/j.1471-8847.2009.00263.x>.
- [61] J. R. Barber. *Contact Mechanics*, volume 250 of *Solid Mechanics and Its Applications*. Springer International Publishing, 2018. ISBN 0521347963. doi: 10.1201/b17588-12. URL <https://doi.org/10.1007/978-3-319-70939-0>.

- [62] H. Nguyen-Schäfer. *Computational Tapered and Cylinder Roller Bearings*. Springer International Publishing, Cham, 2019. ISBN 978-3-030-05443-4. doi: 10.1007/978-3-030-05444-1. URL doi.org/10.1007/978-3-030-05444-1.
- [63] S. Timoshenko and J. N. Goodier. *Theory of Elasticity*. McGraw-Hill Book Company, New York, 1951. ISBN 9780070701229. URL <http://www.worldcat.org/oclc/529127>.
- [64] A. Flamant. Sur la répartition des pressions dans un solide rectangulaire chargé transversalement. *CR Acad. Sci. Paris*, 114:1465–1468, 1892.
- [65] S. Mikhlin. SINGULAR INTEGRAL EQUATIONS. In A. H. Armstrong, editor, *Integral Equations*, pages 113–134. Elsevier, 1957. ISBN 978-1-4832-1284-5. doi: 10.1016/B978-1-4832-1284-5.50009-7. URL <https://doi.org/10.1016/B978-1-4832-1284-5.50009-7>.
- [66] H. FUJIWARA, T. KOBAYASHI, T. KAWASE, and K. YAMAUCHI. Optimized Logarithmic Roller Crowning Design of Cylindrical Roller Bearings and Its Experimental Demonstration. *Tribology Transactions*, 53(6):909–916, 10 2010. ISSN 1040-2004. doi: 10.1080/10402004.2010.510619. URL <https://doi.org/10.1080/10402004.2010.510619>.
- [67] -. Technical Information THERMOPLEX ALN 1001 eng, 2008. URL <https://www.ontrium.com/get.aspx?id=696826>.
- [68] -. Technical Information Klüber Summit SH 32, 46, 68, 100, 2014. URL <https://domxoloda.ru/oils/docs/Summit-SH.pdf>.
- [69] J. A. Greenwood, K. L. Johnson, and E. Matsubara. A surface roughness parameter in Hertz contact. *Wear*, 100(1-3):47–57, 1984. ISSN 00431648. doi: 10.1016/0043-1648(84)90005-X. URL [https://doi.org/10.1016/0043-1648\(84\)90005-X](https://doi.org/10.1016/0043-1648(84)90005-X).
- [70] J. Dekker. Onderzoek naar het gedrag van de stijfheid ten opzichte van de voorspanning op een lineair lager. Technical report, Saxion University of Applied Sciences, 2018.
- [71] S. F. Olejnik and J. Algina. Parametric ANCOVA and the Rank Transform ANCOVA When the Data are Conditionally Non-Normal and Heteroscedastic. *Journal of Educational Statistics*, 9(2): 129–149, 6 1984. ISSN 0362-9791. doi: 10.3102/10769986009002129. URL <https://doi.org/10.3102/10769986009002129>.